



**HAL**  
open science

# Investigating morpho-functional plasticity of CA3 axons in living brain slices by a combination of STED microscopy and electrophysiology

Ronan Chereau

► **To cite this version:**

Ronan Chereau. Investigating morpho-functional plasticity of CA3 axons in living brain slices by a combination of STED microscopy and electrophysiology. *Neurons and Cognition [q-bio.NC]*. Université de Bordeaux, 2014. English. NNT : 2014BORD0050 . tel-01191491

**HAL Id: tel-01191491**

**<https://theses.hal.science/tel-01191491>**

Submitted on 2 Sep 2015

**HAL** is a multi-disciplinary open access archive for the deposit and dissemination of scientific research documents, whether they are published or not. The documents may come from teaching and research institutions in France or abroad, or from public or private research centers.

L'archive ouverte pluridisciplinaire **HAL**, est destinée au dépôt et à la diffusion de documents scientifiques de niveau recherche, publiés ou non, émanant des établissements d'enseignement et de recherche français ou étrangers, des laboratoires publics ou privés.

THESIS PRESENTED  
FOR THE DEGREE OF  
**DOCTOR FROM**  
**THE UNIVERSITY OF BORDEAUX**

DOCTORAL SCHOOL OF LIFE SCIENCES AND HEALTH  
SPECIALISATION: NEUROSCIENCE

By Ronan CHEREAU

**Investigating morpho-functional plasticity of  
CA3 axons in living brain slices by a  
combination of STED microscopy and  
electrophysiology**

Supervised by Prof. Valentin NÄGERL

Defended on June 19<sup>th</sup>, 2014

Committee members :

M. Oliet Stéphane, Directeur de Recherche  
M. Dominique Debanne, Directeur de Recherche  
M. Juan Burrone, Professor  
M. Peter Kind, Professor  
M. Andreas Frick, Chargé de Recherche  
M. Valentin Nägerl, Professor

Chair  
Reviewer  
Reviewer  
Examiner  
Examiner  
PhD supervisor

THÈSE PRÉSENTÉE  
POUR OBTENIR LE GRADE DE  
**DOCTEUR DE**  
**L'UNIVERSITÉ DE BORDEAUX**

ÉCOLE DOCTORALE SCIENCES DE LA VIE ET DE LA SANTE  
SPÉCIALITÉ: NEUROSCIENCES

Par Ronan CHEREAU

**Etude de la plasticité morpho-fonctionnelle des  
axones du CA3 sur tranches de cerveau  
vivantes par la microscopie STED et  
l'électrophysiologie**

Sous la direction du Pr. Valentin NÄGERL

Soutenue le 19 Juin 2014

Membres du jury :

M. Oliet Stéphane, Directeur de Recherche  
M. Dominique Debanne, Directeur de Recherche  
M. Juan Burrone, Professeur  
M. Peter Kind, Professeur  
M. Andreas Frick, Chargé de Recherche  
M. Valentin Nägerl, Professeur

Président  
Rapporteur  
Rapporteur  
Examineur  
Examineur  
Directeur de Thèse

## SUMMARY

### **Investigating morpho-functional plasticity of CA3 axons in living brain slices by a combination of STED microscopy and electrophysiology.**

#### **Abstract:**

Millisecond timing precision in the transfer of information between neurons is essential for the synchrony and plasticity of neural circuits in the brain. Axons are neuronal extensions that ensure the communication via brief electrical impulses called action potentials (AP). Because they are unmyelinated and are extremely thin, hippocampal axons propagate APs slowly and thus generate long delays of conduction (up to 100 ms) that are traditionally considered invariant. However, recent studies have shown that activity changes the morphology of axons and modulate the latency of transmission, thus raising the question whether axons undergo activity-dependent structural changes that could influence the propagation of APs.

The diameter of hippocampal axons (ranging between 100-350 nm) are usually too thin to be properly resolved by conventional light microscopy. However, the development of super resolution STED imaging now enables the observation of their detailed morphological dynamics in living tissue.

Using a novel combination of STED microscopy, field recordings, patch-clamp electrophysiology in mouse brain slices and computer simulations we discovered that CA3 axons undergo long-lasting enlargement in their diameter after the induction of long term potentiation (LTP). We provide strong evidence that this diameter enlargement increases AP conduction velocity.

Taken together, our findings indicate that axons can dynamically tune AP propagation delays by changing their diameters, thereby altering the timing of information transfer in neural circuits. This study suggests a novel and powerful structural mechanism for neural plasticity.

**Keywords:** axon, plasticity, nanoscale, STED

---

#### **Research unit**

Interdisciplinary Institute for Neuroscience - CNRS UMR5297

146 rue Léo Saignat

33077 Bordeaux Cedex

## RÉSUMÉ

### **Etude de la plasticité morpho-fonctionnelle des axones du CA3 sur tranches de cerveau vivantes par la microscopie STED et l'électrophysiologie.**

#### **Résumé:**

Une précision à l'échelle de la milliseconde dans le transfert d'informations entre les neurones est essentielle pour la synchronisation et la plasticité des circuits neuronaux dans le cerveau. Les axones sont des prolongements neuronaux qui assurent la communication via des impulsions électriques ou des potentiels d'action (PA). A cause du manque de myéline et de leur diamètre très fin, les axones de l'hippocampe propagent les PA lentement et ainsi générer des délais de conduction très long (jusqu'à 100 ms) qui sont traditionnellement considérés comme invariants. Cependant, plusieurs études ont montré que l'activité change la morphologie des axones et module le temps de latence de la transmission. Il convient donc de se demander si le diamètre des axones varie en fonction de l'activité pouvant influencer la propagation des PA.

Les diamètres des axones non-myélinisés de l'hippocampe (compris entre 100-350 nm) sont généralement trop petits pour être résolu par la microscopie photonique conventionnelle. Le développement récent de l'imagerie super résolution STED permet désormais l'observation de la dynamique de leur morphologie détaillée dans le tissu vivant.

En combinant la microscopie STED, l'électrophysiologie avec enregistrements en champs et patch-clamp dans des tranches de cerveau de souris et des simulations informatiques, nous avons découvert que les axones du CA3 subissent un élargissement de leur diamètre après l'induction de la potentialisation à long terme (PLT). Nous démontrons que cet élargissement de diamètre augmente la vitesse de conduction des PA.

Dans l'ensemble, nos résultats indiquent que les axones peuvent réguler leur diamètre de manière dynamique changeant le délai de conduction des PA, ce qui modifie le timing du transfert d'information dans les circuits neuronaux. Cette étude suggère l'existence d'un nouveau type de mécanisme structurel dans le compartiment axonal jouant un rôle pour la plasticité neuronale.

**Mots clés:** axones, plasticité, super-résolution, STED

---

#### **Unité de recherche**

Institut Interdisciplinaire de Neurosciences - CNRS UMR5297  
146 rue Léo Saignat  
33077 Bordeaux Cedex

## Curriculum Vitae

### Education and degrees

- 06/2007 MSc in neuroscience, Université Paris 6, France  
06/2005 BSc in neuroscience, Université Bordeaux Segalen, France  
07/2004 *DEUG* in life sciences, Université Nantes, France

### Professional appointments

- 2010- PhD student, Interdisciplinary Institute for Neuroscience, Bordeaux  
2009-10 Lab manager, Prof. Valentin Nägerl, University of Bordeaux  
2007-09 Research assistant, Duke University, Prof. Anne West, Neurobiology Dept.,  
Durham, USA  
2005-07 Research assistant, Université Bordeaux Segalen

### Teaching

- 08/2012 Teaching assistant at Cold Spring Harbor Laboratory course on *Imaging Neural Structure and Function*, Cold Spring Harbor , USA  
09/2011 Teaching assistant at European Synapse Summer School, Bordeaux  
09/2006 Teaching assistant at European Synapse Summer School, Bordeaux

### Training

- 05/2011 Frontiers in Neurophotonics International Summer School, Québec, Canada

### Selected talks

- 01/2014 IINS retreat, Hendaye, France  
10/2013 3<sup>rd</sup> Annual conference of the Marie-Curie training network (SyMbaD), Milan,  
Italy  
11/2012 2<sup>nd</sup> Annual conference of the Marie-Curie training network (SyMbaD),  
Alicante, Spain  
10/2011 1<sup>st</sup> Annual conference of the SyMbaD program, Balaton, Hungary

### Poster presentations

- 11/2013 Society for Neuroscience, San Diego, USA  
10/2013 Frontiers in Neurophotonics, Bordeaux, France  
05/2013 ENCODS conference, Bordeaux, France

- 07/2012 FENS forum, Barcelona, Spain  
10/2011 European Synapse Meeting, Balaton, Hungary

### **Fellowships**

- PhD fellowship from the Conseil Region Aquitaine (3 years)  
PhD extension fellowship from the Fondation Recherche Médicale (FRM) (9 months)

### **Publication list:**

Bethge P.<sup>1,2</sup>, **Chéreau R.**<sup>1,2</sup>, Avignone E.<sup>1,2</sup>, Marsicano G.<sup>3</sup> and Nägerl U.V.<sup>1,2</sup>

#### **Two-photon excitation STED microscopy in two colors in acute brain slices**

Biophysical Journal 104(4): 778-785 (2013)

1. Univ. Bordeaux, IINS, UMR 5297, F-33000 Bordeaux, France.
2. CNRS, IINS, UMR 5297, F-33000 Bordeaux, France.
3. Université de Bordeaux, INSERM U862 NeuroCentre Magendie, Bordeaux, France

**Chéreau R.**<sup>1,2</sup>, Cattaert D.<sup>3</sup>, Nägerl U.V.<sup>1,2</sup>

#### **Structural plasticity regulates propagation delays of action potentials in hippocampal axons. *In preparation***

1. Univ. Bordeaux, IINS, UMR 5297, F-33000 Bordeaux, France.
2. CNRS, IINS, UMR 5297, F-33000 Bordeaux, France.
3. Centre de Neurosciences Intégratives et Cognitives, CNRS-UMR 5228, Universités Bordeaux 1 et 2, Talence, France

Stigloher C.<sup>1</sup>, **Chéreau R.**<sup>2,3</sup>, Marty S.<sup>4</sup>, Nägerl UV.<sup>2,3</sup> and Bessereau J.L.<sup>5</sup>

#### **Dynamics of axonal structure revealed by a combination of electron tomography and STED super-resolution microscopy. *In preparation***

1. University of Würzburg, Biocenter/Theodor-Boveri-Institute, Electron Microscopy, Am Hubland, Würzburg 97074, Germany.
2. Univ. Bordeaux, IINS, UMR 5297, F-33000 Bordeaux, France.
3. CNRS, IINS, UMR 5297, F-33000 Bordeaux, France.
4. Institute of Biology of the Ecole Normale Supérieure, Inserm U1024, CNRS UMR8197, 75005 Paris, France.
5. Ecole Normale Supérieure, Biologie Cellulaire de la Synapse, and Institut National de la Santé et de la Recherche Médicale, U789, F-75005 Paris, France.

## Acknowledgements

This work was conducted at the Interdisciplinary Institute for Neuroscience (UMR 5297 CNRS) in Bordeaux in the group of Prof. U. Valentin Nägerl from October 2010 until June 2014.

First of all I would like to thank the committee members for the evaluation of this work, Dr. Dominique Debanne and Prof. Juan Burrone for their judgment, Dr. Andreas Frick and Prof. Peter Kind for their examination and Dr. Stéphane Oliet for being the chair of the defense.

I wish to thank my supervisor for giving me the opportunity to perform a PhD in his lab, supporting me over the years and giving me independence in my research. I started out in the team almost five years ago coming back from the US as a lab manager in a nascent team. It was a great experience to see the lab building up and the team growing over those years.

I thank Dr. Daniel Cattaert for his collaboration in the project. His modeling approach and our fruitful discussions have shed new light on the project.

I want to thank my buddy and brand new Doctor Philipp Bethge for joining me on our endeavor for an academic degree and countless off-hours in the streets of Bordeaux.

I also wish to thank for former members of the team: Fabien Nadrigny who always impressed me with his explanations every time I had a question about optics; Elena Avignone for biological discussions and her friendship; Martin Lenz, our expert in optics who I wish all the best in his next adventures.

Special thanks to the members of the team: Julie Angibaud, Misa Arizono, Mirelle Ter Veer, Lasani Wijetunge, Thomas Pfeiffer, Jan Tonnesen for contributing to the great atmosphere in the lab and their friendship. Thanks to Aude Panatier for very helpful discussions and her friendship. Thanks to all the members of the institute that are all contributing in making this laboratory such a nice place to work and live.

---

## TABLE OF CONTENT

<b>SUMMARY</b> .....	<b>I</b>
<b>Curriculum Vitae</b> .....	<b>III</b>
<b>Acknowledgements</b> .....	<b>V</b>
<b>TABLE OF CONTENT</b> .....	<b>1</b>
<b>List of Figures</b> .....	<b>3</b>
<b>ABBREVIATIONS</b> .....	<b>5</b>
<b>ABSTRACT</b> .....	<b>7</b>
<b>Résumé détaillé en français</b> .....	<b>8</b>
<b>INTRODUCTION</b> .....	<b>12</b>
<b>1 The axon as a transmission cable</b> .....	<b>12</b>
1.1 General introduction.....	12
1.2 The action potential.....	14
1.3 Classification of axons.....	15
1.4 Hippocampal axons.....	16
<b>2 Physiology and morphology of unmyelinated axons</b> .....	<b>19</b>
2.1 Organization of the axonal compartment.....	19
2.1.1 Axon initial segment.....	19
2.1.2 Axon shaft.....	21
2.1.3 Presynaptic compartment.....	24
2.2 Morphology of axons.....	25
2.2.1 Complexity of axonal arborization.....	25
2.2.2 Morphological heterogeneity of individual axons.....	28
<b>3 Conduction of action potentials</b> .....	<b>31</b>
3.1 Biophysical properties of axons.....	31

---

3.1.1	Cable theory.....	31
3.1.2	The Hodgkin-Huxley model for active propagation.....	34
3.1.3	AP propagation including geometrical constraints (Rall model) .....	34
3.1.4	Axon diameter and conduction velocity .....	36
3.2	Short-term dynamics of action potential propagation .....	38
<b>4</b>	<b>Long-term plasticity of unmyelinated axons .....</b>	<b>41</b>
4.1	Presynaptic changes associated with synaptic plasticity .....	41
4.1.1	Synaptic plasticity.....	41
4.1.2	Functional and structural modifications of the presynaptic compartment during synaptic plasticity.....	43
4.2	Activity-dependent plasticity of intrinsic excitability .....	45
4.3	Long-term change of action potential conduction velocity .....	47
<b>5</b>	<b>STED microscopy .....</b>	<b>48</b>
5.1	Basic optical principle of STED microscopy.....	48
5.1.1	PSF engineering.....	50
5.1.2	Improvement in spatial resolution .....	51
5.2	Development of STED imaging in living tissue .....	53
5.3	STED imaging of the dynamics of axon morphology.....	54
<b>6</b>	<b>Aims of the study .....</b>	<b>56</b>
	<b>MATERIALS AND METHODS .....</b>	<b>57</b>
	<b>RESULTS .....</b>	<b>69</b>
	<b>DISCUSSION .....</b>	<b>138</b>
	<b>REFERENCES.....</b>	<b>149</b>
	<b>APPENDIX.....</b>	<b>163</b>

---

## List of Figures

Figure 1: Drawings of stained neurons in the spinal cord with soma, nucleus, dendrites and axons, by Otto F K. Deiters, 1865.....	13
Figure 2: The structural organization of the hippocampus.....	18
Figure 3: Structural arrangement of actin, spectrin and associated proteins in the axon trunk.....	23
Figure 4: NeuroLucida reconstruction of a CA3 pyramidal neuron. ....	27
Figure 5: Morphology of boutons in the neocortex. ....	29
Figure 6: Electron micrograph and 3D reconstruction of CA3 axons. ....	30
Figure 7: Electrical model of a passive axonal cable.....	32
Figure 8: Expression mechanism of presynaptic LTP and LTD: prototypical mechanisms.....	44
Figure 9: Simplified Jablonski diagram of GFP for fluorescence and stimulated depletion. ....	49
Figure 10: Point spread function engineering for STED microscopy.....	51
Figure 11: Stimulated emission depletion microscopy reveals densely packed nitrogen-vacancy centres in diamond. ....	53
Figure 12: Local infection CA3 pyramidal neurons using sinbis-GFP.....	59
Figure 13: Optical design of the home-built inverted STED microscope for opto-physiology in brain slices. ....	63
Figure 14: Structural plasticity of axon shafts and boutons during LTD.....	131
Figure 15: The inhomogeneous distribution of fluorophores in the axon structure makes intensity-based measurement of diameters inaccurate. ....	132
Figure 16: The imaging of axonal structures was performed in non-saturated conditions. ....	133
Figure 17: The FWHM measurement does not depend on the intensity of the signal.....	134

Figure 18: Geometric ratio measurement on the proximal axon tree. .... 137

Figure 19: Proposed mechanism of axonal diameter enlargement. .... 143

Figure 20: Hippocampal axons may serve as dynamic delay lines for information transfer. .... 148

---

## ABBREVIATIONS

2P microscopy	Two-photon microscopy
ACSF	Artificial cerebrospinal fluid
AIS	Axon initial segment
AMPA	2-amino-3-(3-hydroxy-5-methyl-isoxazol-4-yl)propanoic acid
AnkG	Ankyrin G
AP	Action potential
APD	Avalanche photodiode
APV	(2 <i>R</i> )-amino-5-phosphonovaleric acid; (2 <i>R</i> )-amino-5-phosphonopentanoate
CA1	Cornu ammonis 1
CA3	Cornu ammonis 3
CaM	Calmoduline
Cav channel	Voltage-gated calcium channel
$C_m$	Specific membrane capacitance
$c_m$	Membrane capacitance
CNS	Central nervous system
DG	Dentate gyrus
EDTA	Ethylenediaminetetraacetic acid
EPSP	Excitatory postsynaptic potential
fEPSP	Field excitatory postsynaptic potential
FWHM	Full width half-maximum
GABA	Gamma-aminobutyric acid
GBSS	Gey's balanced salt solution
GFP	Green fluorescent protein
GPCR	G protein coupled receptor
GR	Geometric ratio
HFS	High-frequency stimulation
KAR	Kainate receptor
Kv channel	Voltage-gated potassium channel
KYN	Kynurenic acid

---

$\lambda$	Length constant or wavelength
LTD	Long-term depression
LTP	Long-term potentiation
MEA	Multi-electrode array
NA	Numerical aperture
Nav channel	Voltage-gated sodium channel
NMDA	<i>N</i> -Methyl- <i>D</i> -aspartic acid
OPO	Optical parametric oscillator
PKC	Protein kinase C
PMT	Photomultiplier tube
PNS	Peripheral nervous system
PSF	Point spread function
$R_i$	Specific axoplasmic capacitance
$r_i$	Axoplasmic resistance
$R_m$	Specific membrane resistance
$r_m$	Membrane resistance
SNARE	Soluble N-ethylmaleimide-sensitive factor Attachment protein Receptor
STED	Stimulated emission depletion
STORM	Stochastic optical reconstruction microscopy
$\tau$	Time constant
TBS	Theta-burst stimulation

## ABSTRACT

Millisecond timing precision in the transfer of information between neurons is essential for the synchrony and plasticity of neural circuits in the brain. Axons are neuronal extensions that ensure the communication via brief electrical impulses called action potentials (AP). Because they are unmyelinated and are extremely thin, hippocampal axons propagate APs slowly and thus generate long delays of conduction (up to 100 ms) that are traditionally considered invariant. However, recent studies have shown that activity changes the morphology of axons and modulate the latency of transmission, thus raising the question whether axons undergo activity-dependent structural changes that could influence the propagation of APs.

The diameter of hippocampal axons (ranging between 100-350 nm) are usually too thin to be properly resolved by conventional light microscopy. However, the development of super resolution STED imaging now enables the observation of their detailed morphological dynamics in living tissue.

Using a novel combination of STED microscopy, field recordings, patch-clamp electrophysiology in mouse brain slices and computer simulations we discovered that CA3 axons undergo long-lasting enlargement in their diameter after the induction of long term potentiation (LTP). We provide strong evidence that this diameter enlargement increases AP conduction velocity.

Taken together, our findings indicate that axons can dynamically tune AP propagation delays by changing their diameters, thereby altering the timing of information transfer in neural circuits. This study suggests a novel and powerful structural mechanism for neural plasticity.

## Résumé détaillé en français

Un neurone est une cellule excitable électriquement et hautement polarisée qui reçoit, traite et transmet les informations au moyen de signaux électriques et chimiques. Les neurones peuvent se connecter les uns aux autres par l'intermédiaire de contacts appelés synapses et former des réseaux neuronaux. Typiquement, un neurone est composé de trois compartiments, un corps cellulaire (soma), une arborisation dendritique qui reçoit les signaux d'autres neurones et l'axone qui envoie l'information vers les neurones suivants.

L'axone est une extension protoplasmique mince et allongée qui part du corps cellulaire et qui s'étend jusqu'aux terminaisons nerveuses. Sa fonction est de conduire l'information par l'intermédiaire d'impulsions électriques, généralement des potentiels d'action (PA) partant du soma, se propageant pour atteindre différents neurones.

Traditionnellement les axones sont perçus comme des transmetteurs fiables de l'information générée au soma en véhiculant un code purement digital. Toutefois, les examens attentifs de l'organisation structurale, de la composition en canaux et des différentes propriétés fonctionnelles des axones ont commencé à remettre en question cette vision simpliste. En effet, de nombreuses études ont démontré que la structure de l'axone peut exercer une influence profonde sur l'intégration d'entrée neuronale et la modulation de sortie, indiquant ainsi que le répertoire des axones fonctionnel est beaucoup plus large qu'on ne le pensait traditionnellement.

Un timing précis de la décharge neuronale est essentiel pour la synchronisation du réseau et la plasticité circuit dans le cerveau. Une synchronisation à l'échelle de la milliseconde est extrêmement importante dans l'intégration des signaux excitateurs et inhibiteurs qui module

la fonction de sortie d'un neurone. En outre, la coïncidence entre les événements synaptiques et les décharges dendritiques est connue pour réguler la force de la transmission synaptique dans un processus communément appelé la plasticité dépendante du timing de décharge (en anglais: spike-timing dependent plasticity ou STDP). En ce qui concerne ces fonctions importantes du cerveau, le délai de conduction axonale des potentiels d'action (PA) est un paramètre souvent négligé, mais peut être très long. Du moment de l'initiation jusqu'à la terminaison nerveuse présynaptique, ce délai peut varier sensiblement d'une à plusieurs centaines de millisecondes.

Dans le cerveau des mammifères, la vitesse et la fiabilité de propagation des PA peuvent être assurées de deux manières : un large diamètre axonal ou la myélinisation. Cependant, la plupart des axones dans l'hippocampe sont non-myélinisés et ont des diamètres très minces qui expliquent les importants délais de propagation. Par exemple, en plus de leur topologie très ramifiée et de leur morphologie irrégulière du aux boutons présynaptiques dits 'en passants', les axones CA3 présentent de longues branches collatérales (jusqu'à 20 mm) et des diamètres compris entre 100-300 nm.

La difficulté d'isoler et d'évaluer les propriétés biophysiques de ces axones minces a forgé notre point de vue où le délai de la conduction axonale est un paramètre fixe qui ne contribue pas au codage de l'information. Néanmoins, quelques études indiquent que le délai de conduction des PA pourrait être régulé de manière dynamique. Des études de microscopie à deux photons ont révélé un important remodelage structurel des connexions synaptiques dans l'hippocampe durant des protocoles de plasticité synaptique. Cela représente la preuve la plus convaincante que la morphologie des axones est sensible à l'activité qui pourraient donc modifier la vitesse de conduction des PA. De plus, une régulation dynamique du diamètre

axonal a déjà été suggérée par plusieurs études qui ont signalé des changements dans les latences synaptiques durant l'activité et pourrait être liés à un changement de délais axonaux.

Parce que la microscopie optique conventionnelle ne parvient pas à résoudre correctement la morphologie des axones allant bien au-dessous de 500 nm et la microscopie électronique ne peut pas être combinée avec des tests fonctionnels, c'est une possibilité encore inexplorée de savoir si minces axones non-myélinisés subissent des changements de diamètre dépendants de l'activité qui pourraient influencer la propagation des PA.

Par conséquent, la microscopie à super résolution STED, dont le pouvoir de résolution n'est pas limitée par la diffraction de la lumière, est bien adaptée pour l'imagerie des axones dans des tranches de cerveau vivant.

Dans cette étude, nous avons examiné si les axones peuvent être régulés de manière dynamique par l'activité. Nous avons combiné la microscopie STED, l'électrophysiologie avec des enregistrements d'activité de champs et de neurone unique en 'patch-clamp' sur des tranches en culture de cerveau de souris et des simulations informatiques afin de corrélérer les changements morphologiques dépendants de l'activité d'axones de la vitesse de conduction des PA. Nos résultats montrent que de façon concomitante avec l'induction de protocoles d'activité de potentialisation synaptique, le diamètre des axones s'élargit et la vitesse de conduction des PA augmente AP de conduction. Ces données suggèrent l'existence d'un nouveau type de plasticité par laquelle les diamètres des axones contrôlent dynamiquement les délais synaptiques dans les réseaux neuronaux.

Le travail de cette thèse comprend également le développement d'un nouveau genre de microscope à super-résolution STED qui permet d'observer les fines structures du système nerveux plus profondément dans des tranches de cerveau adulte mais également sur animal

vivant. Les premiers développements de microscopes STED étaient basés sur une excitation à simple photon qui limite les observations sur les structures superficielles de culture de neurones dissociés ou de tranches fines de cerveau en culture. En revanche, la microscopie deux-photon est actuellement la méthode de choix pour l'imagerie dans des échantillons vivant épais que ce soit dans les tranches aigues ou sur animal vivant. Etant une méthode de microscopie photonique classique, la résolution spatiale d'un microscope deux-photon est limitée à environ 350 nm à cause de la diffraction de la lumière, et donc ne permet pas l'observation détaillée d'importantes structures neuronales comme les épines dendritiques ou les axones.

Nous avons construit un nouveau microscope basé sur une excitation à deux photons et à déplétion stimulée pulsée. Sa polyvalence permet l'imagerie des fluorophores classiquement utilisés comme la GFP, YFP et Alexa488. Nous illustrons le potentiel du microscope pour la résolution de structures cérébrales minces telles que des épines dendritiques, les axones et les prolongements microgliaux dans des tranches de cerveau aigues à plus de 50 micromètres de la surface. Nous montrons aussi le potentiel de l'imagerie super résolution à deux couleurs en utilisant des algorithmes de séparations de canaux appelé 'unmixing linéaire'. Sa conception verticale et son objectif à eau à grande distance de travail offre un accès pour combiner l'imagerie de super-résolution avec enregistrement électrophysiologique et permet aussi une évolution vers l'imagerie sur animal vivant.

# INTRODUCTION

## 1 The axon as a transmission cable

### 1.1 General introduction

A neuron is an electrically excitable and highly polarized cell that receives processes and transmits information through electrical and chemical signals. Neurons can connect to each other via contacts called synapses and form neuronal networks. Typically, a neuron is composed of 3 compartments, the cell body (or soma), the input region called dendrites and the output region called axon.

The axon (from Greek, axis) is a thin and elongated protoplasmic protrusion that projects away from the cell body to terminal endings. Its function is to conduct information via electrical impulses, typically action potentials (APs) from the soma to different neurons, muscles or glands. Its discovery, during the 19<sup>th</sup> century, is usually attributed to the German anatomist Otto Friedrich Karl Deiters (Deiters, 1865) being the first to distinguish the axon from the dendrite which is the other type of neuronal protrusions that receive information from other neurons via synapses (Figure 1). The functional role of the axon as the output compartment of the neuron was first suggested by the pioneer work of the Spanish anatomist Santiago Ramón y Cajal (Ramon y Cajal, 1897). A few years later, Julius Bernstein (1902) correctly postulated the fundamental biophysical properties of the neuronal membrane. He used the term “membrane breakdown” to describe the transient loss of membrane negativity during the propagation of an AP. In the 1930’s, Cole and Curtis experimentally measured the change in membrane resistance in the squid giant axon during the passage of an AP (Cole & Curtis, 1939). This work was then followed by Hodgkin, Huxley and Eccles who received

the Nobel prize in physiology and medicine in 1963 for the discovery the ionic mechanisms involved in the excitation and inhibition of the nerve membrane (Hodgkin, 1939).

Ever since, axons were seen as reliable transmission cables, conveying a purely digital code, where information is composed of the rate and timing of stereotypical APs traveling to downstream targets. However, close examination of the structural organization, various channel compositions and functionally diverse properties of axonal arbors has begun to challenge this simplistic view. Indeed, numerous studies have demonstrated that the axon structure can exert profound influence on neuronal input integration and output modulation, thus indicating that the functional repertoire of axons is much broader than traditionally thought (Bucher & Goillard, 2011; Debanne, 2004; Debanne et al, 2011).

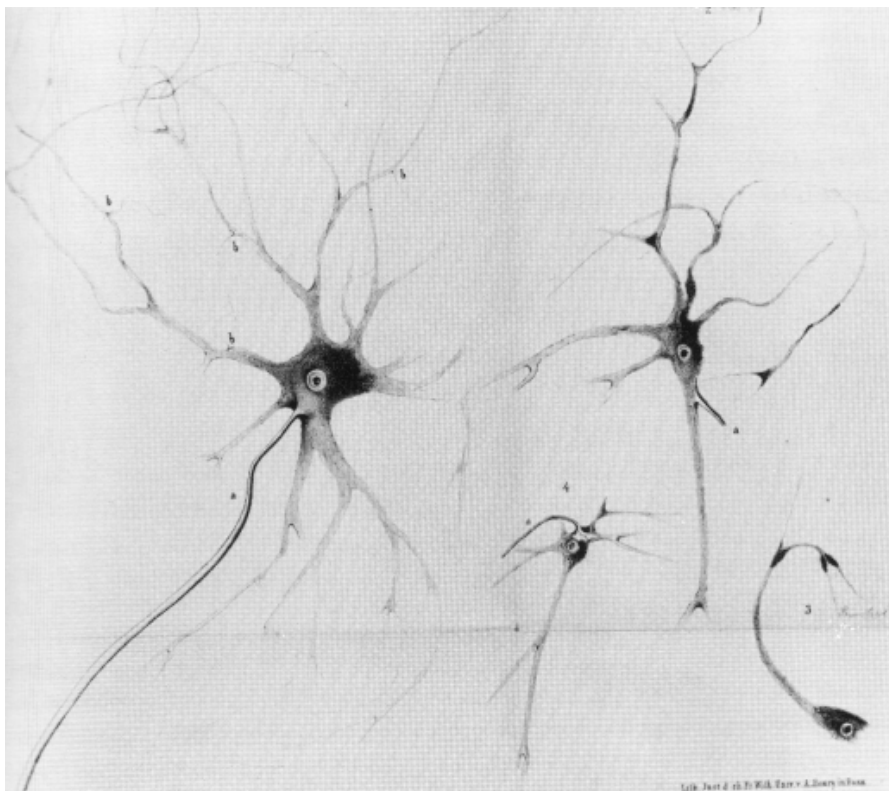


**Figure 1: Drawings of stained neurons in the spinal cord with soma, nucleus, dendrites and axons, by Otto F K. Deiters, 1865.**

## 1.2 The action potential

When an excitatory synapse is activated, an excitatory postsynaptic potential (EPSP) is generated and transiently depolarize the membrane. If the depolarization reaches a certain threshold such as through the simultaneous activation of several synapses, the neuron fires an AP which will travel down the axon. In contrast to EPSPs that spreads electrotonically; APs actively propagate along axons due to the voltage dependence of their ionic conductances. This makes the AP a self-supporting or regenerative process.

The AP is an electrical impulse propagating rapidly along the axon. They are generated by sequential opening of various voltage-gated sodium and potassium channels (Nav and Kv channels, respectively) at the cell membrane. When the membrane is at its resting potential, Nav channels are closed but rapidly open when the potential reaches a specific threshold. This produces an inward flow of positively charged, sodium ions that quickly increase the membrane potential (depolarization phase). This depolarization causes a change of membrane polarity which leads to the inactivation of the Nav channels. The depolarization also activates Kv channels allowing an outward flow of potassium ions returning the membrane potential to its resting potential (repolarisation phase). Their slow inactivation kinetics produces an undershoot called after-hyperpolarisation. For chemical synapses, when the AP arrives at the presynaptic terminal, the change in membrane potential activates voltage-gated calcium channels (Cav channels) creating an inward current of calcium ions into the presynaptic terminal. Typically, this rise of calcium triggers the fusion of vesicles, liberating neurotransmitters into the synaptic cleft. As a consequence, the neurotransmitter molecules activate postsynaptic receptors which produce post synaptic currents.

A single AP is followed by an absolute refractory period during which another AP cannot be evoked, and a relative refractory period during which a stronger stimulus is required to elicit an AP. At the end of the depolarization phase, when Nav channels are closing, they enter in an inactivated state before going back to a resting state which makes them insensitive to any change in membrane potential – this phase corresponds to the absolute refractory period. This aspect is mainly responsible for the unidirectional propagation of AP. Indeed, in a propagating AP, the segment of axon behind the actively spiking part is refractory to the change in potential. The segment in front, yet not having been activated, is capable of being stimulated by the depolarization from the AP.

After the absolute refractory period, the axon undergoes the relative refractory period where activation of Nav channels can induce APs, albeit only after strong stimulation. This is due to an outward flow of potassium ions as a fraction of Kv channels are still open (slow kinetics of the Kv channels).

### **1.3 Classification of axons**

Across species, organs and even within the same anatomical region, axons are very diverse in their structures and properties. Two main types of axons can however be distinguished: unmyelinated and myelinated axons. Myelinated axons refer to axons that are enwrapped by a myelin sheet from Schwann cells in the peripheral nervous system (PNS) or the oligodendrocytes in the central nervous system (CNS). These axons conduct electrical impulses much faster than their unmyelinated kin. The myelin sheath, arranged in segments along the axon and separated by the nodes of Ranvier, acts as an electric insulator preventing the electrical current from leaving the axon and hence, restricting the ionic exchanges to the nodes of Ranvier. Indeed, when impulses propagate continuously as waves along

unmyelinated axons, relying on channel kinetics, they seem to hop from node to node in a combination of fast electrotonic spread and active propagation. This phenomenon is called the saltatory conduction and dramatically increases conduction speed.

In the mammalian CNS, the classification into grey and white matter arises from a whiteness of the myelin revealing the regions containing the fast conducting fibers. By opposition, the grey matter that does not contain myelin gets its color from the neuronal cell bodies, neuropil, glial cells and capillaries. Grey matter is found at the surface of the cerebral cortex and cerebellum, as well as in the depths of the cerebrum (thalamus; hypothalamus; subthalamus, basal ganglia - putamen, globus pallidus, nucleus accumbens; septal nuclei), cerebellar (deep cerebellar nuclei - dentate nucleus, globose nucleus, emboliform nucleus, fastigial nucleus), brainstem (substantia nigra, red nucleus, olivary nuclei, cranial nerve nuclei) and spinal grey matter (anterior horn, lateral horn, posterior horn). The white matter is composed of bundles of myelinated fibers connecting the various grey matter areas. For instance, the corpus callosum is the largest white matter structure of the brain and its role is to facilitate interhemispheric communication.

## **1.4 Hippocampal axons**

The hippocampus, part of the grey matter, is one of the most studied regions of the brain. There are two main reasons for this great interest. First, it is now well established that the hippocampus has a critical role in learning and memory processes. For instance, the hippocampus is involved in remembering information that can be described in a propositional or declarative manner (Andersen, 2007). During the last decades, all the work that has focused on the function of the hippocampus has shaped our current concepts about memory organization in the brain. The second reason that gathers attention around the hippocampus is

its extremely well oriented cellular organization that makes the hippocampal formation relatively easy to study (Figure 2). Indeed, neurons are organized in densely packed layers that are easily recognizable at low magnification. In this organization, two types of excitatory glutamatergic cells can be found: the pyramidal neurons and granule cells. The cell bodies of the granule cells compose the granular layer of the dentate gyrus (DG) whereas the cell bodies of pyramidal neurons lie in a single densely packed layer called stratum pyramidale that can be divided into four regions: Cornu Ammonis 1, 2, 3 and 4 (CA1 to 4). These cells form a tri-synaptic excitatory circuit where cells from entorhinal cortex send their axons through the perforant path to the DG granule cells. The granule cells contact CA3 pyramidal neurons via mossy fiber collaterals. Then, CA3 neurons send axonal projections called Schaffer collaterals (named after the Hungarian anatomist-neurologist Károly Schaffer) that contact pyramidal neurons of the CA1 layer (Andersen, 2007).

The two types of connections DG to CA3 and CA3 to CA1 involve two very distinct types of synapses. The mossy fibers display large varicosities (5-10  $\mu\text{m}$ ) named mossy fiber boutons due to their cushiony appearance. They form synapses with CA3 pyramidal cells in the proximal part of their dendrites on elaborate spines called “thorny excrescences”. The CA3-CA1 connection involves a more typical excitatory glutamatergic synapse in the cortex. For this reason, many scientists use the Schaffer collateral synapse as a sample synapse, to study and identify the rules by which synapses undergo plastic changes.

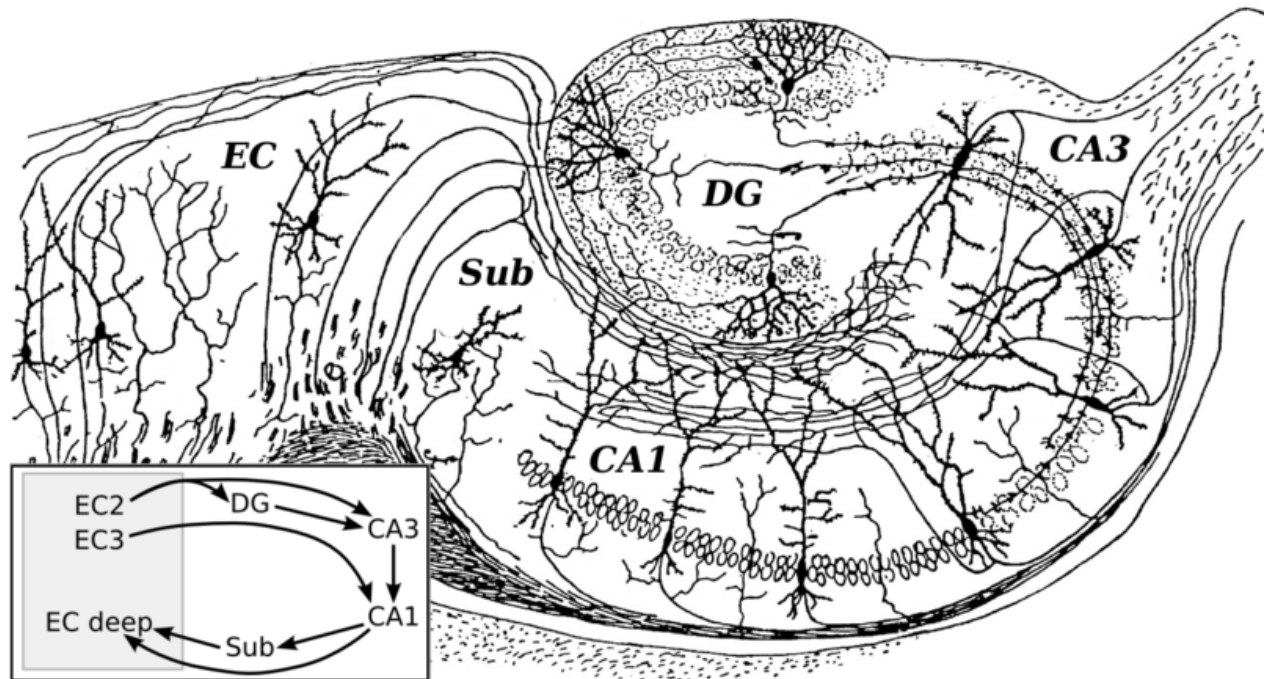


**Figure 2: The structural organization of the hippocampus.**

*The dentate gyrus (DG) that exclusively receives inputs from the entorhinal cortex (EC) is composed of granule cells. Typically, granule cells project to the CA3 area via the morphologically distinct mossy fibers. The CA3 is composed of excitatory pyramidal neurons and sends projections called Schaffer collaterals to the CA1 region. Similarly, CA1 is composed of excitatory pyramidal cells that are projecting toward the Subiculum and other layers of the entorhinal cortex.(modified drawing from Ramon y Cajal, 1911)*

## 2 Physiology and morphology of unmyelinated axons

### 2.1 Organization of the axonal compartment

#### 2.1.1 Axon initial segment

The axon initial segment (AIS) is the site of initiation of the AP. This highly excitable axonal compartment was first identified by the Swiss Rudolf Alber von Kölliker (Kölliker, 1849) and the German Robert Remak (Remak, 1855). The AIS has a variable length of around 25 $\mu$ m and can be located directly at the axon hillock or up to tens of microns away from the hillock. The Nav and Kv channels composition of the AIS as well as its length and distance from the soma contributes to the spiking properties of the neuron. The AIS is characterized by a high density of Nav and Kv channels compared to the rest of the axon and the adjacent cell body. Combining electrophysiological recordings and computer simulations, sodium channels density in the AIS was evaluated to be 20 to 1 000 fold higher than in the soma or dendrite (Mainen et al, 1995; Moore et al, 1983; Rapp et al, 1996) resulting in a boost of inward sodium current that initiates the AP.

The structural organization of the AIS is very different from the rest of the axon. Electron microscopy observations indicated several specific features of AIS. The AIS is rich in microtubule bundles and their membrane is rich in proteins similar to what was observed in the nodes of Ranvier of myelinated fibers (Bender & Trussell, 2012; Palay et al, 1968). Later, electrophysiological and immunocytochemical techniques provided evidence for a specific arrangement of Na<sup>+</sup>, K<sup>+</sup> and Ca<sup>2+</sup> channels that determines action potential generation and shape. Indeed, the distribution of Nav channel subtypes in the AIS is highly polarized. Whereas dense clusters of fast activating and fast inactivating Nav1.6 channels are located at

the distal part of the AIS to promote AP initiation, the proximal Nav1.2 channels contribute to AP back-propagation at the soma and dendrites (Hu et al, 2009). In the same way, Kv channels are distributed at high densities in the AIS. In layer 5 of the cortex and in CA3 pyramidal cells, Kv1.1 and 1.2 are mainly located distally, together with Nav1.6 (Lorincz & Nusser, 2008). Other neuron types have different Kv1 subunit distribution and even though it is known that Kv1.1 and 1.2 have different kinetics (Grissmer et al, 1994) it remains unclear how the difference in Kv subunit composition affects AIS function. In addition, Kv7.3 and Kv7.4 are also present in the AIS of CA3 and CA1 pyramidal neurons and were shown to play a critical role controlling the resting membrane potential and action potential threshold (Pan et al, 2001; Shah et al, 2002; Shah et al, 2008; Yue & Yaari, 2006). More recently, Bender et al., reported the presence of Cav channels in the AIS and demonstrated their implication in AP initiation and control of AP firing pattern (Bender et al, 2010; Bender & Trussell, 2009; Bender et al, 2012).

Initial segments also contain high concentration of GABA<sub>A</sub> receptors (Brunig et al, 2002; Christie & De Blas, 2003). Indeed, GABAergic Chandelier cells project and form axo-axonic contacts on the AIS of hundreds of principal cells acting as “master breakers” of excitatory circuits.

The molecular organization of the AIS is mainly dependent of the scaffolding protein Ankyrin G (AnkG). Shortly after the beginning of the axon development, AnkG is targeted with a high degree of specificity to the proximal part of the axon and underlies the AIS formation. The localization of the AIS is mediated by  $\beta$ -IV-spectrin, a protein associated to the actin cytoskeleton that binds to AnkG (Yang et al, 2007). It is also well established that AnkG retains Nav channels and is therefore responsible for their high density in the AIS (Jenkins & Bennett, 2001; Zhou et al, 1998). The fine tuning of Nav localization in the AIS is

thought to also depend on auxiliary proteins such as Nav $\beta$  and intracellular fibroblast growth factors (iFGFs) that promote their surface expression (Grieco et al, 2005; Laezza et al, 2007).

### **2.1.2 Axon shaft**

The axon trunk is the main part of the axon. Its role is to conduct APs generated at the AIS down to the presynaptic terminal. The channel composition in the distal axon can be very diverse. In the widely studied squid giant axon or more generally for invertebrates, the literature has described initiation and propagation typically based on only a few subtypes of Nav channels giving rise to a fast sodium current and few Kv channels that produce a delayed rectifier potassium current (Goldin, 2002; Hodgkin & Huxley, 1952a; Loughney et al, 1989). However, in mammals, it is well known that many axons, myelinated or unmyelinated, central or peripheral, are equipped with many more Nav and Kv channel subtypes. Yet, the role of every channel subtype, their cooperative effect and the consequence for AP propagation are poorly understood. In thin unmyelinated axons, even less is known as their small diameter increases the difficulty to detect the channel composition reliably by immunolabeling. Therefore, the presence of channel types should be determined indirectly performing extracellular recordings and pharmacology (Moalem-Taylor et al, 2007; Sasaki et al, 2011; Sasaki et al, 2012a).

Nevertheless immunohistochemical labeling has revealed that in CA3 Schaffer collateral axons, mainly contain Nav1.2 (Gong et al, 1999) and Kv1.2 (Veh et al, 1995), but it believed that many more isoforms populate the axon with variable expression levels and localizations. This diversity is reflected in the number of genes that encode for the eleven channel types named Nav1.1 through Nav1.9 and two additional Nax for which the function remain undefined. Although the expression and distribution of Nav channel subtypes in the axon is not well understood, several studies indicate various behavior in the gating properties of Nav

channels that populate the axon. For instance, it was demonstrated that a sodium current can be activated upon hyperpolarized membrane potential and inactivate slowly (Baker & Bostock, 1997; Stys et al, 1993; Tokuno et al, 2003). Such regulation in sodium current was shown to be important for sub threshold excitability and repetitive firing (Bostock & Rothwell, 1997; French et al, 1990; McIntyre et al, 2002).

The diversity is even higher concerning Kv channels. Due to their overall slower kinetics compared to Nav channels, they have a critical influence on the AP waveform and excitability during repetitive firing. In unmyelinated central axons, Kv1.1, Kv1.2 (producing sustain currents) and Kv1.4 (producing transient currents) are widely expressed. They usually form heteromeric complexes within the family as well as with other auxiliary subunits like Kv3.4 and produce a wide variety of gating properties (Rettig, 1994; Trimmer and Rhodes, 2004).

Our view on the structural organization of the cytoskeleton of the axon trunk has completely changed recently. Using immunolabeling techniques combined with superresolution STORM (Stochastic Optical Reconstruction Microscopy) imaging of cortical neurons, Xu et al., have discovered a ring-shaped actin arrangement inside axons in contrast to the linear bundles in dendrites (Xu et al, 2013). Surprisingly, those actin-rings were found to be evenly spaced along the axon with a periodicity of ~180-190 nm. In addition, they found a similar periodic arrangement for spectrin, adducin and Nav (Figure 3). This new information about the unique cytoskeleton layout in axons will certainly change our understanding on how axons develop and how electrical signals propagate within this compartment.

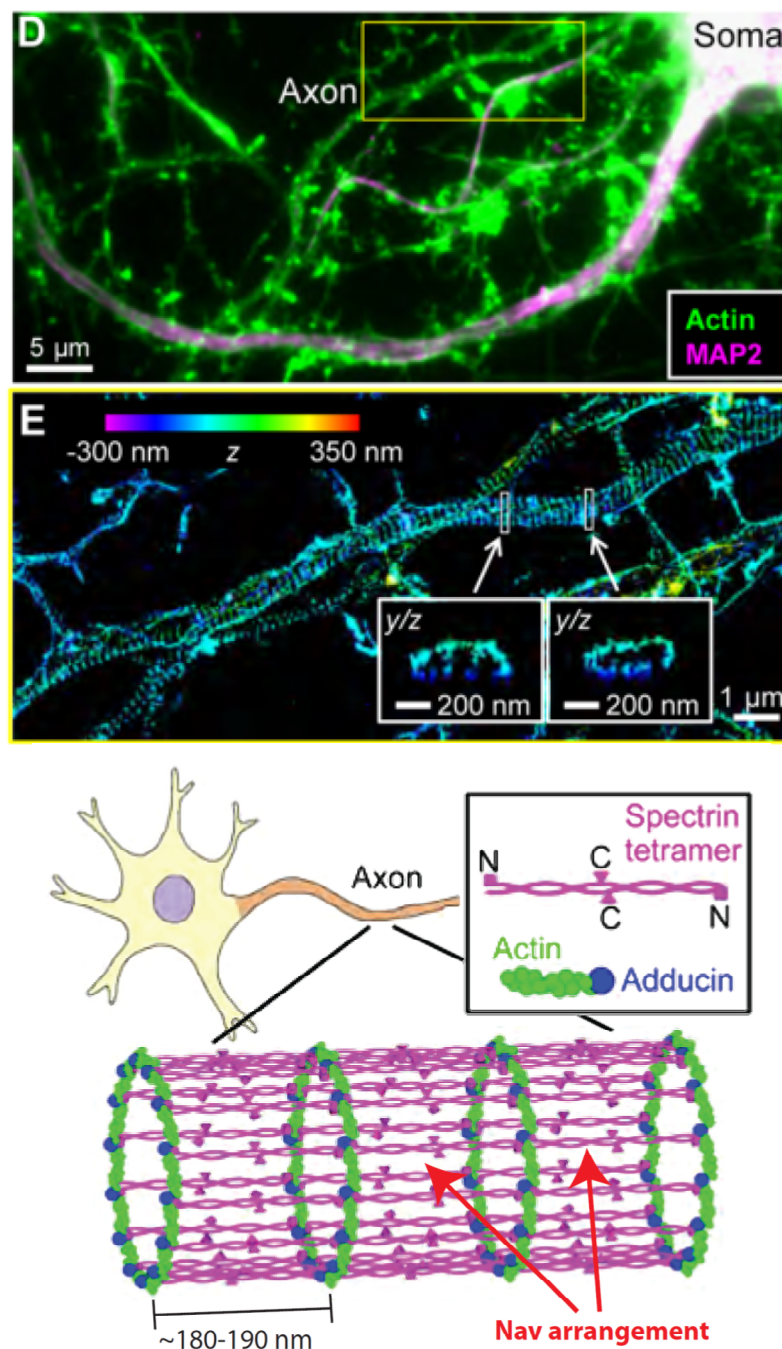


**Figure 3: Structural arrangement of actin, spectrin and associated proteins in the axon trunk.**

(Top) Super resolution STORM microscopy reveals the periodic structural organization of actin in the axon. Conventional fluorescence image of the actin (green) and dendritic marker, MAP2 (magenta), in a cultured hippocampal neuron fixels at 7 DIV (D). 3D STORM image of actin in a region containing axons (E). (Bottom) Periodic organization of the cytoskeleton, with actin that forms rings and its associated proteins in the axon trunk. (adapted from Xu et al., 2013)

### 2.1.3 Presynaptic compartment

The most fundamental function of the presynaptic compartment is to regulate the release of neurotransmitter via the fusion of synaptic vesicles with the presynaptic plasma membrane. Typically, the presynaptic compartment of a chemical synapse is composed of synaptic vesicles, an active zone, scaffolding molecules, and trans-synaptic adhesion molecules (Li & Jimenez, 2008; McAllister, 2007).

The number of synaptic vesicles ranges between hundreds to thousands and can be divided into the readily releasable pool, located in the active zone, and the reserve pool. The segregation of those pools is mediated by the calcium sensitive phosphatase, calcineurin. The activation of calcineurin through the elevation of  $Ca^{2+}$  concentration in the presynaptic bouton, dephosphorylate synapsin that is responsible for the clustering of the reserve pool vesicles, thus allowing vesicles to migrate to the active zone and become part of the readily releasable pool (Cesca et al, 2010). The active zone, sometimes called presynaptic density, is the site of the presynaptic compartment mediating neurotransmitter release. It is formed by the presynaptic membrane and a protein dense material that tightly integrate in the membrane whereby neurotransmitter vesicles are tethered. The fusion of neurotransmitter vesicles at the membrane is highly regulated and utterly depends on the formation of a protein assembly called the SNARE complex (Soluble N-ethylmaleimide-sensitive factor Attachment protein Receptor complex). The increase of presynaptic  $Ca^{2+}$ , following the arrival of an AP, forces vesicles to fuse to the plasma membrane due to a change in conformation of molecules in the SNARE complex.

The assembly and stability of the synaptic cleft is mediated by trans-synaptic adhesion molecules that are thought to regulate structure and function of mature synapses during activity (Knott et al, 2002; Toni et al, 1999).

The elevation of calcium concentration in the presynaptic boutons is mediated by Cav channels present at their membrane. Pharmacological effects of specific  $\text{Ca}^{2+}$  blockers has allowed to determine that Cav2.1 constitute the majority of the Cav channels involved in transmitter release (Burke et al, 1993; Geer et al, 1993; Llinas et al, 1989; Mintz et al, 1992; Turner et al, 1992; Uchitel et al, 1992), Cav2.2 constitutes only by a smaller fraction (Burke et al, 1993; Pocock et al, 1992; Reynolds et al, 1986). In addition, Cav1.2 channels were found to be sparsely expressed in hippocampal presynaptic boutons (Tippens et al, 2008).

The presynaptic compartment also displays various types of receptors that act as modulators of the synaptic transmission. G protein coupled receptors (GPCRs) such as  $\text{GABA}_B$ , cannabinoid and adenosine receptors can either inhibit Cav channels or enhance Kv channels activation leading to the inhibition of transmitter release. Ionotropic glutamate receptors were also found to be present at the presynaptic compartment and also modulate transmitter release. For instance, kainate receptors (KARs), AMPAR, NMDAR exert presynaptic action by modulating transmitter release at certain synapses in the CNS (Engelman & MacDermott, 2004; Kamiya, 2002; Rossi et al, 2008; Rusakov, 2006).

## **2.2 Morphology of axons**

### **2.2.1 Complexity of axonal arborization**

Axons can contact neighboring cells that are few tens of microns away or project to other brain areas several centimeters away. Some neurons have a very simple axonal morphology, for instance, granule cell axons in the cerebellum are characterized by a single T-shaped branch node from which two parallel fibers extend. Others, like basket cell interneurons, that are present in the molecular layer of the cerebellum, the hippocampus and the cortex, densely collateralized in a confined area of tens of microns (Andersen, 2007). This topology allows

basket cells to synchronize firing of hundreds of principal cells through their divergent axon (Cobb et al, 1995).

CA3 axons are traditionally seen as simple axons projecting in the CA1 area and are also known as Schaffer collaterals. In fact, CA3 pyramidal cells give rise to highly divergent projections in all areas of the hippocampus. *In vivo* reconstructions of CA3 axons in the rat have revealed their complex topology (Ishizuka et al, 1990; Ropireddy et al, 2011; Wittner et al, 2007) (Figure 4). These axons can form more than 350 branch points and contact 20 000 to 60 000 neurons (Andersen et al, 1994; Li et al, 1994; Major et al, 1994; Wittner et al, 2007). They contact neurons in the CA3, CA2 (associational connections) accounting for 1/3 of the connections, CA1 (Schaffer collaterals) representing 2/3 of the connections, and a small fraction in the dentate gyrus, in both the ipsilateral and contralateral hippocampus via the commissural pathway. The total length of the CA3 axon collaterals can exceed half a meter while its collaterals length ranges between hundreds of microns up to 20 mm(Wittner et al, 2007).

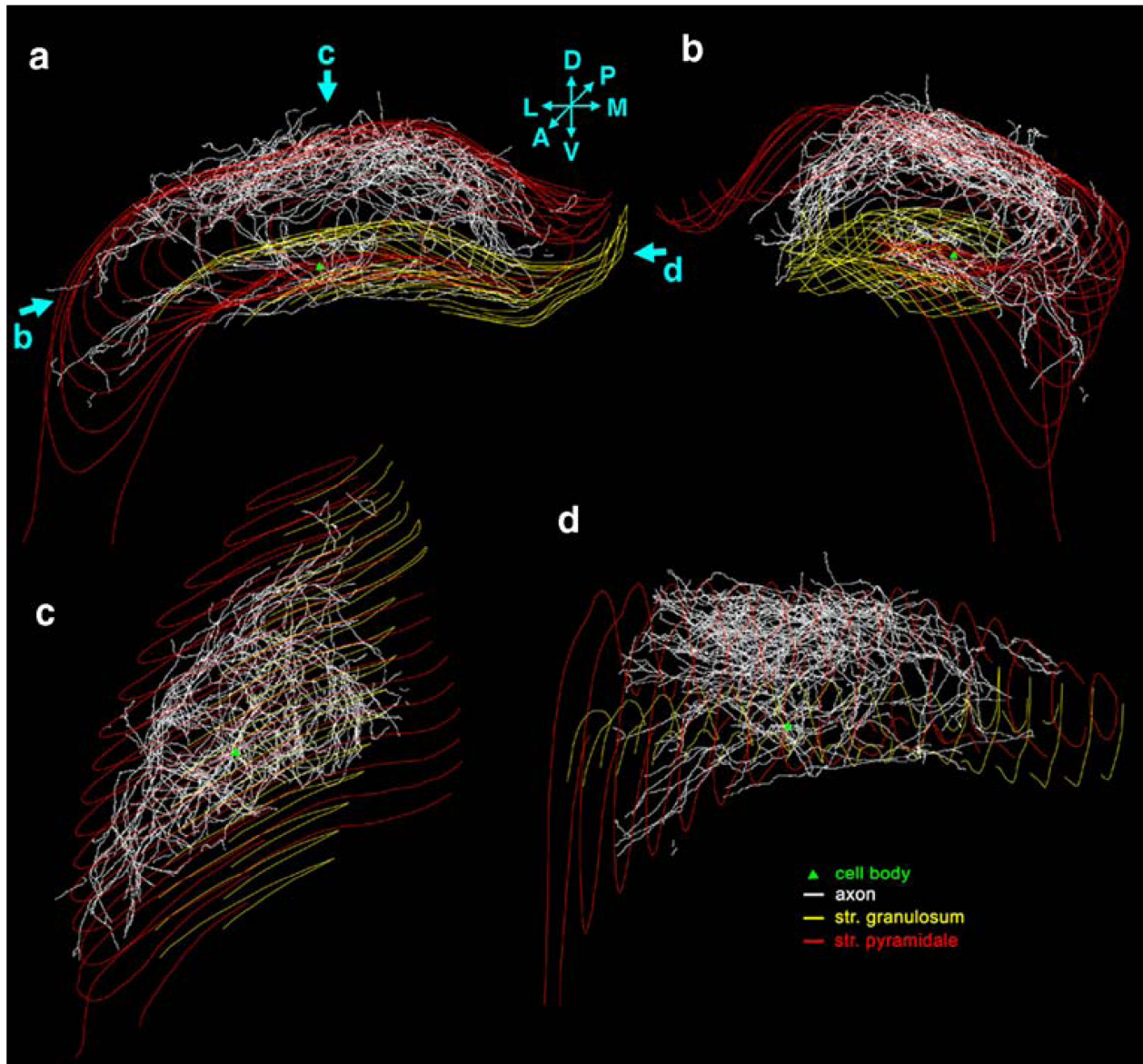


**Figure 4: NeuroLucida reconstruction of a CA3 pyramidal neuron.**

(a) Coronal view of the entire axonal arbor. The green triangle shows the location of the cell body, the axons are white, the dentate granule cell layer is marked with yellow line, CA1-3 pyramidal cell layer with red line. D dorsal, V ventral, L lateral, M medial, A anterior, P posterior. (b) This rotated view shows that CA3 pyramidal cell axon collaterals follow the curve of the Cornu Ammonis. (c) View of the axonal arbor from dorsal. (d) View from medial. (from Wittner et al., 2007)

### 2.2.2 Morphological heterogeneity of individual axons

Axon morphology is a fundamental parameter that determines its biophysical properties such as propagation of electrical signals (Hodgkin & Huxley, 1952b), likely influences biochemical diffusion and possibly active transport. The first noticeable feature of axon morphology is their calibers which greatly differ between 0.08 – 10  $\mu\text{m}$  in the CNS. Larger axons conduct APs faster and with high fidelity but are space and energy consuming. A variation in caliber which positively correlates with conduction speed was shown to be a compensatory mechanism of axon length to ensure synchronous depolarization of their synaptic targets (Salami et al, 2003; Stanford, 1987; Sugihara et al, 1993). In addition to their mean diameter, unmyelinated axons always exert irregular geometries (Greenberg et al, 1990; Shepherd & Harris, 1998) which have often been neglected in two dimensional EM morphometric analyses by representing axons as straight cylinders.

As the presynaptic compartment is a large regulatory machinery of neurotransmitter release, it requires space and makes the axon a varicose structure. In the neocortex, presynaptic boutons can be classified in two morphologically distinct categories, terminaux boutons and en passant boutons. Terminaux boutons resemble dendritic spines with a head containing the release machinery and a neck that links the head to the axon trunk. En passant boutons are presynaptic elements that are displayed in a “beads-on-string” fashion along the axon segment. Whereas layer 2, 3, 5 axons mostly exhibit en passant boutons, layer 6 axons display a high content of the terminal form (Figure 5). Interestingly, long term in vivo imaging revealed that terminaux boutons of layer 6 were more dynamic (De Paola et al, 2006) whereby neck length adjustment allows for more potential synaptic partners (Chklovskii et al, 2004; Stepanyants et al, 2002). The frequency of presynaptic boutons on an axon is also a cell specific feature that depends on the number and location of the synaptic

partners. For instance, en passant boutons are on average spaced every  $3\mu\text{m}$  along CA3 axons and also greatly vary in size ranging from  $0.011\text{-}0.572\mu\text{m}^3$  (Shepherd & Harris, 1998).

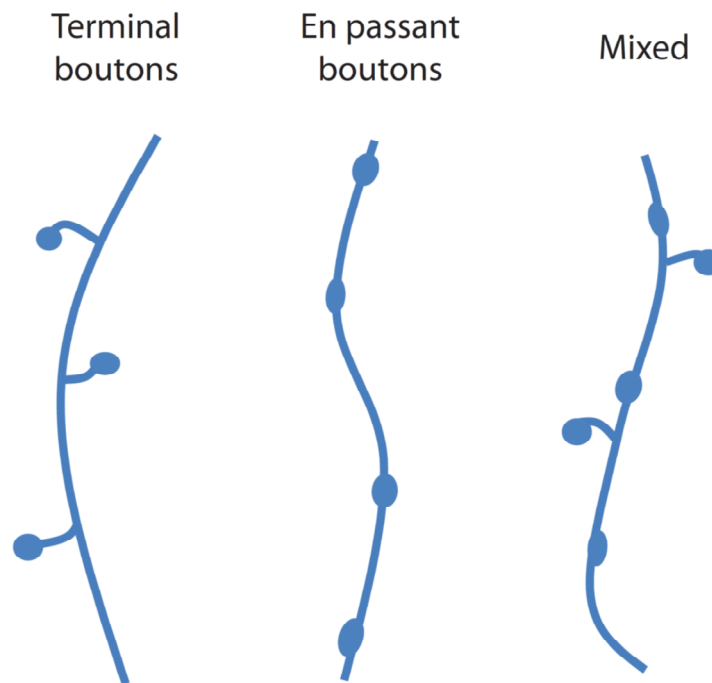


**Figure 5: Morphology of boutons in the neocortex.**

*The 2 types of boutons that can be observed in the neocortex are the terminaux boutons and en passant boutons, which are cell-type specific. Layer 2, 3, 5 axons preferentially exhibit en passant boutons whereas layer 6 axons exhibit more terminaux boutons.*

The irregularity of the axon shaft, the segment between two presynaptic elements, is often under-appreciated due to the lack of resolution in conventional light microscopy. For example, the cross section diameter of the axon shaft of CA3 pyramidal neurons can substantially vary from 80 to 300 nm within a few microns distance (Shepherd & Harris, 1998) (Figure 6). The presences of organelles, such as mitochondria or synaptic vesicles often larger than 40nm contribute to its irregular shape.

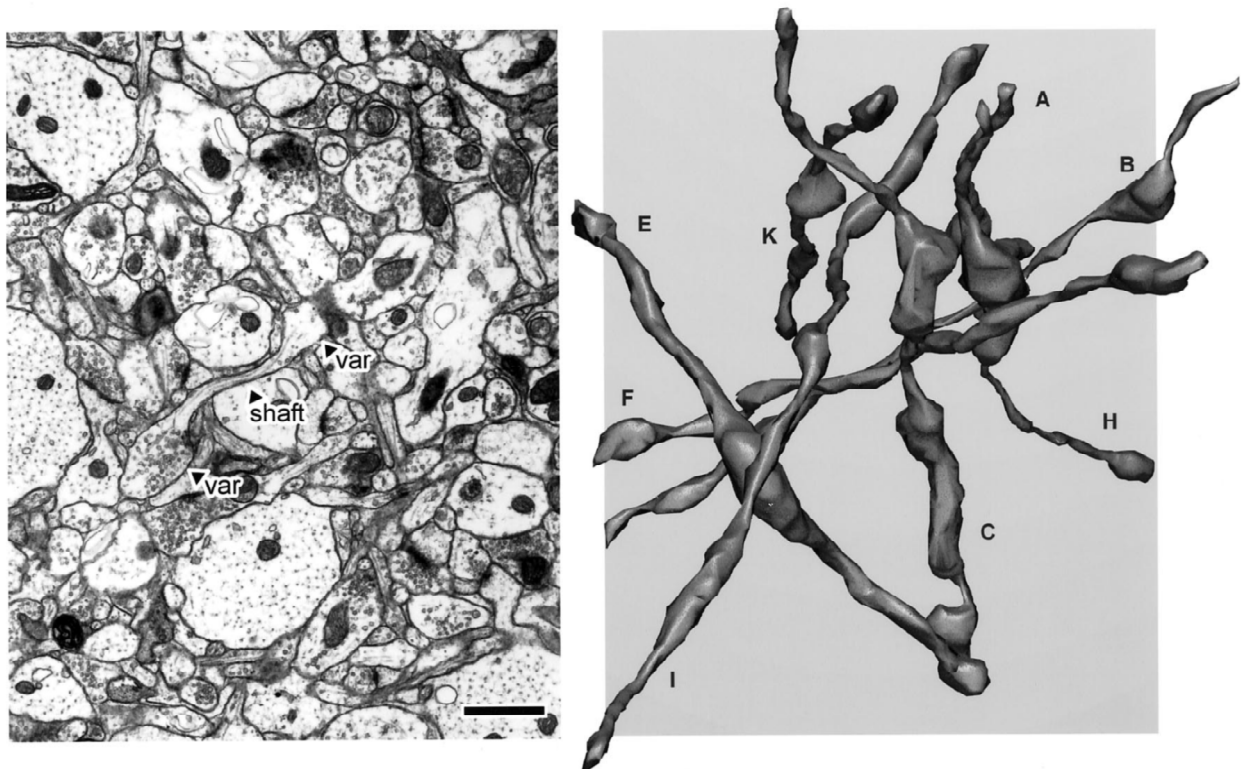


**Figure 6: Electron micrograph and 3D reconstruction of CA3 axons.**

*Left, Full-field view of a representative micrograph from the stack of images used for three-dimensional reconstructions. The shaft and two varicosities (var) of an axon are indicated. Right, Eight reconstructed axons from serial sections, at the same scale as the micrograph. Some axons extend beyond the area of the micrograph because of the three-dimensional perspective. The axons travel in many different directions, rather than parallel to each other. Scale bar, 1.0  $\mu\text{m}$ . (from Shepherd and Harris, 1998).*

## 3 Conduction of action potentials

### 3.1 Biophysical properties of axons

#### 3.1.1 Cable theory

In mathematical neuroscience, the cable theory can be used to describe how an electrical impulse is passively propagating along the axon. It consists of partial differential equations directly derived from the work of William Thomson (later known as Lord Kelvin) in the 1850s that developed the theory to describe the signal decay in submarine telegraphic cables.

The membrane properties of the axon can be defined by the membrane resistance,  $r_m$ , and capacitance,  $c_m$ , both expressed per membrane length unit ( $\Omega \cdot m$  and  $F/m$ ). Both parameters depend on the specific membrane resistance ( $R_m$ ), capacitance ( $C_m$ ) and the circumference of the axon (of radius  $a$ ) following the equations:

$$r_m = \frac{R_m}{2\pi a} \quad (1)$$

$$c_m = C_m 2\pi a \quad (2)$$

The axoplasmic resistance (or axial resistance) affects the travel rate of APs down the axon. The amount of molecules that are not electrically conductive is responsible for this resistance. As a consequence, this will cause more ions to flow across the axolemma than laterally through the axoplasm. The axoplasmic resistance ( $r_i$ ) is defined by the specific axoplasmic resistance ( $R_i$ ), and the cross section area (of radius  $a$ ) of the axon following the equation:

$$r_i = \frac{R_i}{\pi a^2} \quad (3)$$

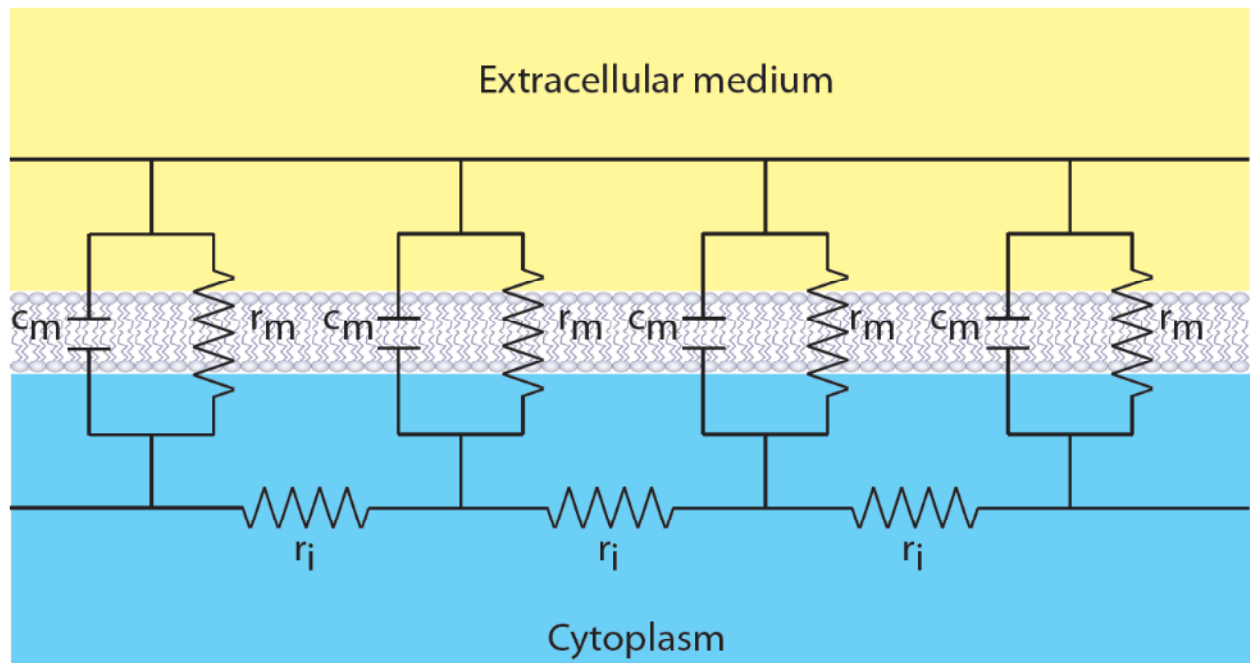


**Figure 7: Electrical model of a passive axonal cable.**

The model is composed of parallel segments of capacitances  $c_m$  and resistance  $r_m$ . The resistance in series along the fiber  $r_i$  characterize the intracellular movement of electric charges.

The length constant,  $\lambda$ , defines the distance for which a graded electric potential passively travels along the axon (Figure 7). In other words, this represents the axonal distance whereby a passive spread of potential can depolarize the membrane to threshold. Interestingly, a large length constant can contribute to spatial summation in the axon. It depends on the membrane resistance ( $r_m$ ), the axoplasmic resistance ( $r_i$ ) and the extracellular resistance ( $r_o$ ) following the equation:

$$\lambda = \sqrt{\frac{r_m}{r_i + r_o}} \quad (4)$$

Knowing that the effect of the extracellular resistance is negligible in normal conditions, the equation can then be simplified as:

$$\lambda = \sqrt{\frac{r_m}{r_i}} \quad (5)$$

To understand how the length constant changes, one has to consider that the membrane resistance is a function of the number of open ion channels and that the axoplasmic resistance is inversely correlated with the axon diameter. A given voltage ( $V_{max}$ ) will decay as a function of the distance ( $x$ ) from the source following the equation:

$$V(x) = V_{max} \left(1 - e^{-\frac{x}{\lambda}}\right) \quad (6)$$

A given voltage decays therefore by approximately 37% after travelling a distance corresponding to one length constant ( $\lambda$ ).

The time constant,  $\tau$ , defines the duration for which the membrane potential of the axon changes in response to a current change in the axoplasm. It describes how much the capacitance delays full depolarization. The time constant depends on the membrane resistance and membrane capacitance following the equation:

$$\tau = r_m c_m \quad (7)$$

The following cable equation including the time and length constant then describe how an electrical current injected at the position  $x$  travels along the axon:

$$\lambda^2 \frac{\partial^2 V}{\partial x^2} = \tau \frac{\partial V}{\partial t} + V \quad (8)$$

### 3.1.2 The Hodgkin-Huxley model for active propagation

In addition to the cable theory, the Hodgkin-Huxley model describes how an AP actively propagates along an unmyelinated axon. In 1952, by impaling a squid giant axon with an electrode, Hodgkin and Huxley were the first to experimentally measure intracellular APs (Hodgkin & Huxley, 1952a). From those measurements, they could establish a conductance-based model that explains the ionic mechanisms underlying the initiation and propagation of action potentials in axons.

It integrates voltage-gated ion channels with non-linear conductance ( $g$ ) and leak ion channels with linear conductance ( $G_L$ ); the membrane capacitance ( $C_m$ ); the equilibrium potential ( $E$ ) for sodium, potassium and leak;  $m$ ,  $n$  and  $h$  are steady-state values for activation and inactivation:

$$I_{ext} = C_m \frac{\partial V}{\partial t} + \bar{g}_{Na} m^3 h (V - E_{Na}) + \bar{g}_K n^4 (V - E_K) + G_L (V - E_L) \quad (9)$$

This equation faithfully reproduces many well known characteristics of AP propagation such as the sodium and potassium currents during an AP, the all-or-none firing pattern of AP, the AP waveform, the refractory period and the periodic firing properties.

### 3.1.3 AP propagation including geometrical constraints (Rall model)

Cable theory and Hodgkin-Huxley model set the fundamental basis for AP propagation in a fixed axonal cylinder. However, irregularities such as changes in diameter and bifurcations can have a large impact on AP propagation. Rall has established several numerical models to understand how AP propagation is affected by those irregularities (Goldstein & Rall, 1974; Holmes & Rall, 1992; Rall, 1962). In those studies, Rall and collaborators demonstrated that for an AP approaching a step decrease in the axon diameter, both velocity and AP peak

amplitude increases while an AP approaching a step increase of axon diameter causes a decrease of velocity and peak height. Exploring the effect of tapering, they found that the velocity was proportional to the length constant when a linear change in diameter over the distance is taken in account.

As mentioned above, most axons in the mammalian brain are highly collateralized. From the hillock, an axon can give rise to many branches that can innervate different areas. In 1974, Goldstein and Rall, later followed by others, mathematically describe how an AP propagates through branch points (Goldstein & Rall, 1974; Manor et al, 1991). They defined a geometrical parameter called geometric ratio ( $GR$ ) that describes the ideal diameter ( $d$ ) relationship between mother and daughter branches:

$$GR = \frac{d^{3/2}_{daughter\ 1} + d^{3/2}_{daughter\ 2}}{d^{3/2}_{mother}} \quad (10)$$

For the case where the ratio equals 1, there is a perfect impedance matching and the AP propagates in the 2 daughter branches without alteration of waveform or velocity. When the ratio is higher than 1, the electrical load approaching the branch point is not sufficient to activate both daughter branches therefore the conduction is delayed and the waveform is transiently altered. In an extreme case, the AP could even fail to propagate, stopping at the branch point.

Although theoretically possible, it still remains unclear whether the axonal compartment uses such mechanism to filter information within its arborization. Modeling studies have suggested that action potentials could fail at branch points in an activity-dependent manner (Luscher & Shiner, 1990). Propagation failures have been reported experimentally in large invertebrate axons under specific conditions (Luscher et al, 1994; Parnas, 1972; Smith, 1980a; Smith, 1980b). In more complex arborizations (e.g., CA3 axons or basket cell axons)

such mechanism has not been reported so far. Because of their small diameter (Shepherd & Harris, 1998), those thin unmyelinated axons remained out of reach for direct electrophysiological measurements. Calcium imaging of presynaptic terminals revealed a high reliability of AP propagation through branch points in cortical pyramidal neurons (Cox et al, 2000) but those measurement were confined to the proximal part of the arbor where collaterals are the largest. New emerging techniques, like direct extracellular recording of APs (Sasaki et al, 2011; Sasaki et al, 2012b) at axons collaterals and latest improvement of voltage-sensitive dyes (Foust et al, 2010) will certainly help to provide a definitive answer.

#### **3.1.4 Axon diameter and conduction velocity**

The conduction velocity in axon is mainly dependent on membrane capacitance, membrane resistance, axial resistance and the types and density of voltage-gated ions channels (Del Castillo & Moore, 1959; Hodgkin, 1939; Hodgkin & Huxley, 1952a; Katz, 1947; Renganathan et al, 2001; Waxman & Ritchie, 1993). Therefore, the action potential velocity depends on both, passive propagation parameters and the non-linear membrane conductance that define the active propagation. As described above, the passive propagation is defined by the length and time constants of the membrane that are dependent on the membrane capacitance, resistance and axial resistance which in turn depends on the diameter. From the equations described above, large axons have large length constants and small time constants which propagate the impulses rapidly. A small time constant means that a depolarization affects more rapidly an adjacent section which brings it to threshold sooner and therefore increases the propagation velocity. For a large length constant, a potential change in a given segment spreads a greater distance along the axon and brings further distal segment to threshold sooner. The equation of the length constant can be written differently to highlight its diameter ( $d$ ) dependence:

$$\lambda = \sqrt{\frac{dR_m}{4R_i}} \quad (11)$$

The propagation velocity is directly proportional to the length constant ( $\lambda$ ) and inversely proportional to the time constant ( $\tau$ ) as illustrated by the following equations:

$$\text{Velocity} \propto \lambda/\tau \quad (12)$$

$$\text{Velocity} \propto \frac{1}{C_m} \sqrt{\frac{d}{4R_m R_i}} \quad (13)$$

Thus, for given specific membrane properties in unmyelinated axons, velocity is proportional to the square-root of the axon diameter (Dayan & Abbott, 2001; Hodgkin & Huxley, 1952a). To double the velocity in an axon, it is necessary to quadruple the diameter. It is important to mention that this relation does not hold true for myelinated axons. The coating of axons with a thick insulating sheath of myelin represents another way to decrease the membrane capacitance and therefore increasing the propagation velocity. In this case, with early empirical (Gasser & Grundfest, 1939; Hursh, 1939) and later theoretical investigations (Rushton, 1951), it is generally agreed that there is a linear relationship between the conduction velocity of myelinated axons and their diameter.

To determine the velocity of an actively propagating AP, it is possible to derive the Hodgkin and Huxley equation based on voltage-clamp data and include passive spread properties from the cable theory giving the following equation:

$$\frac{d}{4R_i} \frac{\partial^2 V}{\partial x^2} = C_m \frac{\partial V}{\partial t} + \bar{g}_{Na} m^3 h (V - E_{Na}) + \bar{g}_K n^4 (V - E_K) + G_L (V - E_L) \quad (14)$$

By numerically solving this equation, the AP propagation velocity remains proportional to the square-root of the axon diameter. The accumulation of experimental measurements has confirmed that the axon diameter is a good indicator of the propagation velocity within and across species. For examples, the squid giant axon can approach a millimeter in diameter and propagate APs at a speed range of 10-25 m/s (Rosenthal & Bezanilla, 2000). Peripheral crustacean axons display velocities of 1-10 m/s with a diameter range of 1-10  $\mu\text{m}$  (Young et al, 2006). At the other end of the spectrum, CA3 axons, which are among the smallest axons with a diameter range of 100-350 nm, the speed of AP propagation was estimated to be around 0.25-0.38 m/s (Andersen et al, 2000; Meeks & Mennerick, 2007).

### **3.2 Short-term dynamics of action potential propagation**

The various types of voltage-gated ion channels in the membrane can have substantially different voltage-dependences and time constants associated with activation and inactivation. Therefore, properties of AP propagation, such as excitability and conduction velocity can change during repetitive stimulation. The first systematic inquiry on activity-dependent changes in spike conduction using earthworm lateral giant axon and frog sciatic A-fibers revealed a change in both excitability and conduction velocity (Bullock, 1951). When the interval between the two stimuli was only several milliseconds, excitability and conduction velocity were reduced (subnormal period). Interestingly, when the interval was longer, up to 100 ms, excitability and velocity were increased. This phenomenon is referred as the supernormal period. A similar change in excitability of CA3 Schaffer collaterals was showed later by Soleng et al. by using antidromic stimulation and recording from the soma (Soleng et al, 2004). They found that the passage of a single AP initially reduces the excitability of the membrane for the first 15 ms and then increases excitability for the next 200 ms.

The shape of the presynaptic AP carries the electric load that determines the  $\text{Ca}^{2+}$  current flow in the presynaptic compartment and hence neurotransmitter release. The AP waveform has long been considered highly stereotypical and faithful when propagating along axons. However, several studies have shown that the amplitude and the duration of APs can be regulated by activity and hence modulate transmitter release (Byrne & Kandel, 1996; Shapiro et al, 1980).

Geiger and Jonas were the first to demonstrate that the duration of APs is not fixed in the hippocampus (Geiger & Jonas, 2000). By performing whole-cell recording of mossy fiber boutons from granule cells in the dentate gyrus, they found that APs get broader during repetitive stimulation. Kv channels, responsible for the AP broadening, rapidly inactivate during high frequency stimulation and slowly recover from inactivation. In addition, they measured the subsequent increase of presynaptic  $\text{Ca}^{2+}$  inflow.

Performing extracellular recording on CA3 axons, Sasaki et al. demonstrated that the AP waveform broadens locally in response to local application of glutamate and adenosine  $A_1$  receptor antagonist on the axon shaft (Sasaki et al, 2011). The authors demonstrated that axonal AMPA receptors activation causes a local depolarization that broadens APs while traveling down the axon. As a consequence of large APs, they showed that synaptic transmission is enhanced. In addition, they provided evidence that astrocytes, known to play an important role in local synaptic transmission, could regulate peri-axonal glutamate concentration and be responsible for the local broadening of APs in the distal part of the axon.

Later, using a similar approach, Sasaki et al. demonstrated that network activity, responsible for sustained depolarization of the resting membrane potential in the soma, does broaden APs in the proximal part of CA3 axons (Sasaki et al, 2012a). They could show that somatic depolarization of CA3 pyramidal cells facilitates neighboring CA3 to CA3 but not distal CA3

to CA1 synaptic transmission. Moreover, they illustrated the importance of the axonal topology showing that AP broadening decays with the distance from the soma and the branching pattern.

## **4 Long-term plasticity of unmyelinated axons**

### **4.1 Presynaptic changes associated with synaptic plasticity**

#### **4.1.1 Synaptic plasticity**

Learning and memory refers to the ability of the brain to encode, store and retrieve information. This ability relies on the plastic nature of neural networks, allowing the brain to adapt itself in response to experience. Among these adaptations, synaptic strength enduring patterns of activity can be modulated in a phenomenon known as synaptic plasticity. The concept was first introduced by Donald Hebb more than 60 years ago: ‘When an axon of cell A is near enough to excite cell B and repeatedly or persistently takes part in firing it, some growth process or metabolic changes takes place in one or both cells such that A’s efficiency, as one of the cells firing B, is increased’ (Hebb 1949). However, it took more than 20 years to get the first experimental evidence of synaptic plasticity. In 1973, by stimulating the perforant path and recording field potentials in the dentate gyrus in anesthetized rabbits, Bliss and Lømo discovered that strong synaptic activity can result in a persistent increase of synaptic strength, a phenomenon referred as long-term potentiation (LTP) (Bliss & Lomo, 1973). The functional counterpart of LTP that is an activity-dependent and input specific decrease of synaptic strength, known as long-term depression (LTD), was experimentally demonstrated a few years later (Lynch et al, 1977).

Since then, LTP and LTD are the most extensively studied paradigms of plasticity and were shown to occur in most synapses of the brain (Cooke & Bliss, 2006). To date, LTP and LTD are believed to be important cellular correlates of learning and memory.

Over the past 40 years, much attention was focused on understanding the structural and functional changes occurring at the post-synaptic compartment. Many forms of synaptic

plasticity have been described involving several biochemical pathways. The most stereotypical form of LTP and LTD occurs at the Schaffer collaterals-CA1 synapse and depends on the activation of postsynaptic NMDA receptors. Typically, expression of LTP and LTD can be decomposed in an early and a late phase. During LTP, NMDA receptors activation produces a rapid and high increase of  $\text{Ca}^{2+}$  in the post-synapse that leads to the phosphorylation of CaM-kinase II. In the early phase, AMPA receptors sensitivity increases usually producing a large potentiation of the synapse. Later, the increase of the global phosphorylation rate in the post-synaptic compartment leads to a long lasting recruitment of AMPA receptors to the synaptic membrane increasing the synaptic efficacy (Lisman, 1989). On the other hand, LTD is induced by a moderate and prolonged increase of  $\text{Ca}^{2+}$  concentration that leads to the activation of calcineurin. The phosphatase activity of calcineurin reduces the synaptic weight by decreasing the number of AMPA receptors at the synapse.

Many structural correlates have been established to underlie the expression of synaptic plasticity. The recruitment of receptors to the postsynaptic density that is responsible for the synaptic strengthening during LTP is often correlated with an increase in spine volume (Harvey & Svoboda, 2007; Kopec et al, 2006; Matsuzaki et al, 2004; Yang et al, 2008). Similarly, LTD causes spine shrinkage (Zhou et al, 2004). Although, it is often assumed that the presynaptic compartment also undergoes structural and morphological changes reflecting structural modifications during synaptic plasticity, there is surprisingly no clear evidence in the literature. It is possible however that significant functional changes occurring at presynaptic boutons might be reflected in much more subtle structural and morphological modifications compared to what spines experience.

#### **4.1.2 Functional and structural modifications of the presynaptic compartment during synaptic plasticity**

The involvement of the presynaptic compartment in the change of synaptic strength has been debated for long. Some argue for a dominant role of the postsynaptic compartment (Bredt & Nicoll, 2003; Malenka & Bear, 2004; Malenka & Nicoll, 1999; Malinow & Malenka, 2002; Song & Huganir, 2002), while others indicate that the presynaptic sites also contribute to the increase in synaptic strength (Bolshakov & Siegelbaum, 1995; Choi et al, 2000; Emptage et al, 2003; Malinow, 1991; Stevens & Wang, 1994; Stricker et al, 1999; Voronin et al, 2004).

In the series of events occurring during the classical NMDAR-dependent LTP, the strengthening of the synapse is not homogenous across the pre and postsynaptic compartments. These processes include a rapidly developing postsynaptic component and a slowly developing presynaptic component (Lisman & Raghavachari, 2006). By monitoring the level of neurotransmitter release together with synaptic activity at CA3-CA1 synapses, Bayazitov et al. explored the differential contribution of the pre and postsynaptic compartment during the strengthening of synapses (Bayazitov et al, 2007). The induction of LTP was performed by different stimulation protocols. They found that 50 Hz and short theta-burst stimulation (TBS) favors postsynaptic strengthening while 200 Hz and TBS promotes a compound LTP that is expressed both pre- and postsynaptically. In this compound LTP expression, the postsynaptic component is fast and strongly dependent on the activation of NMDA receptors whereas the presynaptic component is slower and requires the activation of L-type Cav channels (Grover & Teyler, 1990; Zakharenko et al, 2001) and depends on protein kinase A (PKA) activation (Castillo, 2012) (Figure 8). Other investigations showed that R-type Cav channels are involved in the presynaptic component of LTP in the mossy fiber CA3 pathway (Breustedt et al, 2003; Dietrich et al, 2003). Along with the increase in release probability following the induction of LTP, Bourne et al. have shown that

ultrastructural modifications occur in the presynaptic compartment (Bourne et al, 2013). Performing 3D reconstructions of axons from serial section electron microscopy 30 minutes and 2 hours after induction of LTP, they observed a persistent reduction of the vesicle pool of around 30% and a transient decrease in the readily releasable pool.

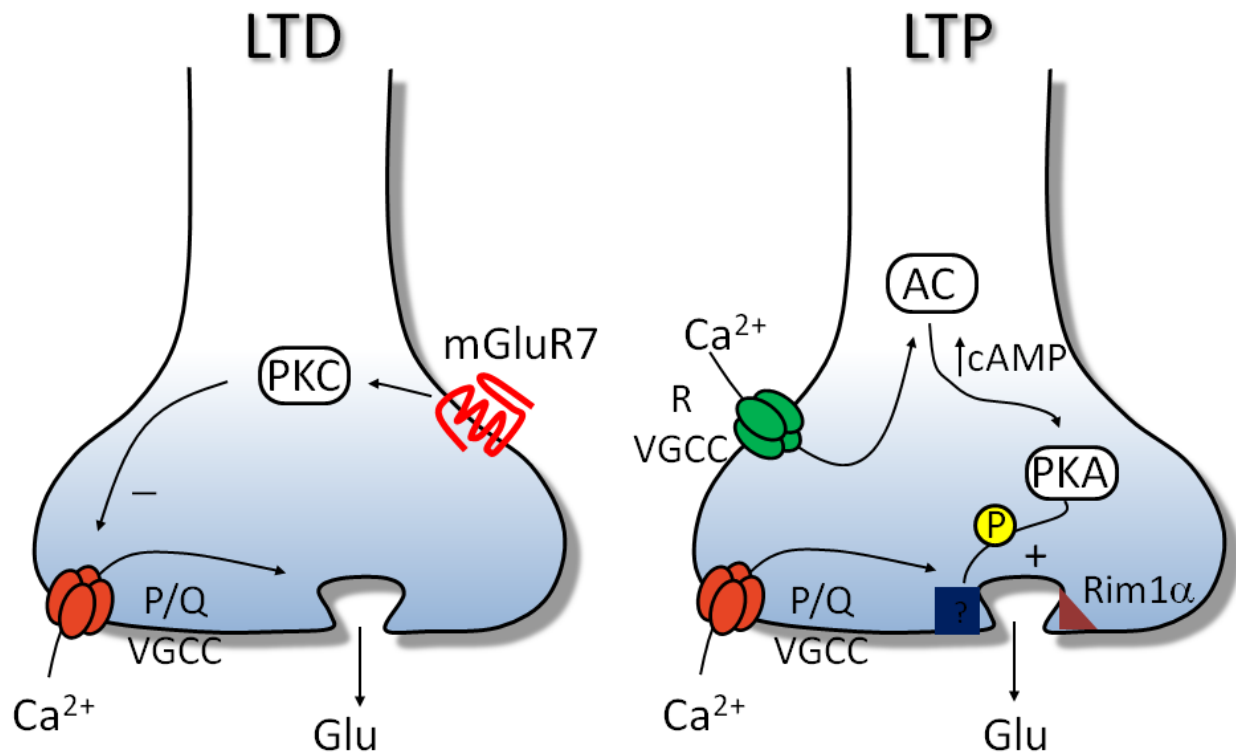


**Figure 8: Expression mechanism of presynaptic LTP and LTD: prototypical mechanisms.**

*Voltage-gated calcium channel mediated  $Ca^{2+}$  influx responsible for neurotransmitter release is involved in some forms of presynaptic LTP/LTD. The activation of mGluR7 produces a depression of P/Q types Cav channels via the activation of the PKC pathway hence reducing neurotransmitter release during LTD. During LTP, R type Cav channels are thought to activate the PKA pathway facilitating neurotransmitter vesicle fusion. (adapted from Castillo, 2012)*

LTD induction has been shown to be associated with a long-lasting depression of the presynaptic  $Ca^{2+}$  transients at mossy-fiber stratum lucidum interneuron synapses (Pelkey et al, 2006). The activation of mGluR7 produces irreversible depression of P/Q type Cav

channels that could possibly involve the protein kinase C (Figure 8) (Perroy et al, 2000). Interestingly, major structural rearrangements accompany the induction of LTD. By combining electrophysiology with timelapse two-photon imaging and monitoring the activity and synaptic morphology, Becker et al. and Bastrikova et al. discovered that the turnover of presynaptic boutons significantly increase after LTD induction in addition to synapse elimination (Bastrikova et al, 2008; Becker et al, 2008).

## **4.2 Activity-dependent plasticity of intrinsic excitability**

The plasticity of intrinsic excitability is a type of non-synaptic plasticity whereby the threshold voltage for the initiation of APs is regulated upon activity. A change in postsynaptic excitability was already suggested in the early descriptions of LTP at hippocampal synapses (Bliss & Lomo, 1973) and it is now well established that changes in pre- and postsynaptic intrinsic excitability plays an important role in synaptic plasticity (Campanac & Debanne, 2007; Debanne et al, 2003; Debanne & Poo, 2010; Zhang & Linden, 2003). As the excitability of the cell membrane depends on the ionic environment and the channel composition, it is becoming increasingly clear that every sub-cellular compartment can differentially regulate their own excitability. This is certainly true for dendrites, where an increase of local excitability has been measured following the induction of LTP (Campanac et al, 2008; Frick et al, 2004). Concerning the axonal compartment, there are only a few reports indicating a change in excitability associated with synaptic plasticity. Xu et al. have demonstrated a synergic effect between the induction of synaptic LTP in CA1 pyramidal cells and an increase in the sensitivity of Nav channels for more hyperpolarized potentials in the presynaptic cell (Xu et al, 2005). Interestingly, this presynaptic change in excitability was blocked by NMDA receptor antagonist APV, Ca<sup>2+</sup> chelators, CaM kinase inhibitors and protein synthesis inhibitors. This indicates that the change of excitability shares common

mechanisms with the late phase of synaptic LTP. However, since the presynaptic effects were recorded at the soma, it remains unclear whether the locus of expression of this change in excitability is in the axonal trunk or in the AIS. Earlier, a similar concomitant change of synaptic strength and presynaptic excitability was found in cultured hippocampal neurons (Ganguly et al, 2000). The authors could prevent the increase of intrinsic excitability by inhibiting a retrograde signaling pathway involving presynaptic PKC. This would suggest that the change in excitability occurs near the presynaptic compartment, hence the axonal trunk.

The AIS is a key structure that controls the overall excitability of neurons. In 2010, two groups have reported novel mechanisms of activity-dependent change in neuronal excitability involving structural modifications of the AIS.

By labeling and imaging the AIS in dissociated hippocampal neurons, Grubb and Burrone showed that neurons can regulate the position of the entire AIS compartment according to ongoing activity (Grubb & Burrone, 2010). The AIS moves away from the soma in response to a persistent increase of extracellular potassium. Performing current-clamp recording combined with AIS imaging, they demonstrated that the AIS relocation is associated with a decrease in neuronal excitability. In another study, Kuba et al. demonstrate that deprivation of auditory input in avian brainstem auditory neuron also leads to structural changes of the AIS (Kuba et al, 2010). Interestingly, unlike the relocation of the AIS described by Grubb and Burrone, using similar labeling techniques, they found that the auditory deprivation increases the length of the AIS but not the distance from the soma. Similarly, they correlated the increase in AIS length with an increase of neuronal excitability via patch-clamp recordings.

### **4.3 Long-term change of action potential conduction velocity**

As described above, the conduction velocity in axons is mainly defined by two parameters: 1) the morphology by considering the core diameter of the axon and its irregularities and 2) the excitability of the axon membrane defined by types and numbers of ion channels. Because of their low optical and electrophysiological accessibility, so far, no study has shown an activity-dependent correlative change between the biophysical properties and conduction velocity.

Although there are few evidences demonstrating that axonal conduction delay can be a plastic feature. Variations in conduction delay were measured by electrophysiological recordings in rabbit visual corticotectal and callosum axons in vivo (Swadlow, 1982; Swadlow, 1985). Indeed, for some of the recorded axons, delays were continuously increasing or decreasing over several months period. By culturing cortical neurons on a multi-electrode array (MEA), Bakkum et al. could to induce, detect and track changes of a small neuronal network and measure how they adapt to various patterns of stimulation. Using this approach, they demonstrated that along with changes in synaptic efficacy, APs propagation delays and amplitude were modulated (Bakkum et al, 2008). Performing repeated stimulation patterns (0.5 Hz) at various location of the reduced network, they observed that, in some axons, the conduction velocity and the amplitude of APs were modulated. The absence of correlation between AP amplitude and velocity may indicate changes in the morphology in addition to channel densities.

However, there are numerous reports on both, structural modifications (Bastrikova et al, 2008; Becker et al, 2008; De Paola et al, 2006) and excitability changes (Bi & Poo, 2001; Ganguly et al, 2000; McNaughton et al, 1994) in axons; those were always the result of local measurements or from reduced preparation. For this reason, people could not reliably assess conduction velocity measurements on such short axonal distance.

## 5 STED microscopy

### 5.1 Basic optical principle of STED microscopy

Fluorescence microscopy is one of the most widely used and powerful techniques in the life sciences, enabling the visualization of cell-biological structures and processes with extremely high specificity and sensitivity in living tissue samples. Fluorescence is the phenomenon whereby a fluorophore absorbs a photon (i.e., 488 nm for GFP) and produces the emission of another photon of lower energy (525 nm) defined by the Stoke shift. Interestingly, when the molecule is in the excited state, it can directly be de-excited by a photon that matches the energy difference between the excited state and the ground state (595 nm for GFP). Upon interaction of the photon with the excited fluorophore, the molecule returns to the ground state before spontaneous fluorescence emission can occur in a process called stimulated emission (Figure 9).

Stimulated emission depletion (STED) microscopy is an imaging technique that uses these non-linear properties of fluorophores described above to achieve super resolution. It was invented by Stefan W. Hell who first described its principle in 1994 (Hell & Wichmann, 1994), and demonstrated it experimentally in 1999 (Klar & Hell, 1999). In neuroscience, STED microscopy enables the observation of nanoscale dynamics of the finest structures of neurons and glia previously inaccessible with traditional light microscopy techniques.

In conventional light scanning microscopy like confocal or two-photon microscopy, the resolution of the optical system is limited by the diffraction of light. This means that when light is focused through a lens or objective, a pattern of diffraction is formed, called point spread function (PSF), and defines the volume of excitation of the fluorophores for a given position in the focal plane. The size of the PSF depends on the excitation wavelength and the numerical aperture ( $NA$ ) of the objective. From this, it is then possible to determine the

theoretical resolution limit ( $\Delta r$ ) of the system given by Abbe's formula with  $\lambda$ , the wavelength used to excite the fluorophore and NA, numerical aperture of the objective.

$$\Delta r \cong \frac{\lambda}{2 NA} \quad (15)$$

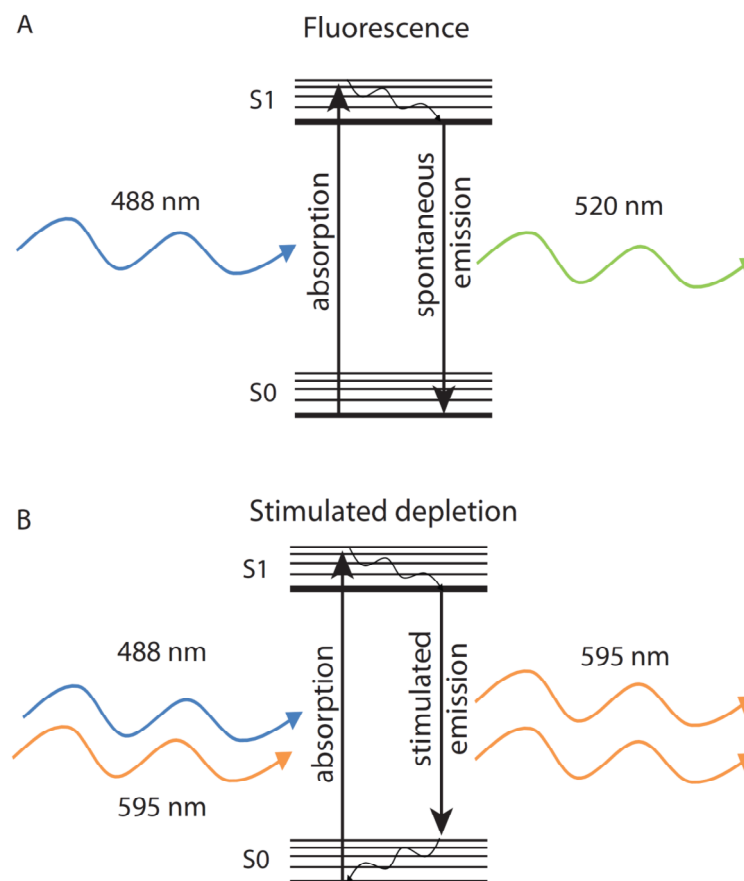


**Figure 9: Simplified Jablonski diagram of GFP for fluorescence and stimulated depletion.**

(A) The GFP molecule is excited from its ground state ( $S_0$ ) to a higher energy level (mostly  $S_1$ ) by a blue photon (488 nm). After vibrational relaxation to the lowest  $S_1$  level, the molecule emits a red-shifted photon (green) and returns back to its ground state by a process called fluorescence.

(B) In case of stimulated depletion, similarly, the GFP molecule is excited from its ground state ( $S_0$ ) to a higher energy level ( $S_1$ ) by a blue photon (488 nm). Before spontaneous fluorescence occurs, a red-shifted photon (595 nm) de-excites the molecule from ( $S_1$ ) to its ground state ( $S_0$ ) which leads to the emission of a photon has the same properties (such as wavelength, polarity) as the incident photon.

STED microscopy circumvents the diffraction limit of light by spatially controlling the excited states of fluorescent molecules.

This is achieved by 1) taking advantage of stimulated emission, a process that competes with spontaneous fluorescence, efficiently preventing the fluorophores from emitting fluorescent signals and 2) by spatially controlling the fluorescence quenching which restricts the fluorescence signal to be emitted in the center of the excitation PSF.

### **5.1.1 PSF engineering**

The second requirement to achieve super-resolution imaging using stimulated depletion is the ability to shape the PSF of the depletion beam at the focal plane in order to allow the excited molecule to emit exclusively in the center of the excitation PSF. This is achieved by the use of a helical vortex phase plate that allows the Gaussian STED beam to destructively interfere in the center so that a vortex of light is created. When an optical vortex travels through a focusing lens or an objective and is projected onto a flat surface, its intensity distribution will form a doughnut-like pattern in the focal plane (Figure 10). That way, the azimuthally distributed photons of the doughnut will quench the fluorescence at the rim of the excitation PSF. It is critical to the performance of a STED microscope that the center of the doughnut remains at a minimal value throughout the power range. For this reason, a  $\lambda/4$  wave plate is used to create circular polarization of the STED light in the focal plane.

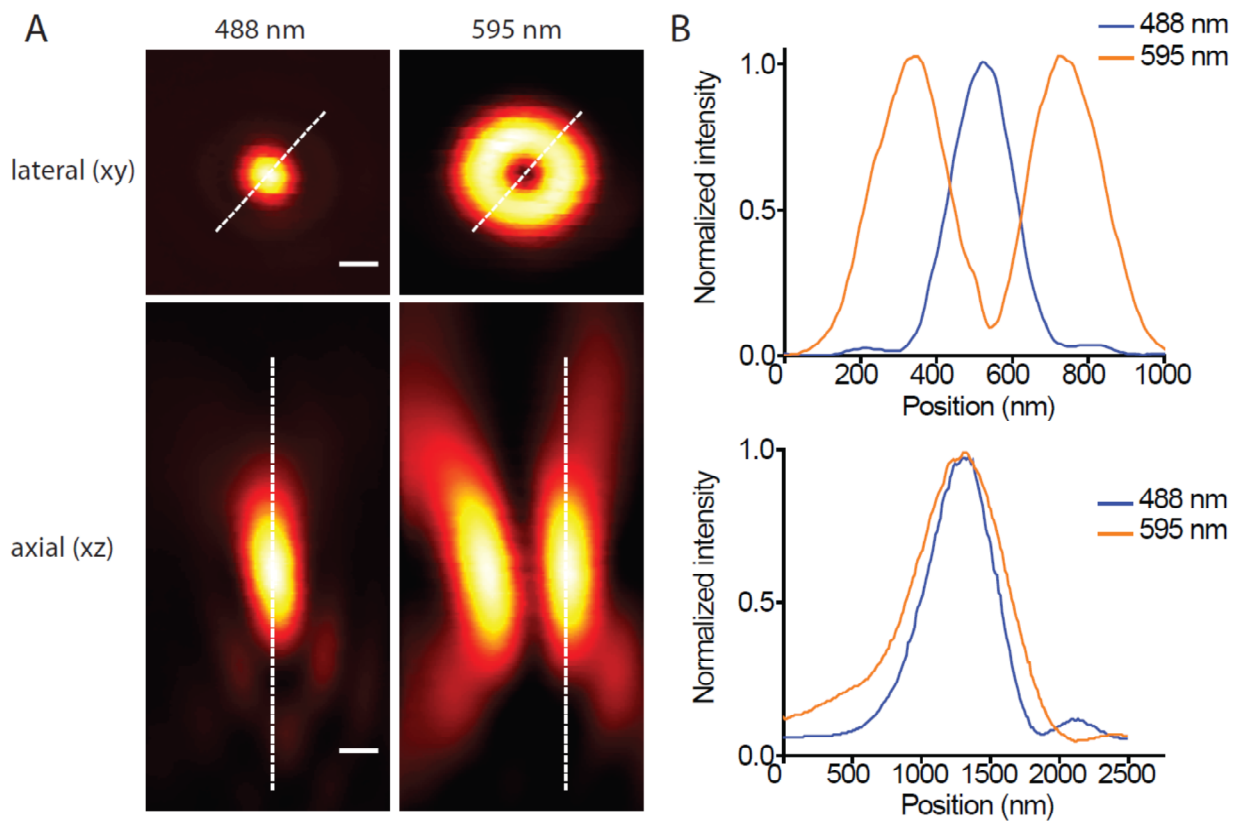


**Figure 10: Point spread function engineering for STED microscopy.**

(A) Reflections of the laser beams from gold particles used for visualization and spatial alignment of the excitation and STED beams. The laser beams are routed through a pellicle beam splitter so that the reflections can be detected by a photomultiplier tube. This allows for the characterization of the excitation and STED beams and illustrates the doughnut-like intensity distribution of the STED laser. Scale bar: 200 nm.

(B) Intensity profiles along the optical axis of the excitation and STED PSF shown in (A), indicated by the white dashed line.

### 5.1.2 Improvement in spatial resolution

For STED microscopy, in addition to the excitation wavelength and the NA, the optical resolution will also be defined by the intensity of depletion saturation of the fluorophore image. The fluorescent photon yield of a molecule does not increase linearly with the excitation intensity. This non-linear process also exists for stimulated depletion and is

responsible for the theoretically unlimited resolution. Indeed, using high intensity doughnut-like depletion beam allows the saturation of the quenching process around the excitation PSF. As a result, the fluorescence is allowed to be emitted only from the center of the doughnut, giving an effective PSF below the diffraction limit of the optical system.

STED microscopy was the first technique that was not limited by the diffraction barrier of optical microscopy. The resolution in STED imaging is theoretically unlimited and can be expressed by a modified Abbe's equation where  $I$  is the STED beam intensity used and  $I_s$  is the STED beam intensity required to reduce the fluorescence by a factor of  $1/e$  (Harke et al, 2008):

$$\Delta r \cong \frac{\lambda}{2 \cdot NA \sqrt{1 + I/I_s}} \quad (16)$$

In theory, STED microscopy could provide an unlimited resolution. This implies that the power used for depletion is infinite. In practice, there are technical limitations such as the property of lasers which deliver a finite amount of light power. To date, the record for the best resolution in STED goes to Rittweger et al. where in 2009, by using nitrogen vacancies diamond and an average of 850 mW STED power, they achieved to obtain a resolution of  $\sim 5.8$  nm (Figure 11) (Rittweger et al, 2009). In this case, the power remains a limiting factor to improve even more the resolution.

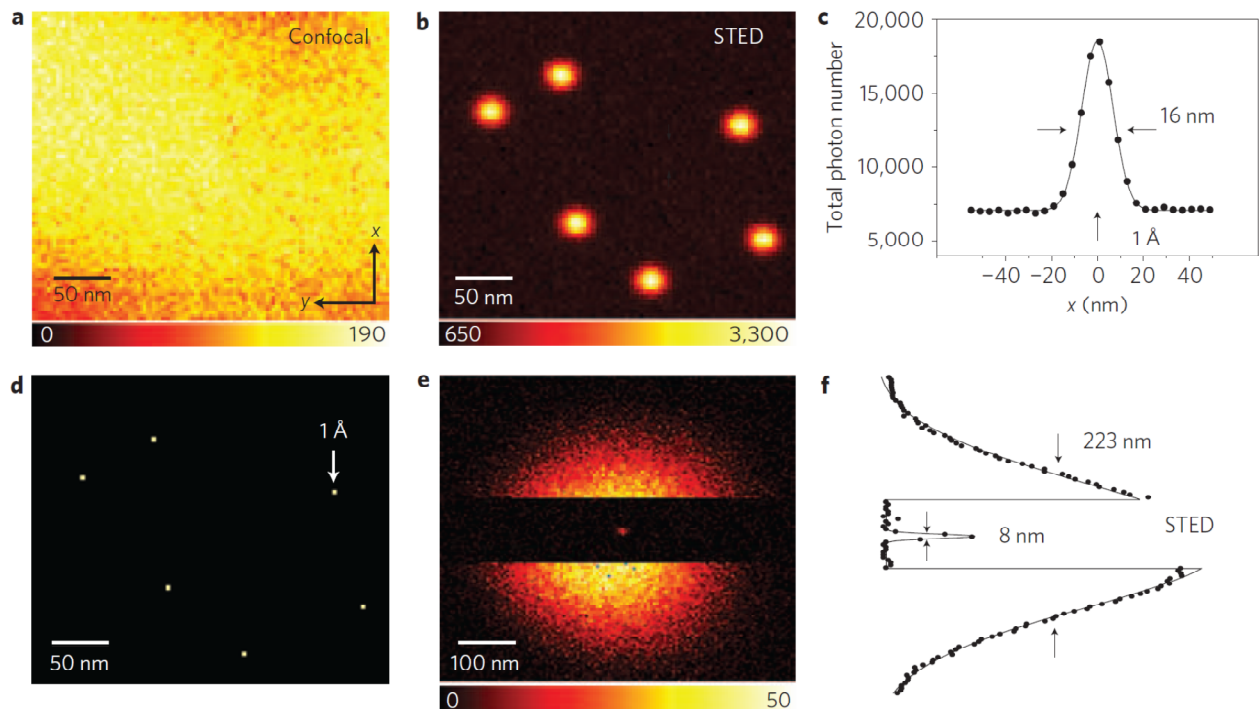


**Figure 11: Stimulated emission depletion microscopy reveals densely packed nitrogen-vacancy centres in diamond.**

*Confocal (a) and STED (b) images from the same crystal region. (c) The individual centers resolved in b automatically yield the effective PSF of the STED recording whose y-profile exhibits a FWHM of  $\Delta y = 16.0$  nm. (d) The coordinate of each centre can be calculated with 0.14 nm precision. Comparing (a) with (d) highlights the dramatic gain in spatial resolution resulting from the unique increase in resolution. (e,f) Applying  $I_{\max\text{STED}} = 3.7$  GW cm<sup>-2</sup> shrinks a confocal spot of 223 nm diameter (FWHM) down to 8 nm. Note that the increase in resolution is a purely physical phenomenon. (from Rittweger et al., 2009)*

## 5.2 Development of STED imaging in living tissue

To perform STED imaging on live cells, the high light power can damage the integrity of the structure. The photo-damage is a consequence of light absorption by the biological tissue and hence produces heat. Therefore it is necessary to use modest amounts of light without compromising resolution. By using pulsed lasers, it is possible to image with low average STED power to preserve the sample and high peak intensity to obtain super resolution. This

requires that both excitation and depletion pulses are synchronized and differentially delayed. Several studies have demonstrated that STED imaging is compatible with live-cell observations achieving a spatial resolution of around 60-100 nm with STED intensities comparable to what is being used for two-photon imaging (Nagerl et al, 2008; Rankin et al, 2011; Willig & Nagerl, 2012).

### **5.3 STED imaging of the dynamics of axon morphology**

Unmyelinated axons in the hippocampus are often too small to be properly resolved by conventional light microscopy (Shepherd & Harris, 1998). STED microscopy allows the observation of nanoscale features and permits quantitative morphological analysis of the axonal structure by extracting precise estimates of axon diameters. To understand how to perform measurements based on collected signal intensity, it is important to discriminate the evaluation of the performance of the optical system and the measurement of a biological structure.

The home-built STED microscope in the laboratory uses an excitation wavelength at 485 nm and a 1.4 NA objective. Applying Abbe's formula, the theoretical resolution limit in confocal mode of the system is then 173 nm. The experimental validation of the instrument's resolution should be tested by using, for example, fluorescent nanobeads that are significantly smaller than the theoretical resolution of the system and can be approximated as point sources of light. In confocal imaging, the PSF at the focal point follows a 2D-Gaussian distribution in the lateral (xy) dimension. The distribution of the fluorescent signal must then be mathematically approximated as a 2D-Gaussian distribution and therefore the full width at half-maximum (FWHM) from the Gaussian fit gives the best approximation on the resolution

of the system. If the measured FWHM value matches the theoretical resolution, the system is fully optimized and can be regarded as being truly diffraction limited.

The calculation of the theoretical resolution in STED imaging implies to have a good understanding of the photo-physical properties of the fluorophores which are likely to change depending on their environment (temperature, pH, medium). It is therefore easier to test experimentally the resolution using fluorescent beads. In STED microscopy, the resulting effective PSF at the focal plane is the result of the combination of the excitation beam and a doughnut shape depletion beam. In condition of saturated depletion of the fluorophore, the effective PSF is then following and well approximated by a Lorentzian distribution. By imaging 40 nm fluorescent beads in STED mode, the FWHM measurement that reflects the performance of the system can be around 40 nm when the system is optimized; therefore the size of the bead becomes a limiting factor to assess the resolution. For the experiments, we typically consider 40 nm as our resolution limit for STED imaging which is well below the size of the thinnest axons measured in electron microscopy (~ 80 nm) (Shepherd & Harris, 1998).

The improvement of resolution provided by STED microscopy enables to study the structural complexity of axon. In order to assess the diameter of axons, we measure the FWHM of the fluorescence intensity profile from the axon section area. The FWHM represents the extend of the intensity distribution and therefore is directly linked to the axon diameter. In opposition to the resolution of an optical system that purely depends on the size of the PSF, the measurement of a fluorescent structure is considered to be much larger than the resolution limit. In that case, no assumption can be made on the fluorescence distribution of a volume labeled axon. Therefore, the FWHM is directly extracted from the raw intensity profile and reflects the best estimate of the true size of the structure.

## 6 Aims of the study

In contrast to the somato-dendritic region, much less is known about if and how axonal compartment is dynamically regulated. Axons are classically viewed as static transmission cables that reliably transmit APs over long distances. However, recent studies have questioned this view, indicating that they are structurally and functionally dynamic.

Given that geometrical features shape the passive electrical properties of axons and hence should influence AP propagation, we wanted to explore the possibility that axons undergo dynamic modifications in their morphology in response to electrical stimulation. However, because axon morphology cannot be fully resolved in live tissue, little is known about their structural dynamics, let alone what its impact is for axon function. I overcame this technical limitation by using superresolution STED microscopy, allowing me to investigate the structure and function of CA3 axons in living hippocampal slices.

The central aims of my PhD thesis were the following:

- 1) To establish STED microscopy for imaging axon morphology in living brain slices in parallel with electrophysiological analyses.
- 2) To develop semi-automated image analysis tools for rapid and reliable quantification of axon morphology imaged by STED microscopy.
- 3) To examine the morphological dynamics CA3 axons by by time lapse imaging under control conditions.
- 4) To investigate activity-dependent structural changes in presynaptic boutons and axon shafts axons using common plasticity paradigms like LTP and LTD.
- 5) To evaluate the functional impact of the morphological changes on AP propagation using electrophysiological recordings and computer simulations.

## MATERIALS AND METHODS

### Animals

Wild-type mice were kept under 12 h light/ 12 h dark cycle with *ad libitum* access to food and water (strain from Jackson Labs, Bar Harbor, ME). All experiments were in accordance with the National Code of Ethics on Animal Experimentation (Carte Nationale d'éthique sur l'expérimentation animale; Ministère de l'enseignement supérieur et de la recherche, Ministère de l'agriculture de l'agroalimentaire et de la forêt) and approved by the Committee of Ethics of Bordeaux.

### Organotypic hippocampal slice cultures

Organotypic hippocampal slices were prepared from 5-7 days old wild-type mice and cultured for 3–5 weeks using the Gähwiler technique (Gähwiler, 1987; Gähwiler et al, 1997). The main advantage of this culturing method is the very good optical accessibility for an inverted setup as the slice grows directly on a coverslip. Moreover, it can easily be combined with electrophysiology.

The first step of the protocol consists in the preparation of the coverslips. 12x24 mm, 0,17 µm thick coverslips are first heated in ethanol for 30 minutes. Then the coverslips are dried and heated in an oven for at least 3 h at 225 °C. After this step, they are then coated with a poly-L-lysine solution for 20-30 minutes. After drying, the coverslips are washed in distilled water for 20 minutes. The dissection itself consists of the extraction of the hippocampi from the 5-7 days old mice by decapitating the mice, removing the scalp, opening the skull, removing and submerging the brain in cooled and freshly prepared dissection solution with the following composition: 98 ml GBSS (containing in g/L: 0.220 CaCl<sub>2</sub> \* 2 H<sub>2</sub>O; 0.740 KCl; 0.030 KH<sub>2</sub>PO<sub>4</sub>; 0.210 MgCl<sub>2</sub> \* 6 H<sub>2</sub>O; 0.070 MgSO<sub>4</sub> \* 7 H<sub>2</sub>O; 8 NaCl; 0.227 NaHCO<sub>3</sub>;

0.120 Na<sub>2</sub>HPO<sub>4</sub>; 1.100 D(+)-Glucose \* H<sub>2</sub>O); 18,92 mg of kynurenic acid; and 1 ml of glucose solution (1.1g in 1mL of distilled water). The pH was adjusted with 1M HCl to 7.2, sterile filter and stored at 4 °C. The hippocampi are then isolated and placed on the teflon disk of the tissue chopper (McIlwain) that is equipped with a razor blade. Coronal slices of 350 µm are produced and transferred in a new petri dish containing cooled dissection solution for 30-60 minutes. The next step consists in mounting the slices on the glass coverslips by embedding them into a clot of thrombin and chicken plasma. 10 µL of chicken plasma is deposited on the center of the coverslip. A slice is then transferred on the chicken plasma drop before adding 10 µL of thrombin solution (742.5 µl of GBSS; 7.5 µl of glucose solution; 500 µl of thrombin). The chicken plasma and the thrombin are then mixed before leaving the clot to coagulate around the slice for 30 minutes. The coverslips are then transferred into delta tubes (Nunc) before adding 750 µL of culture medium with the following composition: 100 ml of BME medium; 50 ml of HBSS; 50 ml of horse serum; 1 ml of glutamine; 2 ml of glucose. The tubes containing the slices are then placed on a roller-drum incubator set at 35 °C with a rotation speed of 0.1 rpm.

### **Recording solutions**

For the imaging experiments, slice cultures were mounted into a heated recording chamber (32°C) and continuously perfused with carbogenated (95% O<sub>2</sub>, 5% CO<sub>2</sub>) artificial cerebrospinal fluid (ACSF) at pH 7.4 with an osmolarity of 300-310 mOsm containing 124 mM NaCl, 3mM KCl, 2 mM CaCl<sub>2</sub>, 1 mM MgCl<sub>2</sub>, 10 mM glucose, 1.25 mM NaH<sub>2</sub>PO<sub>4</sub>, 26 mM NaHCO<sub>3</sub>, 2.5 mM sodium L-ascorbate, 2 mM trolox (Sigma-Aldrich). The use of antioxidants, ascorbic acid and Trolox helps preventing toxicity due to sample illumination by free radicals from reactive oxygen species.

For the experiments that didn't involve imaging, the composition of the ACSF was identical except that neither Trolox nor ascorbic acid was used.

### Viral infection

For specifically labeling CA3 neurons, a glass micropipette backfilled with Sinbis-GFP diluted in TNE buffer containing 0.1 M NaCl, 0.05M Tris-Cl pH8, 0.5 M EDTA, 0.001% Tween-20, connected to a Picospritzer (Parker), and placed in the cell body layer of the CA3 area. The virus was injected into the tissue by applying a few pressure pulses (50-150 ms; 10-15 psi). The size of the injection area, which appears dark in transmission mode and was visually inspected to keep it confined so that approximately 30-50 neurons get infected (Figure 12).

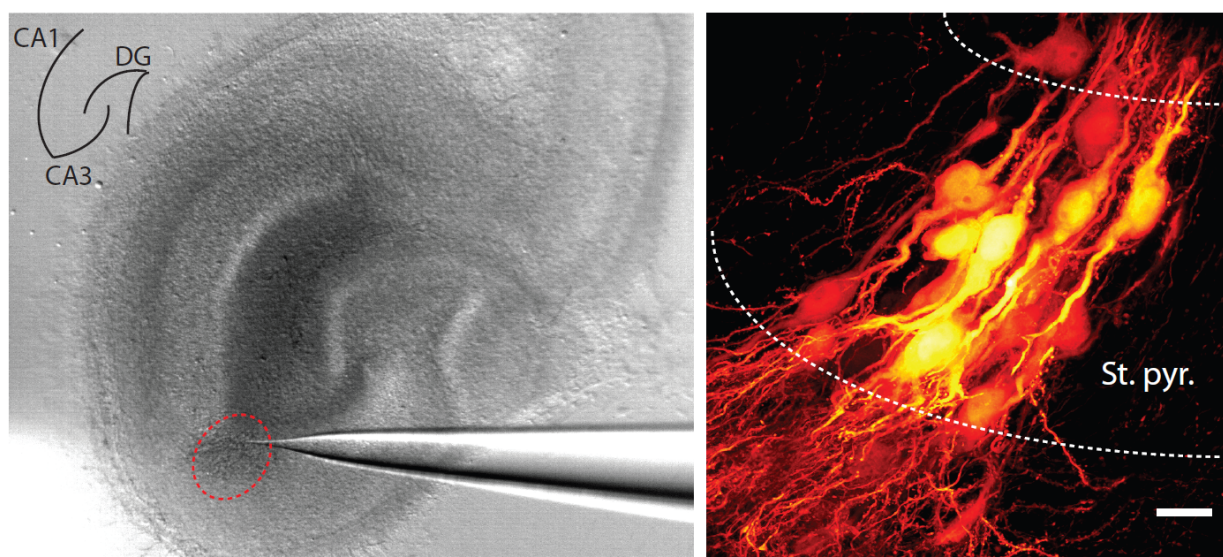


**Figure 12: Local infection CA3 pyramidal neurons using sinbis-GFP.**

*Left.* A glass pipette filled with sinbis-GFP viral particles solution is inserted into the stratum pyramidale of the CA3 area. Few pulses of positive pressure are applied and the affected area is controlled by visual inspection by contrast change (dotted red circle). *Right.* High magnification fluorescence image of the CA3 pyramidal layer 36 h post-infection. Only a small section of CA3 pyramidal neurons are labeled. Scale bar: 20  $\mu\text{m}$ .

Experiments were conducted 36-48 h post-infection giving optimal GFP expression while (Ehrengruber et al, 1999) preserving the physiological health of the cells (Jeromin et al, 2003).

### **Extracellular field recordings**

For the imaging experiments, field excitatory postsynaptic potentials were recorded from the CA1 stratum radiatum using a glass microelectrode (3-5 M $\Omega$ ) filled with ACSF. In order to maximize the number of CA3 labeled fibers undergoing the stimulation, a glass microelectrode (3-5 M $\Omega$ ) filled with ACSF was placed in the middle of the labeled CA3 somata area. Short (0.2 ms) current pulses were delivered from a stimulus isolator (AMPI). The stimulus strength (ranging between 10-35  $\mu$ A) was adjusted to elicit a fEPSP of 50% of the maximal amplitude for LTP and control experiments and 66% for LTD experiments. The fEPSPs were recorded from Digidata 1440A and Multiclamp 700B (Axon CNS; Molecular Devices). Amplifier gain was set at 20 and a Bessel filter of 2 kHz was applied. A test pulse was recorded every 15 s (0.067 Hz) through the whole experiment. The stimuli protocols consisted of 3 trains with 20 s interval of 100 pulses delivered at 100 Hz to induce LTP; 900 pulses delivered at 1 Hz to induce LTD and started after recording a baseline of 20 min. The initial slopes of the fEPSPs were determined with Clampfit 10.1 (Axon instruments). Some experiments were performed in the presence of the NMDA receptor antagonist, D-APV, to prevent the induction of an LTP.

For the electrophysiological experiments that involved patch-clamp recording of CA3 pyramidal neurons, the stimulation pipette was placed in the CA1 radiatum in between the extracellular field recording electrode (placed in the distal part of the CA1) and the CA3.

### **Patch-clamp recordings**

Current-clamp recordings were obtained from CA3 pyramidal cells to record the arrival time of an antidromic AP generated distally on the axon.

Patch-clamp glass electrodes (1.5 x 1.17mm, Harvard Apparatus, 3-5 M $\Omega$ ) were filled with the following solution (in mM) : 115 KMeSO<sub>3</sub>, 10.3 Na<sup>+</sup> (NaOH, Na-ATP, Na-GTP), 4.6 MgCl<sub>2</sub>, 40 HEPES, 1 EGTA, 4 ATP, 0.3 GTP, osmolarity =275–280, pH: 7.3. Once the seal between the cell membrane and the glass electrode reached 1G $\Omega$ , whole-cell mode was used and cells were clamped at -70mV. Those presenting an access resistance (Ra) greater than 25 M $\Omega$  or and injected current greater than -100 pA were excluded from the experiment. CA3 cells were recorded in current clamp with a dynamic current injection correction to maintain the resting membrane at -70 mV. Amplifier (Multiclamp 700A) gain was set at 1 and a Bessel filter of 2 kHz was applied. To elicit an antidromic AP, a glass electrode back-filled with ACSF was placed in the distal part of the CA1 and then moved toward the CA3 until an AP could be recorded reliably at the soma. Short (0.1 ms) current pulses were delivered from a stimulus isolator (AMPI) with a stimulation strength ranging between 25-75  $\mu$ A. Excitatory field recordings was performed simultaneously with the same stimulation electrode in order to monitor the induction of plasticity.

### **Inverted single-photon STED setup**

For live-cell imaging of hippocampal brain slice cultures, we use a custom-built STED microscope based on pulsed excitation and pulsed depletion in the visible range of the spectrum (Figure 13). A standard commercial inverted microscope (DMI 6000 CS Trino, Leica, Mannheim, Germany) equipped with a high-numerical-aperture objective lens (PL APO, 100 $\times$ , oil, NA 1.4, Leica) served as a base. For excitation, a pulsed-laser diode (PDL 800-D, Picoquant, Berlin, Germany) was used delivering 90 ps pulse duration at 485 nm

wavelength. For fluorescence quenching, 595 nm wavelength laser pulses for the STED beam were produced by an optical parametric oscillator (OPO BASIC Ring fs RTP, APE, Berlin, Germany) pumped by a Ti:Sapphire laser (MaiTai, Spectra-Physics, Darmstadt, Germany), operating at 80 MHz and emitting at 800 nm. The pulses of originally 200 fs duration were stretched to ~68 ps by first dispersion in a glass rod 25 cm long (SF6) and then in a polarization-preserving fiber (Schäfter & Kirchhoff, Hamburg, Germany) of 20 m length. To create the STED focal doughnut, a polymeric phase plate (RPC Photonics, Rochester, NY) was introduced into the STED beam path. The STED and excitation pulses were synchronized at 80 MHz via external triggering of the laser diode using an electronic delay generator. The laser beams were combined using a dichroic mirror (AHF Analysentechnik, Tübingen, Germany). We used a telecentric beam scanner (Yanus IV, TILL Photonics, Gräfelfing, Germany) in combination with scan and tube lenses from the microscope manufacturer to stir the laser beams across the sample. The fluorescence signal was detected in a descanned fashion and separated from the excitation by a dichroic mirror (499 nm long-pass), then cleaned with a 525/50 band-pass filter and finally focused onto a multimode optical fiber connected to an avalanche photodiode (SPCM-AQR-13-FC, PerkinElmer, Waltham, MA). Image acquisition was controlled by the custom-written software IMSpector (IMSpector).

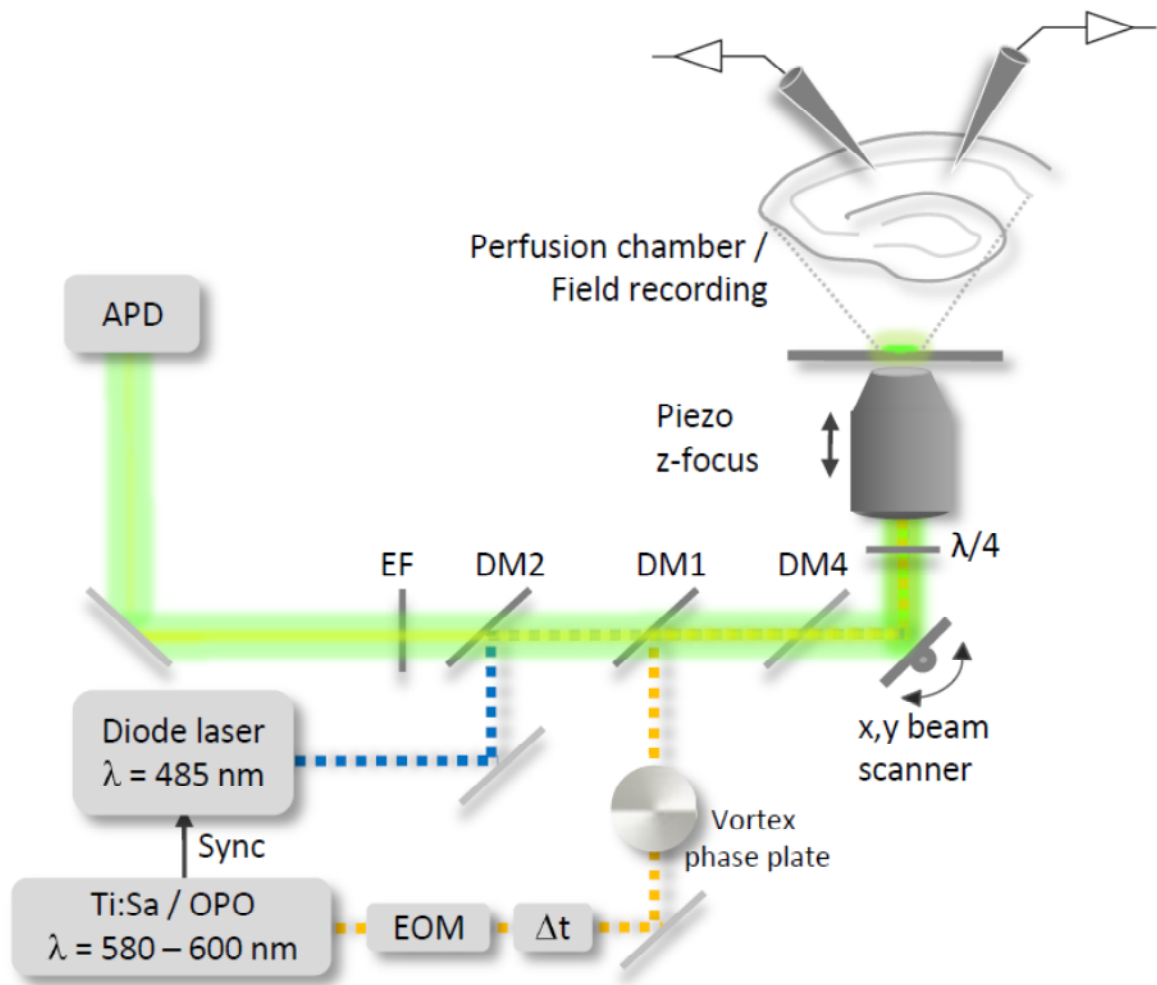


**Figure 13: Optical design of the home-built inverted STED microscope for opto-physiology in brain slices.**

The diode laser used for excitation is routed through a beam scanner into an upright microscope and synchronized with the STED laser (Ti:Sa/optical parametric oscillator (OPO)). Femtosecond pulses emitted from the Ti:Sa/OPO are broadened by a 20-m-long polarization-preserving single-mode fiber. The doughnut is formed by a helical phase mask (Vortex phase plate). An oil immersion objective is used.  $\lambda/2$ , half-wave plate;  $\lambda/4$ , quarter-wave plate; DC, dichroic mirrors, NA, numerical aperture;  $\Delta t$ , pulse broadening fiber; xy-scan, scanner for x and y dimension; APD, avalanche photodiode; EOM, electro-optical modulator.

**Image acquisition**

The parameters of acquisition were originally defined so that neither apparent photodamage nor excessive photobleaching was detected over the time course of the experiment. All the image acquisitions were performed with an excitation power of 4-6  $\mu\text{W}$  and a STED power of  $\sim 8$  mW (objective back aperture measurements). The images stacks were acquired with a voxel size of 19.5 nm (xy); 375 nm (z) and dwell time of 15  $\mu\text{s}$ , unless stated otherwise. Imaging depths into the slice, determined by the z-piezo focus, the fluorescence on top of the slice defining the zero z-position, was ranging between 5-15  $\mu\text{m}$ . For the plasticity experiments, an area containing multiple and well separated axon stretches was selected. Z-stacks of  $30 \times 20 \times 3 \mu\text{m}$  (x, y and z dimensions respectively) were acquired every  $\sim 10$  min for 1 hour. Two acquisitions were performed before the stimulus and four after.

**Image analysis**

Images were exported from the IMSpector software into an 8-bit tiff file format. We used NIH ImageJ for processing the acquisitions. Image analysis was done on raw data and images presented in the figures were filtered by a 1-pixel median filter to reduce noise. A screening by visual inspection was performed and only the signal of the axon stretches that were fully contained into the volume of acquisition at all time points was selected for the morphometric analysis. A maximum intensity projection was performed on the regions of interest. To realize the automated morphometric measurement, a reference image that consist of a line of pixels running along the axon stretch was produced by first, thresholding and binarize the picture, then we used the skeletonize plugin from ImageJ. A custom written Matlab program was used to automatically measure the FWHM along the axon image using the reference image that determines the position of the measurement. At every position, it automatically estimates the best tangential fit and plots the intensity profile from its orthogonal. To reduce

the noise coming from the measurement and the imaging, an average of 5 parallel lines is done. Considering that the cytoplasmic fluorescence concentration might be inhomogeneous, no assumption was made on the intensity plot profile distribution; therefore the FWHM was directly extracted from the raw intensity profile. Diameter profiles of full axon stretches could then be generated and analyzed further. For the plasticity experiments, 1  $\mu\text{m}$  axon shaft portions were selected from the automatically generated FWHM profiles excluding the varicosities by visual inspection. Average diameters were calculated over time for each 1  $\mu\text{m}$ . To determine the bouton size change over time, all boutons from all the experiments were automatically analysed by measuring the FWHM along the boutons. Bouton areas could be determined by summing all the FWHM measured and multiplied by the pixel size.

## Simulations

The propagation of action potentials into axon branches was simulated using the compartment model program NEURON version 7.3 (Carnevale & Hines, 2006). The properties of each compartment can be defined independently. Axon branches were measured with the STED microscope (see above). A text file containing the diameter profile along the studied branch was used to build a simulation model. The simulation model was composed of unmyelinated excitable compartments, described by standard (Hodgkin & Huxley, 1952a; Hodgkin & Huxley, 1952b) channel kinetic equations.

### *Geometry*

The simulation model was made of 4 sections: to give the model a realistic behavior (i.e. in order to avoid sealed effects from interfering with the analysis), the *simulated branch* (3) was included after a 500  $\mu\text{m}$  *proximal axon* (2) (used to simulate realistic incoming spike), and before a *distal axon* (4) of 200  $\mu\text{m}$  in which spikes propagate after traveling in the simulated branch. Spikes were initiated in an *initial segment* (1) in which a current pulse was

generated before accessing the 500  $\mu\text{m}$  axon. In each section, the number of segments was calculated to get a length/diameter ratio  $\leq 5$ . The temporal integration step was 100  $\mu\text{s}$ .

### *Passive properties*

The intra-compartmental potential,  $E$ , is described by the differential equation

$$\frac{dE}{dt} = \frac{I_{\text{leak}} + I_{\text{core}} + I_{\text{ch}}}{cm}$$

where  $I_{\text{leak}}$  is the passive leakage current:  $I_{\text{leak}} = (E_{\text{leak}} - E) \times G_{\text{leak}}$

and  $E_{\text{leak}}$  and  $G_{\text{leak}}$  are the equilibrium potential and the leak conductance, respectively.

$I_{\text{core}}$  is the axial current to neighboring compartments summed over all neighbors

$$I_{\text{core}} = \sum_{c \in \text{neighbors}} (E_c - E) \times G_{\text{core}}$$

The parameter  $G_{\text{core}}$  (in S) denotes the core conductance from the compartment in question to

the neighboring compartment:  $G_{\text{core}} = \frac{\pi \times \text{diam}^2}{4} \times \frac{1}{l} \times \frac{1}{R_a}$

where  $\text{diam}$  and  $l$  are diameter and length of the compartment (in cm), respectively;  $R_a$  is the specific resistance of the axoplasm (in  $\Omega \cdot \text{cm}$ ).

$I_{\text{ch}}$  in equation (1) is intrinsic currents. Intracellular current injection can be modeled by adding current to the compartment. The parameter  $cm$  ( $\mu\text{F}$ ) describes the capacitance of the compartment

$$cm = C_m \times \text{area}$$

( $\text{area}$  is the membrane surface of the compartment in  $\text{cm}^2$ ,  $C_m$  is the specific capacitance in  $\mu\text{F} \cdot \text{cm}^{-2}$ )

All compartments had the same specific membrane resistance ( $R_m$ ) set to 10000  $\Omega \cdot \text{cm}^2$ . All computations were carried out assuming a specific capacitance,  $C_m$  of  $1 \mu\text{F}/\text{cm}^2$  and a specific axoplasmic resistance,  $R_a$ , of 100  $\Omega \cdot \text{cm}$ .

*Sodium and potassium channels*

**Sodium (Na<sup>+</sup>) current** is computed as:  $I_{Na} = (E_{Na} - E) \cdot G_{Na} \cdot m^3 \cdot h$

The activation variable  $m$  is described by  $\frac{dm}{dt} = \alpha_m \cdot (1 - m) - \beta_m \cdot m$

with rate functions  $\alpha_m$  and  $\beta_m$

$$\alpha_m = \frac{A_{\alpha_m} \times k_{\alpha_m} \times (E - d_{\alpha_m})}{1 - e^{-k_{\alpha_m} \times (E - d_{\alpha_m})}} \quad \beta_m = A_{\beta_m} \times e^{k_{\beta_m} \times (E - d_{\beta_m})}$$

The inactivation variable  $h$  is computed in a similar way.  $\frac{dh}{dt} = \alpha_h \cdot (1 - h) - \beta_h \cdot h$

With rate functions  $\alpha_h$  and  $\beta_h$

$$\alpha_h = A_{\alpha_h} \times e^{k_{\alpha_h} \times (E - d_{\alpha_h})} \quad \beta_h = \frac{A_{\beta_h}}{1 + e^{-k_{\beta_h} \times (E - d_{\beta_h})}}$$

In most computations, we used the following values for the Na<sup>+</sup> channel parameters (IS):

Activation  $m$ :

$$A_{\alpha_m} = 1 \text{ ms}^{-1}; k_{\alpha_m} = 0.1 \text{ mV}^{-1}; d_{\alpha_m} = -40 \text{ mV};$$

$$A_{\beta_m} = 4 \text{ ms}^{-1}; k_{\beta_m} = -0.055 \text{ mV}^{-1}; d_{\beta_m} = -65 \text{ mV}$$

Inactivation  $h$ :

$$A_{\alpha_h} = 0.07 \text{ ms}^{-1}; k_{\alpha_h} = -0.05 \text{ mV}^{-1}; d_{\alpha_h} = -65 \text{ mV};$$

$$A_{\beta_h} = 1 \text{ ms}^{-1}; k_{\beta_h} = -0.1 \text{ mV}^{-1}; d_{\beta_h} = -35 \text{ mV}$$

The maximum conductance density for Na<sup>+</sup> channels in a given compartment was  $G_{Na} \text{ Max} = 0.6 \text{ S.cm}^{-2}$  in the initial segment, and  $G_{Na} \text{ Max} = 0.012 \text{ S.cm}^{-2}$  in other sections of the model. The equilibrium potential for Na<sup>+</sup> ions was set  $E_{Na} = +50 \text{ mV}$ .

**Potassium (K<sup>+</sup>) current** is computed as:  $I_K = (E_K - E) \cdot G_K \cdot n^4$

Its activation variable,  $n$ , is described by the equation :  $\frac{dn}{dt} = \alpha_n \cdot (1 - n) - \beta_n \cdot n$

with rate functions  $\alpha_n$  and  $\beta_n$

$$\alpha_n = \frac{A_{\alpha_n} \times k_{\alpha_n} \times (E - d_{\alpha_n})}{1 - e^{-k_{\alpha_n} \times (E - d_{\alpha_n})}} \quad \beta_n = A_{\beta_n} \times e^{k_{\beta_n} \times (E - d_{\beta_n})}$$

In all computations, we used the following values for the  $K^+$  channel parameters:

$$A_{\alpha_n} = 0.1 \text{ ms}^{-1}; k_{\alpha_n} = 0.1 \text{ mV}^{-1}; d_{\alpha_n} = -55 \text{ mV};$$

$$A_{\beta_n} = 0.125 \text{ ms}^{-1}; k_{\beta_n} = -0.0125 \text{ mV}^{-1}; d_{\beta_n} = -65 \text{ mV}$$

The maximum conductance density was  $G_{K\text{Max}} = 0.19 \text{ S.cm}^{-2}$  in the initial segment, and  $0.0036 \text{ S.cm}^{-2}$  in the other sections of the model. The equilibrium potential for  $K^+$  ions was  $E_K = -77 \text{ mV}$ .

## Statistics

For the plasticity experiments, we expressed the values as normalized mean  $\pm$  standard error of mean. We performed a two-way repeated ANOVA, to test the effect of time, the interaction between groups and change over time, and the effect between groups. The homogeneity of variances for every timepoints was tested using a Levene test, for the timepoints that were not significant, a post-hoc Bonferroni test was performed otherwise we performed a post-hoc Dunnett test.

## RESULTS

The results section is composed of two parts:

**Part 1** is a research article in preparation and formatted in the style of a scientific journal describing the activity-dependent regulation of axon morphology and function in living brain slices. In this project, I designed, performed and analyzed the imaging and electrophysiological experiments. The computer models were built by our collaborator, Daniel Cattaert; he and I ran the simulation-based experiments.

**Part 2** is a research article published in Biophysical Journal on February 2013 describing the development of a novel type of STED microscope based on two-photon excitation. In this project, I contributed to the design and building off the microscope.

**Part 1: Activity-dependent morphological dynamics of CA3 axons and modulation of action potential conduction velocity.****Aim of the study:**

According to the traditional view axons are faithful and static conductors of action potentials (AP) generated at the cell body. However, recently it has become evident that axons can strongly and dynamically influence AP propagation, e.g. AP speed and waveform, which is thought to powerfully broaden the computational repertoire of neural circuits.

Axon morphology is likely to be an important determinant of AP propagation within the axonal tree, because basic structural parameters (such as axon diameter) largely define the passive electrical properties of axons. However, because most axons in the central nervous system are so thin, it has been impossible to image axons, let alone their activity-dependent dynamics, in live tissue using conventional light microscopy, which does not offer nearly enough spatial resolution.

To overcome this limitation and to investigate the plastic structural changes of hippocampal axons in living brain slices, we used a novel combination of superresolution STED microscopy, electrophysiology and biophysical modeling using the NEURON simulation environment.

**Methodology:**

We used a custom-built STED microscope (spatial resolution around 50 nm) for visualizing the structural dynamics of GFP-labeled Schaffer collateral axons. Axon diameters were monitored using quantitative analysis in baseline conditions and after HFS-induced LTP of CA3-CA1 synapses. Using the STED morphology data, we built a realistic NEURON model of Schaffer collateral axons to systematically explore the influence of nanoscale axon

morphology on AP propagation. We performed antidromic AP latency measurements using patch-clamp recordings and extracellular stimulations of the axon.

**Results:**

STED imaging revealed that live CA3 axons are on average 200 nm wide, ranging from 100 to 350 nm, in keeping with previous EM reports. Axons can undergo local fluctuations in diameter under baseline conditions. However altogether, the populations of axons were very stable over a period of an hour. Interestingly, induction of LTP caused a significant and persistent enlargement of axon diameters. Using patch-clamp recordings and antidromic stimulation, we correlated the axon diameter increase with an increased conduction velocity of APs following LTP induction.

Taken together, our findings indicate that axons dynamically tune AP propagation by changing their diameters, thereby alter the timing of information transfer in neural circuits, suggesting a novel and powerful structural mechanism for neural plasticity.

## **Structural plasticity regulates propagation delays of action potentials in hippocampal axons**

Ronan Chereau<sup>1,2</sup>, Daniel Cattaert<sup>3</sup> and U. Valentin Nägerl<sup>1,2</sup>

<sup>1</sup>Interdisciplinary Institute for Neuroscience (IINS), Université de Bordeaux, France

<sup>2</sup>UMR 5297, Centre National de la Recherche Scientifique (CNRS), Bordeaux, France

<sup>3</sup>Centre de Neurosciences Intégratives et Cognitives, CNRS-UMR 5228 et Université de Bordeaux, France

**Running Title:** Axon plasticity regulates velocity of action potentials

**ABSTRACT**

Precise timing of electrical signalling is critically important for many kinds of computations performed by neural circuits, such as action potential firing, spike-timing dependent synaptic plasticity and temporal coding of sensory inputs.

The transmission of APs over unmyelinated axons is an inherently slow process, which causes major time delays for synaptic communication, taking up to hundreds of milliseconds. While it is clear that travel distance and morphological properties of the axon largely set this conduction delay, very little is known about whether and how it may be physiologically regulated.

We combined time-lapse superresolution stimulated emission depletion (STED) microscopy with electrophysiology and computer simulations to investigate the relationship between axon morphology and AP conduction in CA3 pyramidal neurons in living mouse organotypic hippocampal brain slices.

Our study reveals that axon morphology, which is very heterogeneous, is largely stable under baseline conditions. By contrast, after the induction of LTP in the CA3-CA1 synaptic pathway we observed remodelling of presynaptic boutons and axon shafts that correlates with bi-directional changes in AP conduction velocity measured by patch clamp recordings and predicted by biophysical modeling.

Our findings indicate that AP propagation delay is regulated by activity-driven changes in axon morphology, suggesting a novel structural mechanism for fine-tuning the timing of information transfer in neural circuits.

---

## INTRODUCTION

Precise timing of neuronal activity is essential for network synchrony and circuit plasticity in the brain. Timing variations of synaptic inputs on the order of a few milliseconds can decide over action potential firing<sup>1</sup> and the direction of synaptic plasticity<sup>2,3</sup>.

Neural timing ultimately is defined by the anatomy and biophysics of the underlying neural structures, which impose characteristic time delays on electrical signals as they get integrated and transmitted. The possibility that time delays are plastic variables has not been explored much experimentally, for technical reasons but also because neural plasticity is mostly studied as a change in signal amplitude (rather than signal timing). Hence, we know very little about whether and how time delays are physiologically regulated and what this may mean for information processing in the brain.

A major source of time delay arises from the conduction of action potentials (AP) along axons. It can take tens of milliseconds for an AP to travel from the axon initial segment (AIS) to the presynaptic terminal, depending on distance<sup>4</sup>. To conduct APs at very high speed axons need to be myelinated or have large core diameters. However, most axons in the hippocampus, including the Schaffer collaterals from CA3 neurons, are unmyelinated and extremely thin (between 100-300 nm<sup>5</sup>), conducting APs at a speed of less than 300  $\mu\text{m}/\text{msec}$ <sup>4</sup>.<sup>6</sup> This imposes long delays on AP propagation (between 5-10 milliseconds), despite short travel distances to postsynaptic targets in the CA1 area (less than a few millimeters).

The experimental difficulty to record electrophysiologically from single axon fibers and to measure accurately their nanoscale morphology in living tissue has hampered our ability to investigate whether the delay of axonal AP propagation is a dynamically regulated variable, let alone if and how it may be affected by structural changes in the axon. Recent studies

based on two-photon imaging and/or electrophysiology have discussed this as a possibility, demonstrating that the induction of synaptic plasticity causes in tandem morphological and functional changes in axonal compartments<sup>7-10</sup>.

However, it remains an open question whether thin unmyelinated axons undergo activity-dependent changes in their diameter that might influence the propagation of APs. This knowledge gap is largely because conventional light microscopy does not provide enough spatial resolution and electron microscopy cannot be used for longitudinal studies. By contrast, STED microscopy can faithfully resolve axon morphology and is compatible with functional assays in living brain tissue<sup>11, 12</sup>.

Here, we used a combination of time-lapse STED imaging, electrophysiology and biophysical modelling to investigate activity-dependent structural plasticity of axons and assess its impact on AP propagation in organotypic brain slices.

We demonstrate that the induction of LTP leads to orchestrated increases in presynaptic boutons and axon shafts, which are correlated with bidirectional changes in AP conduction velocity. Our study suggests a novel type of morpho-functional plasticity whereby axon morphology dynamically regulates AP conduction delays in hippocampal axons.

---

## METHODS

### Animals

Wild-type mice were kept under 12 h light/ 12 h dark cycle with *ad libitum* access to food and water (strain from Jackson Labs, Bar Harbor, ME). Experimental procedures were in accordance with the French National Code of Ethics on Animal Experimentation and approved by the Committee of Ethics of Bordeaux (no. 50120202).

### Organotypic hippocampal slice cultures

Organotypic hippocampal slice cultures (Gähwiler type) were dissected from 5- to 7-day old pups of wild-type mice and cultured 3–5 weeks at 35 °C in a roller drum at 10 revolutions per hour as previously described<sup>13, 14</sup>. In brief, hippocampi were chopped coronally at 350 µm using a tissue chopper and embedded in a freshly mixed plasma/thrombin clot on the surface of a poly-L-lysine (PLL)-coated glass coverslip. After coagulation, the slice on the coverslip was cultured in a roller tube in 0.5 ml of medium consisting of 50% Eagle's basal medium, 25% horse serum and 25% Hank's balanced salt solution, supplemented with glutamine to a final concentration of 1 mM and glucose (11 g/l) (all from Sigma). The Gähwiler cultures are optically very accessible, as synapses close to the coverslip can be imaged on an inverted microscope setup.

### Recording solutions

For the imaging experiments, slice cultures were mounted into a heated recording chamber (32°C) and continuously perfused with carbogenated (95% O<sub>2</sub>, 5% CO<sub>2</sub>) artificial cerebrospinal fluid (ACSF) at pH 7.4 with an osmolarity of 300-310 mOsm containing 124 mM NaCl, 3mM KCl, 2 mM CaCl<sub>2</sub>, 1 mM MgCl<sub>2</sub>, 10 mM glucose, 1.25 mM NaH<sub>2</sub>PO<sub>4</sub>, 26 mM NaHCO<sub>3</sub>, 2.5 mM sodium L-ascorbate, 2 mM trolox (Sigma-Aldrich). The use of antioxidants, ascorbic acid and Trolox helps preventing toxicity due to sample illumination by free radicals from reactive oxygen species. For the experiments that didn't involve

---

imaging, the composition of the ACSF was identical except that neither Trolox nor ascorbic acid was used.

### **Viral infection**

For specifically labelling CA3 neurons, a glass micropipette backfilled with Sindbis-GFP viral particles diluted in TNE buffer containing 0.1 M NaCl, 0.05M Tris-Cl pH8, 0.5 M EDTA, 0.001% Tween-20, connected to a pressure-injection device (Picospritzer, Parker), and positioned into the cell body layer of the CA3 area of the hippocampus. The virus was injected into the tissue by applying a few pulses of positive pressure (50-150 ms; 10-15 psi). The size of the injection area, which appears dark in transmission mode and was visually inspected to keep it confined so that approximately 30-50 neurons get infected. Experiments were conducted 36-48 h post-infection giving optimal GFP expression<sup>15</sup> while preserving the physiological health of the cells<sup>16</sup>.

### **Electrophysiology**

For the imaging experiments, field excitatory postsynaptic potentials were recorded from the CA1 *stratum radiatum* using a glass microelectrode (tip resistance ~3-5 M $\Omega$ ) filled with ACSF. In order to maximize the overlap between fibers that are labelled and that experience the stimulation, a monopolar stimulating electrode (glass microelectrode ~3-5 M $\Omega$  filled with ACSF) was placed in the middle of the area of labelled CA3 cell bodies. Brief (0.2 ms) current pulses were delivered from a stimulus isolator (AMPI). The stimulus strength (ranging between 10-35  $\mu$ A) was adjusted to elicit fEPSP corresponding to 50% of their maximal amplitude. The fEPSPs were recorded using a patch clamp amplifier (Multiclamp 700B; Molecular Devices). Amplifier gain was set at 20X and a Bessel filter of 2 kHz was applied. A test pulse was recorded every 15 s (0.067 Hz) throughout the experiment. The stimulus protocol consisted of 3 trains of 100 pulses delivered at 100 Hz and 20 seconds apart to induce LTP and started after recording a baseline of 20 min. The initial slopes of the

---

fEPSPs were determined with Clampfit 10.1 (Molecular Devices). Some experiments were performed in the presence of the NMDA receptor antagonist, D-APV.

Whole-cell patch clamp recordings were performed using glass capillaries (tip resistance ~3-5 M $\Omega$ ) with the following solution (in mM): 115 KMeSO<sub>3</sub>, 10.3 Na<sup>+</sup> (NaOH, Na-ATP, Na-GTP), 4.6 MgCl<sub>2</sub>, 40 HEPES, 1 EGTA, 4 mM ATP, 0.3 GTP, osmolarity = 275–280 mosmol, pH 7.3. Recordings where the access resistance (R<sub>a</sub>) exceeded 25 M $\Omega$  or with holding currents greater than -100 pA were excluded from analysis. CA3 cells were recorded in current clamp mode with a dynamic current injection correction to maintain the resting membrane at -70 mV. The gain of the patch clamp amplifier was set at 1X and a Bessel filter of 2 kHz was applied. To elicit an antidromic AP, a glass electrode back-filled with ACSF was placed in the distal part of the CA1 area and then moved toward the CA3 until an AP could be recorded reliably at the soma. Short (0.1 ms) current pulses were delivered from a stimulus isolator (AMPI) with a stimulation strength ranging between 25-75  $\mu$ A. Excitatory field recordings was performed simultaneously with the same stimulation electrode in order to monitor the induction of plasticity.

### **STED microscopy**

For live-cell imaging of hippocampal brain slice cultures, we used a home-built STED microscope based on pulsed excitation and pulsed depletion in the visible range of the spectrum. A standard commercial inverted microscope (DMI 6000 CS Trino, Leica, Mannheim, Germany) equipped with a high-numerical-aperture objective lens (PL APO, 100 $\times$ , oil, NA 1.4, Leica) served as a base. For excitation, a pulsed-laser diode (PDL 800-D, Picoquant, Berlin, Germany) was used delivering 90 ps pulse duration at 485 nm wavelength. For depletion, 595 nm wavelength laser pulses for the STED beam were produced by an optical parametric oscillator (OPO BASIC Ring fs RTP, APE, Berlin, Germany) pumped by a Ti:Sapphire laser (MaiTai, Spectra-Physics, Darmstadt, Germany), operating at 80 MHz and

---

emitting at 800 nm. The pulses of originally 200 fs duration were stretched to ~68 ps by first dispersion in a glass rod 25 cm long (SF6) and then in a polarization-preserving fiber (Schäfter & Kirchhoff, Hamburg, Germany) of 20 m length. To create the STED focal doughnut, a polymeric phase plate (RPC Photonics, Rochester, NY) was introduced into the STED beam path. The STED and excitation pulses were synchronized at 80 MHz via external triggering of the laser diode using an electronic delay generator. The laser beams were combined using a dichroic mirror (AHF Analysentechnik, Tübingen, Germany). We used a telecentric beam scanner (Yanus IV, TILL Photonics, Gräfelfing, Germany) in combination with scan and tube lenses from the microscope manufacturer to stir the laser beams across the sample. The fluorescence signal was detected in a descanned fashion and separated from the excitation by a dichroic mirror (499 nm long-pass), then cleaned with a 525/50 band-pass filter and finally focused onto a multimode optical fiber connected to an avalanche photodiode (SPCM-AQR-13-FC, PerkinElmer, Waltham, MA). Image acquisition was controlled by the custom-written software IMSpector<sup>17</sup>.

### **Image acquisition**

The parameters of acquisition were originally defined so that neither apparent photodamage nor excessive photobleaching was detected over the time course of the experiment. All the image acquisitions were performed with an excitation power of 4-6  $\mu$ W and a STED power of ~8 mW (measured at the objective back aperture). The images stacks were acquired with a voxel size of 19.5 nm (xy); 375 nm (z) and dwell time of 15  $\mu$ s. Imaging depths into the slice, determined by the z-piezo focus, the fluorescence on top of the slice defining the zero z-position, was ranging between 5-15  $\mu$ m. For the plasticity experiments, an area containing multiple and well separated axon stretches was selected. Z-stacks of 30x20x3 $\mu$ m (x, y and z dimensions respectively) were acquired every ~10 min for 1 hour. Two acquisitions were performed before the stimulus and four after.

---

## Image analysis

Images were exported from the IMSpector software into an 8-bit tiff file format. We used NIH ImageJ for processing the acquisitions. Image analysis was done on raw data and images presented in the figures were filtered by a 1-pixel median filter to reduce noise. A screening by visual inspection was performed and only the signal of the axon stretches that were fully contained into the volume of acquisition at all time points was selected for the morphometric analysis. A maximum intensity projection was performed on the regions of interest. To realize the automated morphometric measurement, a reference image that consist of a line of pixels running along the axon stretch was produced by first, thresholding and binarize the picture, then we used the skeletonize plugin from ImageJ. A custom written Matlab program was used to automatically measure the FWHM along the axon image using the reference image that determines the position of the measurement. At every position, it automatically estimates the best tangential fit and plots the intensity profile from its orthogonal. To reduce the noise coming from the measurement and the imaging, an average of 5 parallel lines is done. Considering that the cytoplasmic fluorescence concentration might be inhomogeneous, no assumption was made on the intensity plot profile distribution; therefore the FWHM was directly extracted from the raw intensity profile. Diameter profiles of full axon stretches could then be generated and analyzed further. For the plasticity experiments, 1  $\mu\text{m}$  axon shaft portions were selected from the automatically generated FWHM profiles excluding the varicosities by visual inspection. Average diameters were calculated over time for each 1  $\mu\text{m}$ . To determine the bouton size change over time, all boutons from all the experiments were automatically analysed by measuring the FWHM along the boutons. Bouton areas could be determined by summing all the FWHM measured and multiplied by the pixel size.

## Simulations

The propagation of action potentials into axon branches was simulated using the compartment model program NEURON version 7.3<sup>18</sup>. The properties of each compartment can be defined independently. Axon branches were measured with the STED microscope (see above). A text file containing the diameter profile along the studied branch was used to build a simulation model. The simulation model was composed of unmyelinated excitable compartments, described by standard<sup>19,20</sup> channel kinetic equations.

### *Geometry of model axon*

The simulation model was made of 4 sections: to give the model a realistic behavior (i.e. in order to avoid sealed effects from interfering with the analysis), the *simulated branch* (3) was included after a 500  $\mu\text{m}$  *proximal axon* (2) (used to simulate realistic incoming spike), and before a *distal axon* (4) of 200  $\mu\text{m}$  in which spikes propagate after traveling in the simulated branch. Spikes were initiated in an *initial segment* (1) in which a current pulse was generated before accessing the 500  $\mu\text{m}$  axon. In each section, the number of segments was calculated to get a length/diameter ratio  $\leq 5$ . The temporal integration step was 100  $\mu\text{s}$ . The tested sequences consisted in a mirrored repetition of diameter profiles obtained after automated analysis of axon stretches acquired in STED mode and normalized to a length of 500 nm in order to avoid edge effects.

### *Passive electrical properties*

The intra-compartmental potential,  $E$ , is described by the differential equation

$$\frac{dE}{dt} = \frac{I_{leak} + I_{core} + I_{ch}}{cm} \quad (\text{Equation 1})$$

where  $I_{leak}$  is the passive leakage current:  $I_{leak} = (E_{leak} - E) \times G_{leak}$  (Equation 2)

and  $E_{leak}$  and  $G_{leak}$  are the equilibrium potential and the leak conductance, respectively.

$I_{core}$  is the axial current to neighboring compartments summed over all neighbors

$$I_{core} = \sum_{c \in neighbors} (E_c - E) \times G_{core} \quad (\text{Equation 3})$$

The parameter  $G_{core}$  (in S) denotes the core conductance from the compartment in question to

the neighboring compartment:

$$G_{core} = \frac{\pi \times diam^2}{4} \times \frac{1}{l} \times \frac{1}{R_a}$$

where  $diam$  and  $l$  are diameter and length of the compartment (in cm), respectively ;  $R_a$  is the specific resistance of the axoplasm (in  $\Omega.cm$ ).

$I_{ch}$  in equation (1) is intrinsic currents. Intracellular current injection can be modeled by adding current to the compartment. The parameter  $cm$  ( $\mu F$ ) describes the capacitance of the compartment

$$cm = C_m \times area$$

( $area$  is the membrane surface of the compartment in  $cm^2$ ,  $C_m$  is the specific capacitance in  $\mu F.cm^{-2}$ )

All compartments had the same specific membrane resistance ( $R_m$ ) set to  $10000 \Omega.cm^2$ . All computations were carried out assuming a specific capacitance,  $C_m$  of  $1\mu F/cm^2$  and a specific axoplasmic resistance,  $R_a$ , of  $100 \Omega.cm$ .

### *Sodium and potassium channels*

**Sodium ( $Na^+$ ) current** is computed as:  $I_{Na} = (E_{Na} - E).G_{Na}.m^3.h$

The activation variable  $m$  is described by

$$\frac{dm}{dt} = \alpha_m.(1 - m) - \beta_m.m$$

with rate functions  $\alpha_m$  and  $\beta_m$

$$\alpha_m = \frac{A_{\alpha_m} \times k_{\alpha_m} \times (E - d_{\alpha_m})}{1 - e^{-k_{\alpha_m} \times (E - d_{\alpha_m})}} \quad \beta_m = A_{\beta_m} \times e^{k_{\beta_m} \times (E - d_{\beta_m})}$$

The inactivation variable  $h$  is computed in a similar way.  $\frac{dh}{dt} = \alpha_h \cdot (1-h) - \beta_h \cdot h$

With rate functions  $\alpha_h$  and  $\beta_h$

$$\alpha_h = A_{\alpha_h} \times e^{k_{\alpha_h} \times (E - d_{\alpha_h})} \quad \beta_h = \frac{A_{\beta_h}}{1 + e^{-k_{\beta_h} \times (E - d_{\beta_h})}}$$

In most computations, we used the following values for the Na<sup>+</sup> channel parameters (IS):

Activation  $m$ :

$$A_{cm} = 1 \text{ ms}^{-1}; k_{cm} = 0.1 \text{ mV}^{-1}; d_{cm} = -40 \text{ mV};$$

$$A_{\beta m} = 4 \text{ ms}^{-1}; k_{\beta m} = -0.055 \text{ mV}^{-1}; d_{\beta m} = -65 \text{ mV}$$

Inactivation  $h$ :

$$A_{ch} = 0.07 \text{ ms}^{-1}; k_{ch} = -0.05 \text{ mV}^{-1}; d_{ch} = -65 \text{ mV};$$

$$A_{\beta h} = 1 \text{ ms}^{-1}; k_{\beta h} = -0.1 \text{ mV}^{-1}; d_{\beta h} = -35 \text{ mV}$$

The maximum conductance density for Na<sup>+</sup> channels in a given compartment was  $G_{\text{Na Max}} = 0.6 \text{ S.cm}^{-2}$  in the initial segment, and  $G_{\text{Na Max}} = 0.012 \text{ S.cm}^{-2}$  in other sections of the model. The equilibrium potential for Na<sup>+</sup> ions was set  $E_{\text{Na}} = +50 \text{ mV}$ .

**Potassium (K<sup>+</sup>) current** is computed as:

$$I_K = (E_K - E) \cdot G_K n^4$$

Its activation variable,  $n$ , is described by the equation:  $\frac{dn}{dt} = \alpha_n \cdot (1-n) - \beta_n \cdot n$

with rate functions  $\alpha_n$  and  $\beta_n$

$$\alpha_n = \frac{A_{\alpha_n} \times k_{\alpha_n} \times (E - d_{\alpha_n})}{1 - e^{-k_{\alpha_n} \times (E - d_{\alpha_n})}} \quad \beta_n = A_{\beta_n} \times e^{k_{\beta_n} \times (E - d_{\beta_n})}$$

In all computations, we used the following values for the K<sup>+</sup> channel parameters:

$$A_{cn} = 0.1 \text{ ms}^{-1}; k_{cn} = 0.1 \text{ mV}^{-1}; d_{cn} = -55 \text{ mV};$$

---

$$A_{\beta n} = 0.125 \text{ ms}^{-1}; k_{\beta n} = -0.0125 \text{ mV}^{-1}; d_{\beta n} = -65 \text{ mV}$$

The maximum conductance density was  $G_{K\text{Max}} = 0.19 \text{ S.cm}^{-2}$  in the initial segment, and  $0.0036 \text{ S.cm}^{-2}$  in the other sections of the model. The equilibrium potential for  $\text{K}^+$  ions was  $E_K = -77 \text{ mV}$ .

### **Statistics**

For the plasticity experiments, we expressed the values as normalized mean  $\pm$  standard error of mean. We performed a two-way repeated ANOVA, to test the effect of time, the interaction between groups and change over time, and the effect between groups. The homogeneity of variances for every timepoints was tested using a Levene test, for the timepoints that were not significant, a post-hoc Bonferroni test was performed otherwise we performed a post-hoc Dunnett test.

---

## RESULTS

### Quantitative analysis of axon morphology at the nanoscale

To visualize axonal projections in 3-5 weeks organotypic hippocampal slices, CA3 pyramidal neurons were locally infected using Sindbis virus expressing GFP (**Fig. 1a,b**). The Schaffer collateral projections were imaged in the CA1 *stratum radiatum* by STED microscopy. Our home-built STED microscope offers a spatial resolution in the focal plane of around 50 nm (**Fig. S1**), providing sufficient resolution to reliably quantify morphological parameters of thin unmyelinated axons that can be as small as 100 nm regarding previous electron microscopy studies<sup>5</sup>.

The images reveal irregular geometries of axon morphologies and high variability across axon segments (**Fig. 1c**). In order to comprehensively analyze axonal morphology, we measured both inter-varicosity shaft segment diameters and presynaptic boutons sizes. Axon shaft diameters were symmetrically distributed around a median of 203 nm, ranging from 70 to 420 nm ( $n = 26574$ , only values above 0.1% were represented, **Fig. 1d**), while median bouton size was  $0.53 \mu\text{m}^2$  ranging between  $0.2\text{--}2.2 \mu\text{m}^2$  ( $n = 319$ , **Fig. 1e**). The distributions of the morphological parameters appeared smooth and unimodal (**Fig. 1d,e**).

We observed slight dynamic changes in the axonal morphology, however the overall aspect of the structure is stable over the course of an hour (**Fig. 1g,h**). Both boutons size and shaft diameter did not undergo directional changes over time (Kruskall-Wallis test  $P_{\text{bouton}} > 0.40$ ,  $n=63$ ,  $P_{\text{shaft}} > 0.54$ ,  $n=113$  segments of  $1 \mu\text{m}$ ; **Fig. 1i-k**) indicating that the morphology of those structures are largely stable over periods of an hour and that repeated STED imaging did not induce visible photodamage.

---

## LTP induction leads to structural plasticity in axons

We investigated how CA3 axons morphology changes during LTP at CA3-CA1 synapses. We measured field excitatory postsynaptic potentials (fEPSPs) in the CA1 stratum radiatum after electrical high-frequency stimulation (HFS) in the CA3 pyramidal layer in order to maximize the overlap between stimulated and imaged axons (**Fig. 2a**). HFS led to a strong increase in fEPSP responses (potentiation at 30-40 minutes post-induction, 81%; **Fig. 2b**; average potentiation at 30-40 minutes post-induction,  $65 \pm 16\%$ ,  $n=8$ ,  $p<0.002$ ; **Fig. 2d**). At the same time, STED image stacks were acquired around every 12 minutes, with two reference stacks before the stimulation and four stacks after it.

The STED time lapse imaging series revealed a substantial increase in the diameter of CA3 axon concomitant with LTP induction (**Fig. 2c** with corresponding LTP recording **Fig. 2b**). The effect appears to be evenly expressed along axons and builds up over tens of minutes after LTP induction (at 45 minutes:  $5.0 \pm 0.8\%$ ; LTP:  $n=8$ ; **Fig. 2e**) leading to statistically significant differences between "before" and "after" stimulation groups ( $p<0.05$ ), as well as between stimulated and unstimulated conditions (control:  $n = 7$ ;  $p<0.05$ ).

Because LTP might not be evenly expressed throughout the CA1 stratum radiatum and that the imaging protocol limits us to relatively small fields of view, we sorted LTP experiments by the ones that showed in average the largest diameter increase over the ones that showed a minimal change (**Fig. 2f**). The average diameter increase for the experiments that showed the largest change is about 7% (at 45 minutes:  $6.9 \pm 0.6\%$ ;  $n=4$ ) which amounts to a 14% increase in axonal cross section over the control conditions.

In order to check whether the morphological effect induced by HFS depends on the expression of LTP, we repeated the experiments in the presence of an NMDA receptor

---

antagonist (50 $\mu$ M APV). Whereas the induction of LTP was completely abolished by bath application of the drug (**Fig. 2d**), the morphological effect on axon diameter was only visible at 45 minutes after HFS ( $3.6 \pm 1.6\%$ , n=6) (**Fig. 2f**). However, it appears to build up more slowly compared to without the drug.

We also compared the distributions of diameter changes for individual axon segments in an hour for the control condition and after LTP induction (**Fig. 2g**). This analysis reflects the important variability in diameter change in both control and LTP condition. It also further support the hypothesis that some of the axons did not experience the stimulation as a small fraction showed almost no change (fraction 0%;).

We analyzed the bouton morphology separately from the shaft segments. We observed a much more subtle increase of the bouton size during LTP and no significant difference in APV conditions (**Fig. 2h**).

Taken together, the combination of time lapse STED microscopy and electrophysiological experiments reveals that axons can undergo activity-dependent structural plasticity whereby electrical stimulation leads to nanoscale changes in axon diameter.

### **LTP leads to an increase of APs conduction velocity**

Knowing that AP conduction is largely predicted by morphological parameters, we investigated whether a change in AP velocity would corroborate the morphological data. We performed patch-clamp recordings from CA3 pyramidal neurons together with direct axonal stimulation in the CA1 *stratum radiatum*. We monitored simultaneously antidromic AP propagation latencies at the soma and fEPSP in the CA1 *stratum radiatum* during LTP induction (**Fig. 3a**). The current-clamp waveform following the electrical stimulation was characterized using drugs to discriminate AP generated by direct axonal stimulation and

---

synaptically evoked AP (**Supplementary Fig. 4a**). In addition, synaptic transmission was blocked by 2mM kynurenic acid (KYN) at the end of every recording to validate the experiment (**Supplementary Fig. 4b**).

Interestingly, we found a significant long-lasting reduction of APs latencies 20 minutes after LTP induction reflecting an increase of conduction velocity in the axonal compartment (**Fig. 3c,d** with corresponding LTP recording **Fig. 3b**). In average, we found that the AP latency was significantly reduced by  $2.2 \pm 0.77\%$  at 30-40 minutes after induction of LTP (n=10,  $P < 0.02$ , with an average potentiation at 30-40 minutes post-induction of  $81 \pm 22\%$ ,  $P < 0.006$ ) and this change was completely abolished when LTP was blocked (APV, n=8, at 30-40 minutes post-induction: average decrease of latency of  $0.12 \pm 0.42\%$ ,  $p > 0.78$ ; average potentiation of  $11 \pm 9\%$ ,  $p > 0.26$ ) (**Fig. 3e-g**).

### **LTP induction increases boutons**

In order to know if morphological changes of the axon geometry could explain the initial slow down of conduction velocity, we imaged CA3 axons right after HFS. Interestingly, we observed that 2 minutes after HFS, boutons undergo an increase in size by  $20 \pm 2.5\%$  (n=148, from 4 experiments;  $p < 0.05$ ) while the axon shaft diameter increases by  $2.3 \pm 1.4\%$  (n=148,  $p > 0.05$ ; **Fig. 4a-c**). This rapid change appears to be transient as the 8 minutes after the stimulation, the size of the bouton partially decreases ( $9.8 \pm 2.7\%$ , n=148,  $p < 0.05$ ) while the axon shaft diameter keeps increasing by  $3.8 \pm 1.5\%$  (n=148,  $p < 0.05$ ; **Fig. 4b,c**). In addition, by plotting the relative change of bouton size with the measured adjacent shaft diameter, we show that the irregularity of the axon structure is much greater 2 minutes after the stimulation compared to after 8 minutes (**Fig. 4d**).

---

These results indicate that HFS transiently increases irregularity of the axon structure could be the cause for the initial slow down in conduction velocity observed previously.

### **Axon structural plasticity correlates with changes in AP propagation delays during LTP**

While basic biophysical principles explain directional changes of geometry and AP conduction velocity, we investigated their correlation based on realistic model simulations. In the model used, we tested different axon stretch geometry based on real morphological data (**Fig. 5a**). We found a high correlation between AP conduction velocity and the square-root of the average axon shaft tested ( $r^2 = 0.94$ ) (**Fig. 5b**). We also tested the impact of the degree of irregularity generated by the average increase of boutons size on an axon segment (**Fig. 5c** and **Supplementary Fig. 6**). The increase by 10 and 20% of the bouton size increases the delay of propagation hence decreases the conduction velocity. The changes in conduction velocity calculated from the AP latency recordings correlates well with the simulation based on the morphological changes after HFS and during the establishment of LTP (**Fig. 5d**).

## DISCUSSION

Our experimental approach based on a combination of STED microscopy (with a spatial resolution of around 50 nm) and electrophysiology in living brain slices made it possible to visualize nanoscale changes in axon morphology and to carry out electrophysiological experiments to induce synaptic plasticity and to assess the impact on AP propagation.

We obtained direct evidence that axons become wider and propagate APs faster after the induction of LTP. Both the morphological and functional effects were rapidly expressed and persisted for at least an hour, suggesting a novel form of neural plasticity, which may have important implications for temporal coding in neural circuits of the mammalian brain.

### **Morphological dynamics of axons in living brain slices**

Hyperthin unmyelinated axons are an anatomical hallmark of the hippocampus, with shaft diameters oftentimes narrower than 200 nm<sup>5</sup>. As conventional light microscopy does not provide sufficient spatial resolution for accurate measurements on this spatial scale, very little is known about the morphological dynamics of axon shafts, let alone its regulation by neuronal activity or its effects on AP propagation.

By contrast, the morphological dynamics of presynaptic boutons, which are much larger than axon shafts, have been studied before by two-photon microscopy, revealing that they undergo a modest amount of structural remodelling under baseline conditions, but significantly reduce their contacts with dendritic spines after the induction of long-term depression (LTD) at hippocampal synapses<sup>9, 10</sup>.

---

## Coordinated changes in axon morphology and function

Consistent with the previous work, we observed very little structural remodelling of presynaptic boutons and axon shafts under baseline conditions. However, the induction of LTP led to clear-cut bouton enlargement and shaft widening, which were detectable within minutes and persisted for more than one hour after stimulation. The time-lapse data indicate that the structural changes followed a differential time course, where the boutons swelled up transiently before the shafts became wider.

Importantly, these changes would be entirely invisible to conventional light microscopy, because they were on the order of tens of nanometers, necessitating the use of superresolution microscopy.

LTP induction also led to clear changes in AP propagation delay, which at first increased, and then decreased to significantly below baseline levels for the remainder of the experiment. These findings confirm and extend previous reports on changes in synaptic latency after LTP induction. However, these changes were attributed to activation of silent synapses<sup>21</sup> or to changes in presynaptic release probability<sup>7</sup>. In contrast, our experiments provide direct evidence for a drop in AP propagation delay after LTP, which is consistent with a study in cultured neurons using multi-electrode arrays<sup>8</sup>.

The changes in shaft diameter and AP propagation delay after LTP correspond well with cable theory that predicts that the speed of AP conduction in unmyelinated axons depends on the square root of axon diameter<sup>22</sup>, indicating that the decreased AP propagation delays reflect a widening of axon shafts that accelerates AP conduction, as opposed to axon excitability changes independent of any structural effects. Moreover, the model simulations, which were based on accurate morphological reconstructions using the STED data, also

---

corroborate the conclusion that AP conduction velocity is increased after LTP. Interestingly, the model predicted the increase in AP propagation delay from the transient swelling of the boutons after LTP induction.

### **Potential mechanisms of axon widening**

The increase in axon diameter after LTP implies a gain in surface area of the axon, which must be sourced either by *de novo* membrane synthesis or redistribution of existing membrane pools. A local redistribution of membranes cannot account for the net gain, because the effect was globally expressed and affected the average diameter. Moreover, according to membrane biophysics, stretching or unfolding of axon membranes can also be ruled out as mechanisms, because lipid bilayers are unlikely to be elastic enough or to behave like an accordion.

Alternatively, a substantial increase in surface membrane could derive from the exocytosis of presynaptic vesicles due to the intense electrical stimulation of the axons during the induction of LTP. The estimated size of the total membrane added by the release of synaptic vesicles, based on the net loss of vesicles seen ultrastructurally after LTP<sup>23</sup>, could in fact readily account for the increase in bouton size and axon diameter. The differential time course we observed for the structural changes suggests a scenario where the addition of the membrane of the vesicles first drives an expansion of the boutons, which then diffuses laterally to cause widening of the adjacent axon shafts, providing a plausible cell biological mechanism, which is both rapid and metabolically cost-efficient. However, the partial blockade of the morphological effects by APV experiments argue somewhat against this model, because *a priori* APV should not affect the release of synaptic vesicles during LTP induction.

---

### Functional implications for neural timing

The changes in AP propagation delay during LTP were recorded over relatively short distances, and hence amounted to just a couple of hundreds of microseconds. However, if axon widening affects AP conduction uniformly along the axon, the reduction of AP propagation delay should scale with the length of the axons. Given that CA3 axons can be as long as 20 mm *in vivo* in rats<sup>24</sup>, the AP propagation delay for distal synapses would build up to several tens of milliseconds, which would be expected to strongly impact synaptic integration in the postsynaptic neurons.

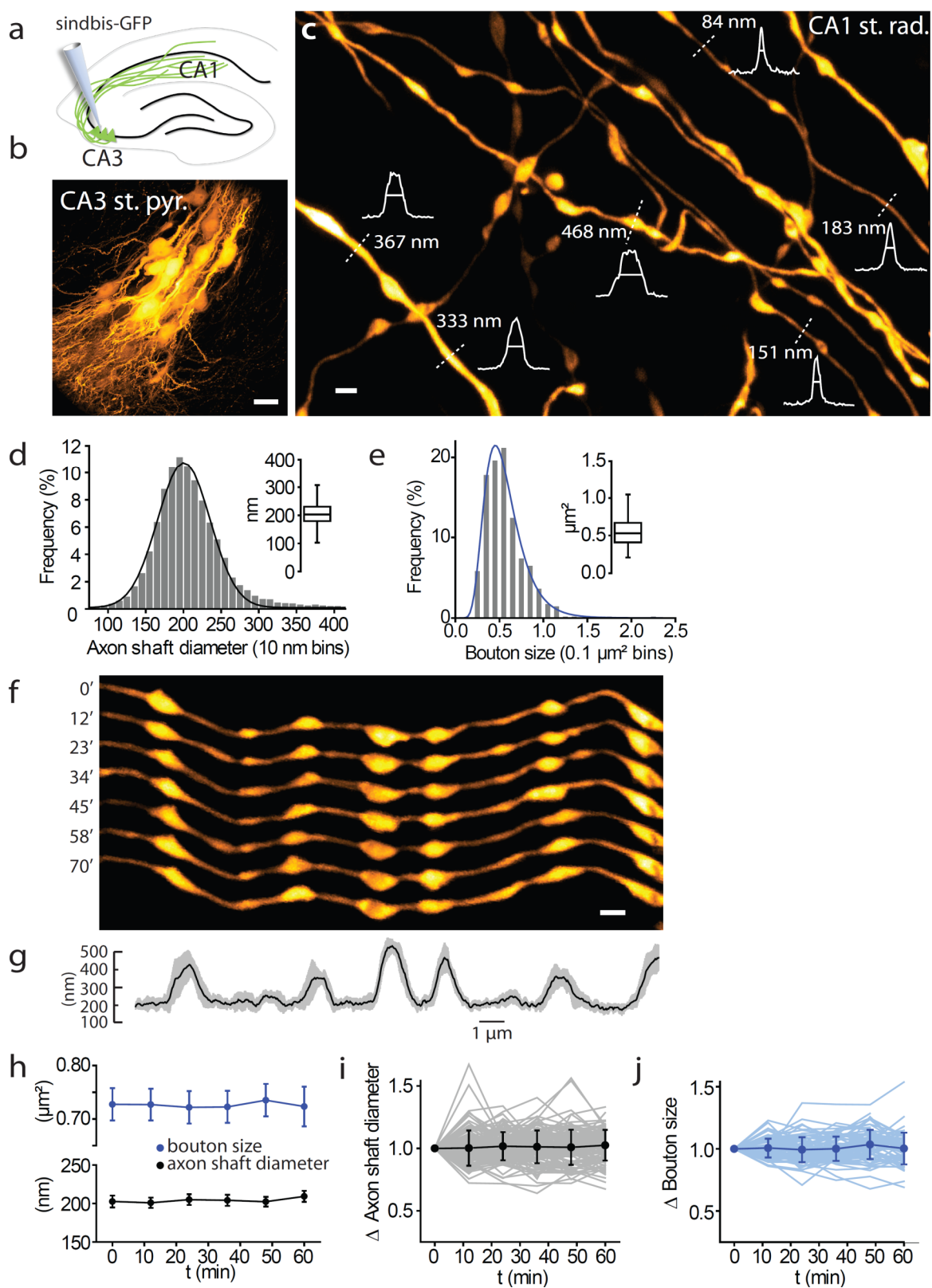
What is the functional significance of variations in axonal delays for network performance? Propagation delays could be important in the context of spike-timing dependent plasticity (STDP). The time window for supralinear summation of calcium caused by dendritic spikes and synaptic events is on the milliseconds scale and determines whether synapses get potentiated or depressed. Given that STDP might be responsible for the formation of synchronized groups of neurons that are strongly interconnected, slight variations in propagation delays could remodel those poly-synchronous groups<sup>25</sup>. Variations in delay at excitatory synapses may also produce substantial changes in the temporal integration by changing the balance during di-synaptic inhibition and therefore may change the output properties.

Several studies have indicated that CA3 axons, known to branch extensively<sup>24, 26</sup> do not propagate APs reliably throughout their complex arbor and might exhibit failures at branch points under certain conditions<sup>27-29</sup>. The enlargement of axon shafts may affect the reliability of AP propagation by altering the impedance mismatch at branch points.

Finally, the concept whereby axons act as dynamic delay lines for information transfer has been debated for a long time. In the auditory system, the interaural time difference to achieve coincidence detection in sound localisation requires sub-millisecond precision and was thought to rely on axon length<sup>30</sup> (i.e. Jeffress model<sup>31</sup>). But recent findings showed that the topological organization of delays were poorly correlated with axon length and demonstrated that axon diameters and distances between nodes of Ranvier were mechanisms for adjusting interaural delay differences<sup>32</sup>.

In summary, our study amends the classic view of structural plasticity as primarily reflecting a change in synaptic strength by demonstrating structural changes that dynamically regulate the speed of AP conduction and hence are likely to substantially impact the timing of information transfer in neural circuits.

Figure 1



---

**Figure 1 Heterogeneity and dynamics of CA3 axons**

(a-c) Viral injection of Sindbis-GFP in the CA3 pyramidal layer yielded a sparse set of brightly labeled axons whose hyperthin morphology could be readily imaged by STED microscopy. (a) Schematic of the viral injection approach. (b) Confocal image of the CA3 pyramidal layer approximately 36 hours post-injection showing a compact subset of labeled neurons (scale bar, 20  $\mu\text{m}$ ). (c) STED images of axons in the *stratum radiatum*. The image is a maximum-intensity projection of eight z-planes 375 nm apart (raw images in Supplementary Figure 1). Intensity profiles of axons shafts and boutons (white); full-width half maximums (FWHMs) indicate axon diameters (scale bar, 1  $\mu\text{m}$ ).

(d-e) Distribution of morphological parameters of axons. (d) Distribution of axon diameters (n=26574). Curved line is a Gaussian fit, where  $R^2=0.99$ . The inset shows median diameter; 203 nm, interquartile and range. (e) Distribution of bouton size (n=319). Curved line is a log-normal fit, where  $R^2=0.98$ . The inset shows median size; 0.53  $\mu\text{m}^2$ , interquartile and range.

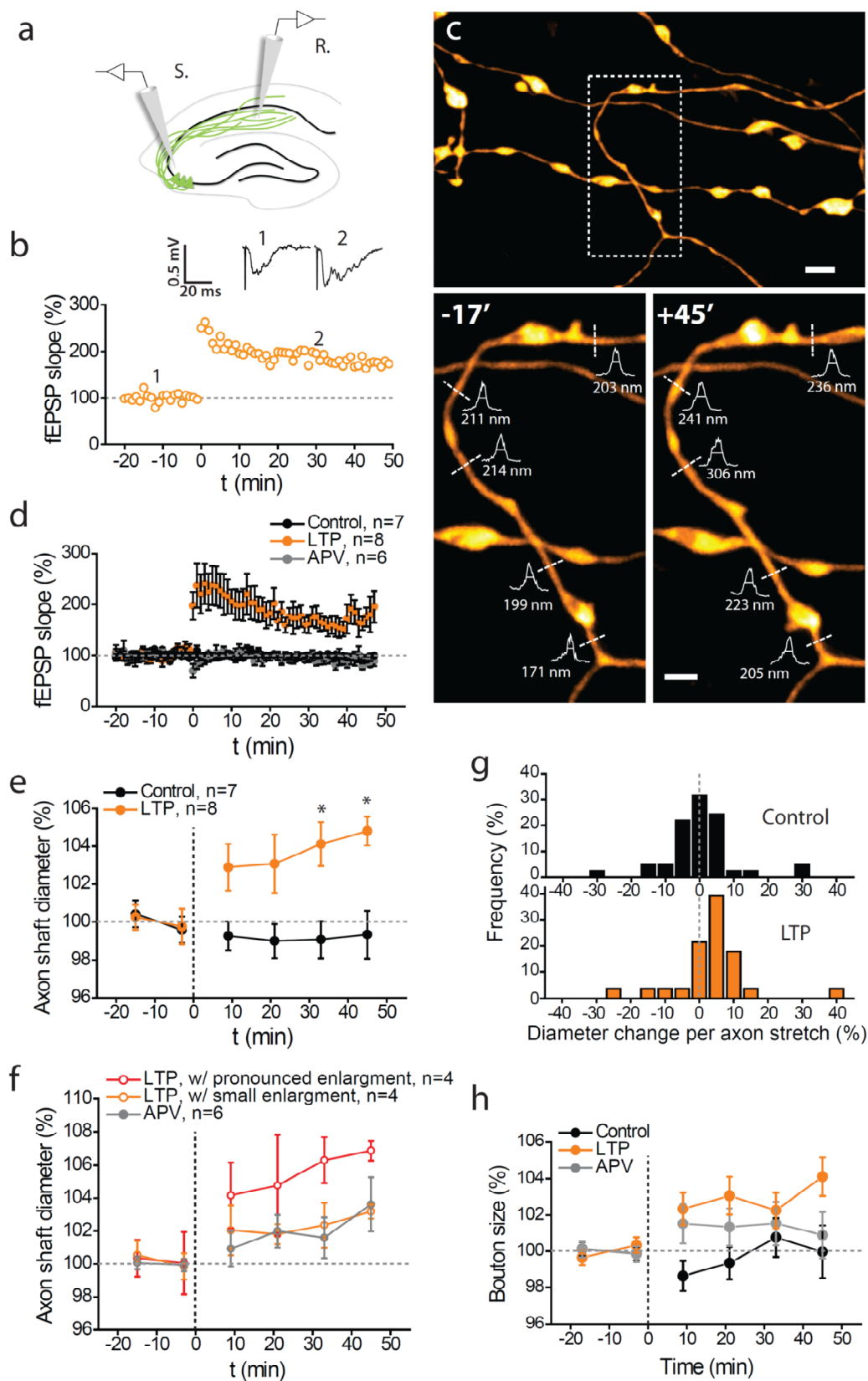
(f) Example of an axon segment imaged over more than an hour (scale bar, 1  $\mu\text{m}$ )

(g) Diameter profile of the axon shown in (f). The average diameter in time is represented (black line) with SD (grey).

(h) Time-lapse imaging over 1 hour (geometric mean with 95% CI) for boutons (n=85) and 1  $\mu\text{m}$  axon shaft segments (n=113).

(i-j) Standard deviation of the normalized changes over 1 hour.

Figure 2



---

**Figure 2 Structural plasticity of axon shafts and boutons during LTP**

(a) Recording configuration (S.: stimulating electrode; R.: recording electrode). The GFP labeled neurons were imaged in the CA1 stratum radiatum.

(b-c) Example of morphological change observed during LTP. (b) Normalized fEPSP slope recordings during baseline and LTP induction. The inset shows representative fEPSP traces before (1) and after induction of LTP (2). (c) STED images showing morphological changes before and after LTP induction. Top: overview; Bottom: magnified view corresponding to the region on the left image (Intensity profiles and FWHMs reported on the images illustrate the increase of axon shaft diameter after LTP induction).

(d) Average time course of the fEPSP slope (normalized to baseline) during LTP induction (orange; average potentiation at 30-40 minutes post-induction  $65 \pm 16\%$  of baseline,  $n=8$ ,  $p<0.002$ ). LTP was not induced in the presence of the NMDA receptor blocker APV (grey,  $n=6$ ,  $p>0.58$ ). The recordings were stable in control conditions (black,  $n=7$ ,  $p>0.18$ ); mean  $\pm$  SEM shown.

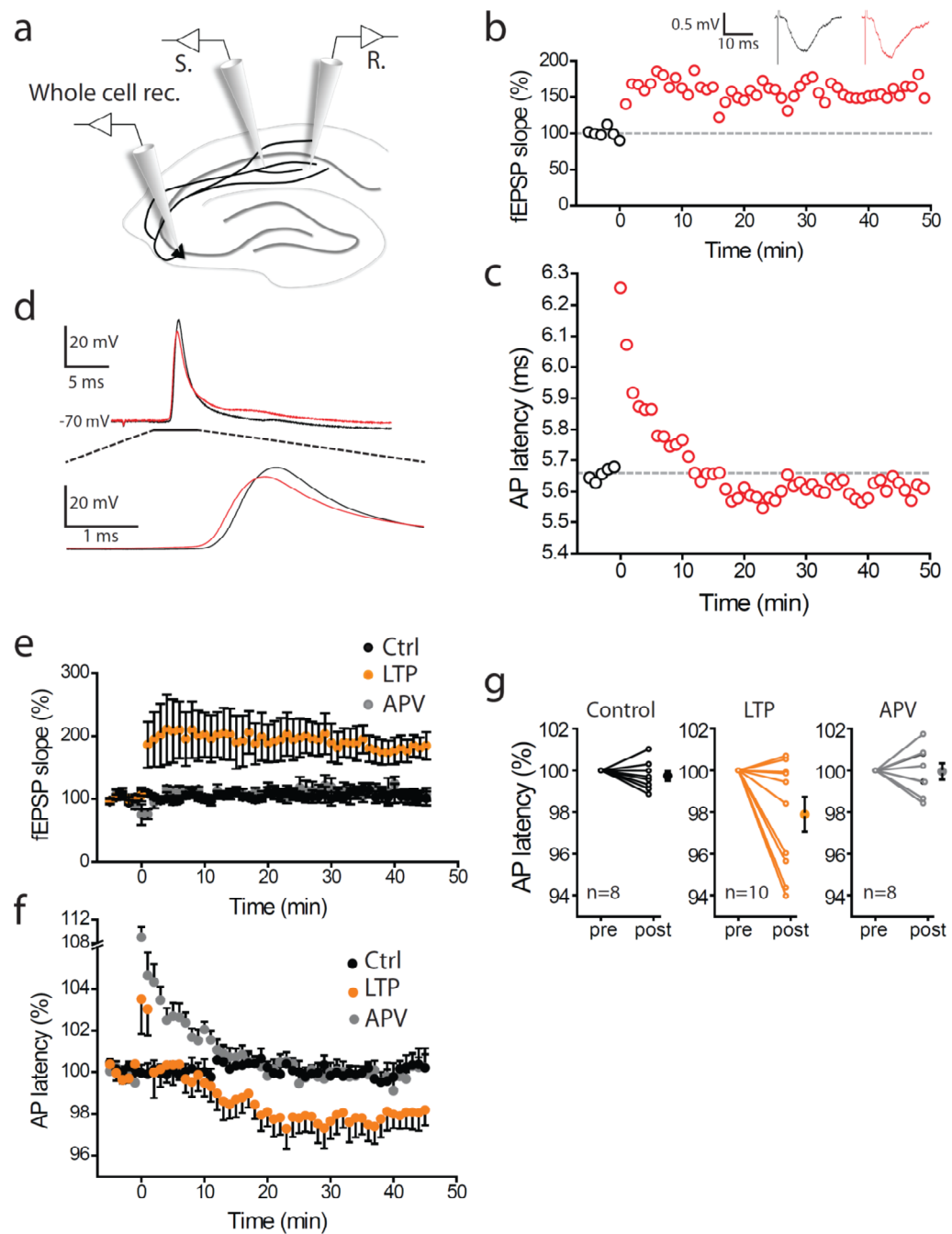
(e) Normalized axon shaft diameter during LTP (orange) shows a sustained increase over the course of 45 minutes after induction (orange,  $n=8$ ) over the control condition (black,  $n=7$ ).

(f) Normalized axon shaft diameter for LTP experiments that showed the most pronounced enlargement (red,  $n=4$ ) compared to experiments that showed a smaller enlargement ( $n=4$ ) and when LTP was blocked with APV ( $n=6$ ).

(g) Frequency distribution of average diameter change per axon stretch at +45 minutes compared to -15 minutes for control and LTP experiments (all experiments pulled).

(h) Normalized bouton size for the three groups (Control,  $n=7$ ; LTP, orange,  $n=8$ ; APV, grey,  $n=6$ )

Figure 3



---

**Figure 3 LTP induction leads to changes in AP propagation delay**

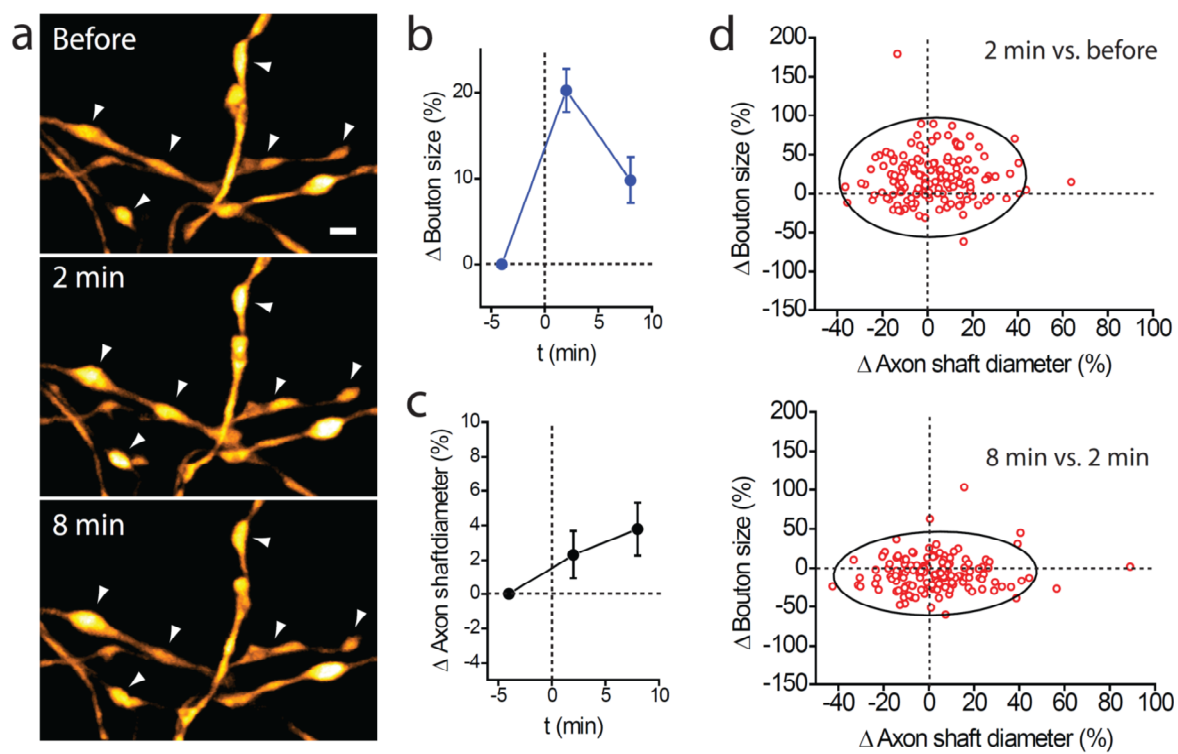
(a) Recording configuration of antidromic AP latencies of CA3 pyramidal neurons (Whole cell rec.: whole-cell recording; S.: stimulating electrode; R.: recording electrode).

(b-d) Example of reduction of antidromic latency during LTP. (b) Normalized fEPSP slope recordings during baseline (black circles) and LTP induction (red circles). The inset shows representative fEPSP traces before (black) and after induction of LTP (red). (c) AP latency recordings measured as the onset of AP waveforms at the soma during the course of LTP was stable during baseline (black) typically increases and recovers over few minutes and show a stable latency reduction from 20 minutes after induction (red). (d) Representative waveforms recorded at the soma following direct axonal stimulation before (black) and after induction of LTP (red).

(e) Average time course of the fEPSP slope (normalized to baseline) during LTP induction (orange; average potentiation at 30-40 minutes post-induction  $81 \pm 22\%$  of baseline,  $n=10$ ,  $p < 0.02$ ). LTP was not induced in the presence of APV (grey,  $n=8$ ). The recordings were stable in control conditions (black,  $n=8$ ); mean  $\pm$  SEM shown.

(f) Average AP latency recordings for the three groups

Figure 4



---

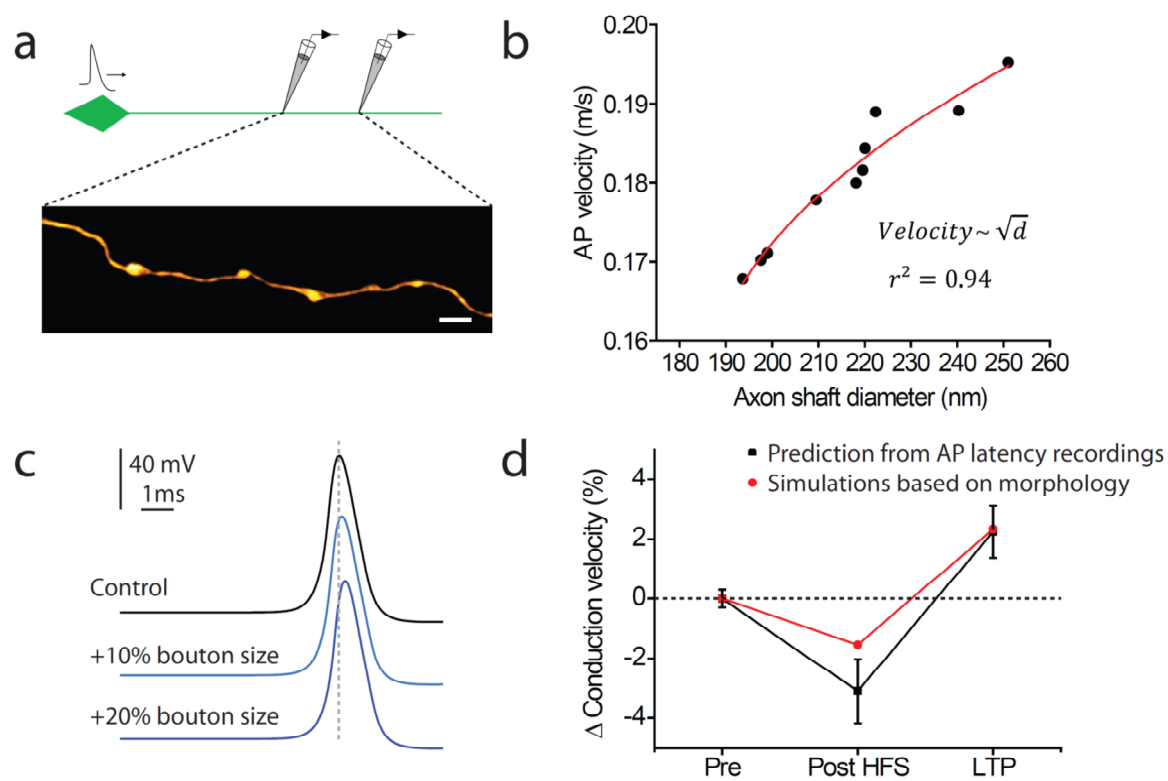
**Figure 4 LTP induction increases presynaptic boutons**

(a) Effect of HFS on the axonal structure. STED images showing the enlargement of boutons identified by the arrowheads, 2 and 8 minutes after HFS.

(b-c) Normalized change in bouton size (b) and axon shaft diameter (c) following HFS. Error bars, SEM.

(d) Normalized bouton size change plotted against normalized axon shaft diameter showing the relative change between 2 minutes versus before (top) and 8 min versus 2 minutes after the stimulation.

Figure 5



---

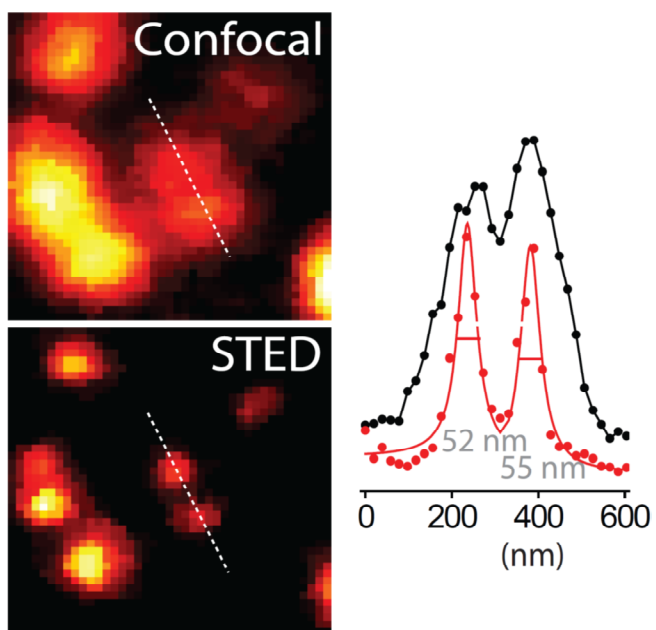
**Figure 5 Biophysical modeling of impact of axon structural plasticity on AP propagation**

(a-b) Conduction velocities were determined based on simulated AP propagation through real morphological data extracted from STED images (a). Ten axon segments were tested for conduction velocity and plotted against their axon shaft diameters (b). The conduction velocity is proportional to the square-root of the axon diameter ( $R^2=0.94$ ).

(c) A ball and stick model was used to simulate the increase of bouton size during HFS. The shaft diameter used was 200nm and bouton dimensions were 0.5 $\mu$ m width, 1 $\mu$ m long with an oblong shape. Data illustrate longer delays of propagation when the average bouton size is larger.

(d) Comparison between the conduction velocity based on predictions from AP latency recordings and simulations based on the morphology.

Figure S1



---

**Figure S1** Resolution improvement of STED microscopy over confocal microscopy.

Imaging 40 nm fluorescent beads reveals a substantial gain in spatial resolution by STED over confocal microscopy. Intensity profiles corresponding to the dotted lines in the images are depicted in the graph (raw data, dots). The FWHM from Lorentzian fits on the STED intensity profiles (red line) illustrate the gain in resolution whereas in confocal mode it was not possible to discriminate the two beads (black line).

Figure S2

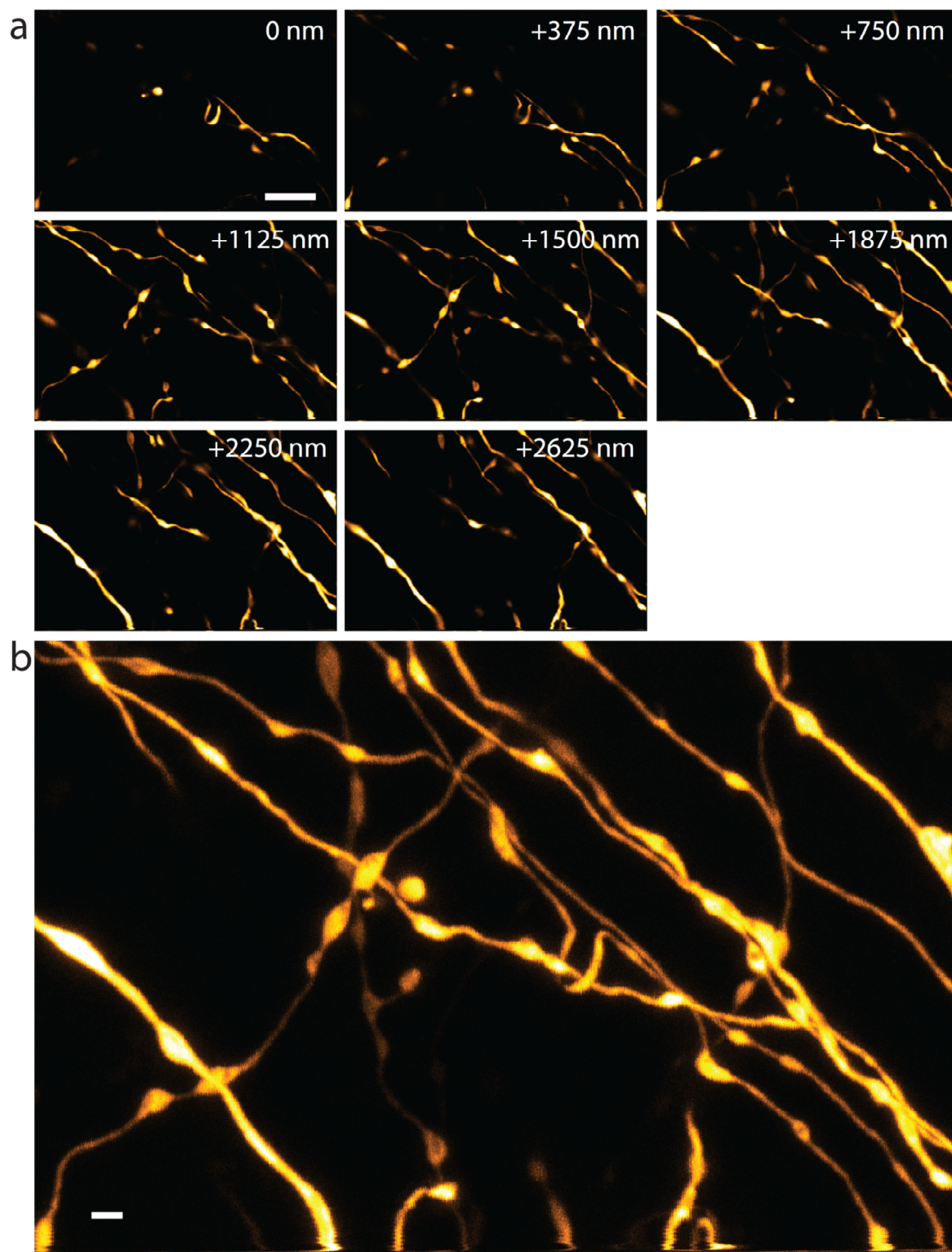
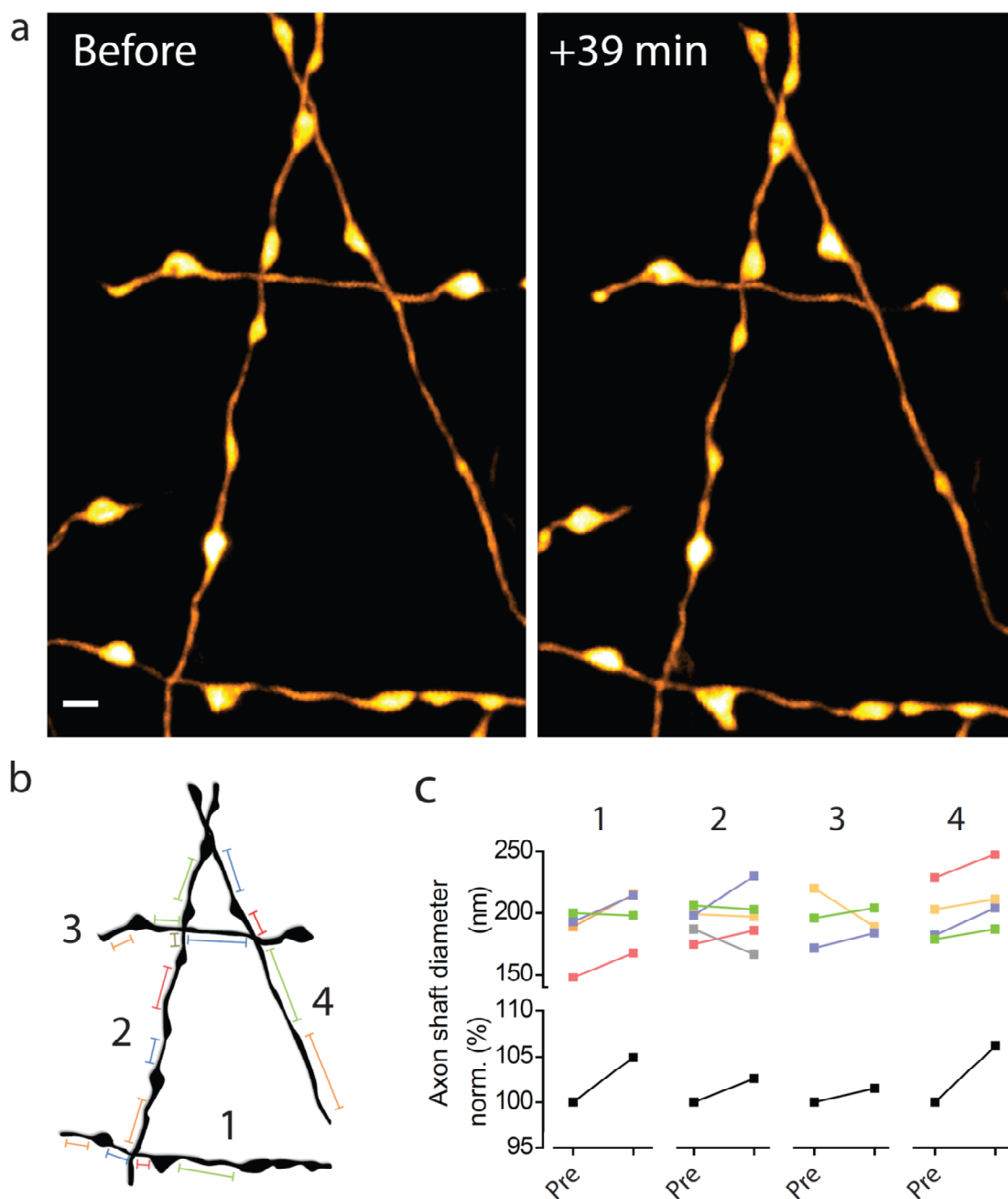


**Figure S2** Raw data of the maximum intensity projection image shown in Figure 1.

(a) The image z-stack depicted as a maximum intensity projection in Fig. 1c, covering 8 sections 375 nm apart. All sections shown are raw images (scale bar, 5  $\mu\text{m}$ ).

(b) The maximum intensity projection of the raw image sections (scale bar, 1  $\mu\text{m}$ ).

Figure S3



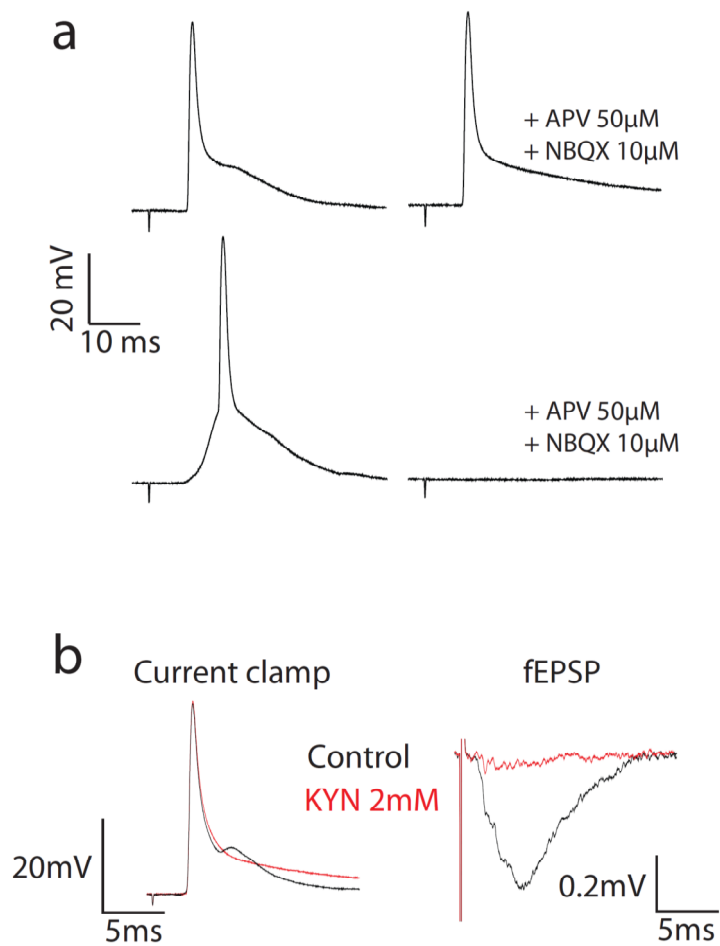
---

**Figure S3** Example of axon shaft diameter increase after LTP induction

(a) STED images of the same axon segments before and after induction of LTP showing slight enlargements of axon diameters between boutons (scale bar, 1  $\mu\text{m}$ ).

(b-c) Comparison between the average inter-bouton diameters from the four axon segments shown in A before and after LTP. (c) Most of the axon shaft regions increase in diameter during LTP. Every segment is color-coded from the schematic in (b) (top part of the plot). Normalized and average change in axon diameters for the four axon segments (bottom of the plot).

Figure S4



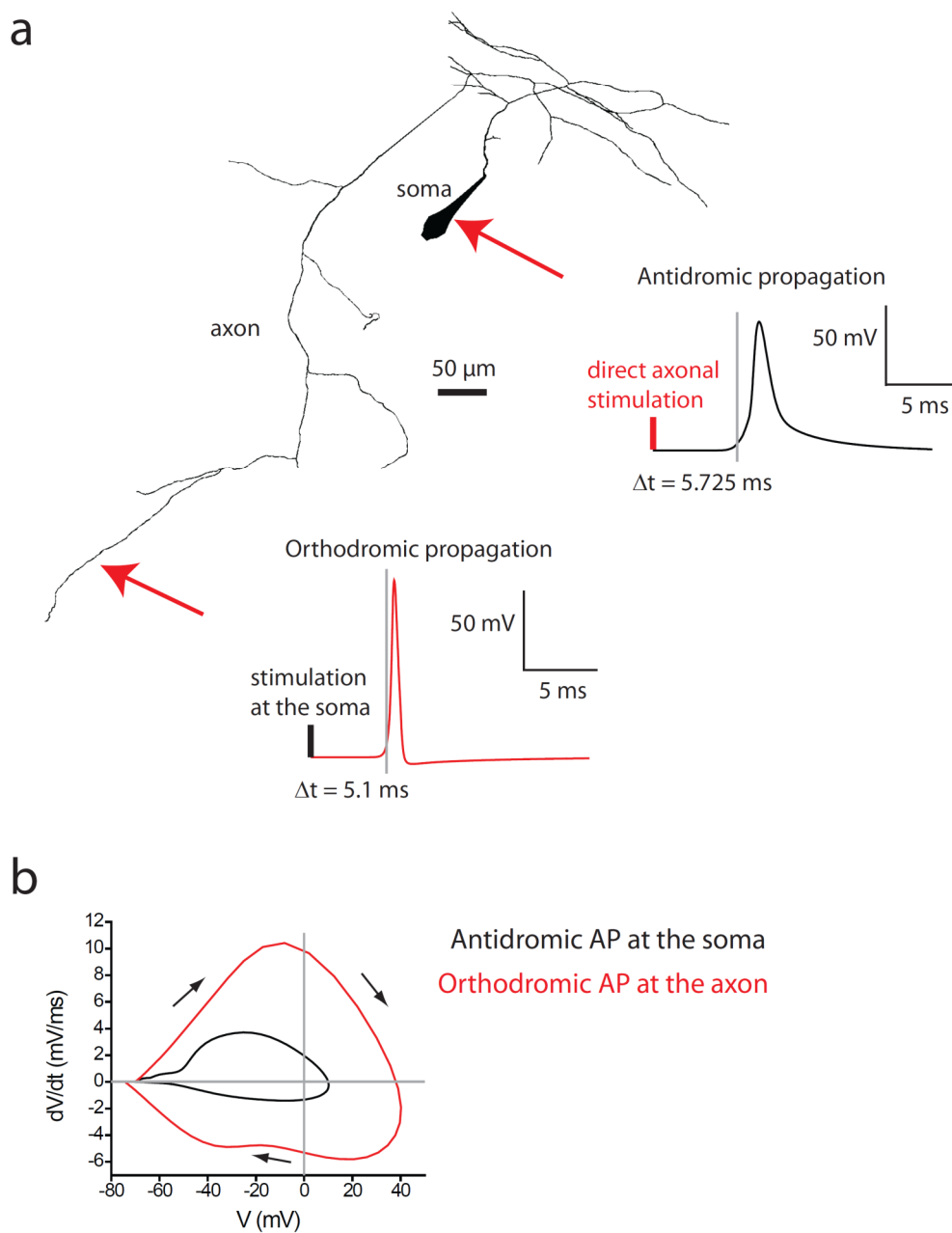
---

**Figure S4** Electrophysiological approach to measure axonal propagation delays of APs.

(a) Comparison between waveforms from direct axonal stimulation and synaptically-evoked AP. Typical AP waveform from direct axonal stimulation shows a sharp rising depolarization phase and a depolarization phase combined with an EPSP. A synaptically-evoked AP consists of an initial slow rising phase corresponding to the EPSP and generation of a somatic AP when the potential reaches the threshold. The blockade of glutamatergic synaptic transmission with APV and NBQX vanishes the synaptically-evoked AP where axonal AP remains.

(b) Blocking glutamatergic transmission with 2 mM kynurenic acid (KYN) vanishes the fEPSP while the AP waveform recorded at the soma remains, confirming that the AP is generated from direct axonal stimulation.

Figure S5



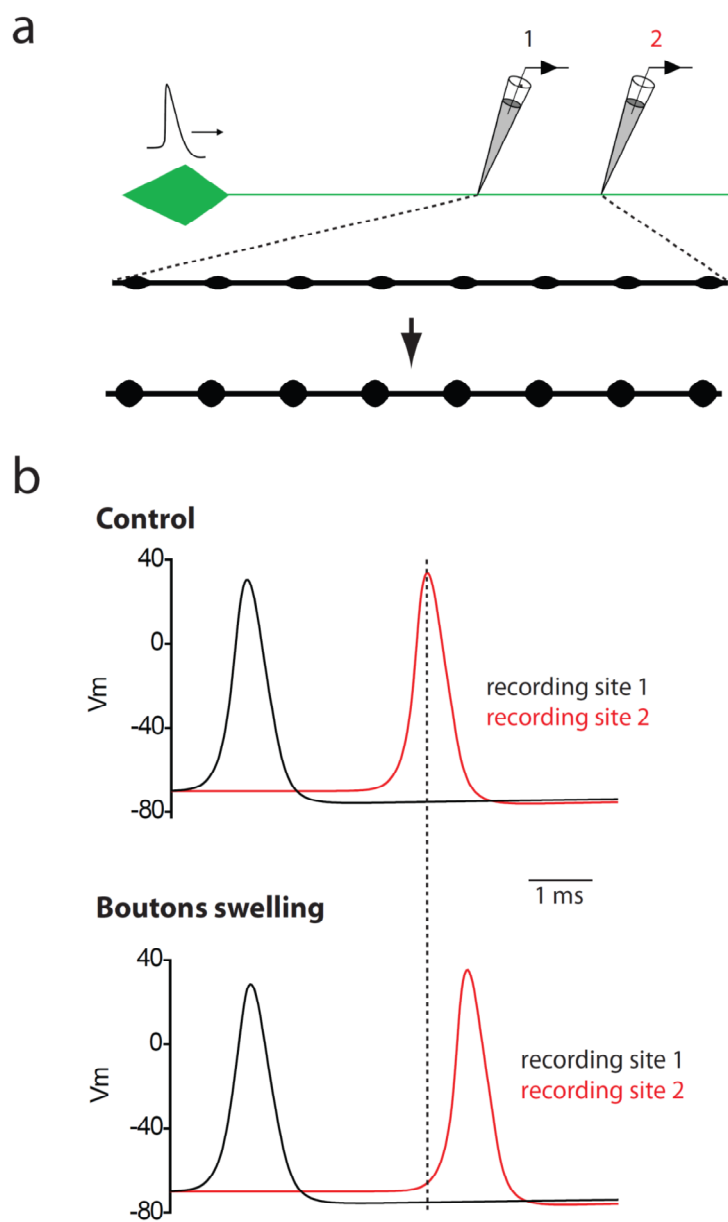
---

**Figure S5** Velocity comparison between orthodromic and antidromic AP propagation.

(a) The reconstruction of the proximal axon arborization of a CA3 pyramidal neuron was used for this simulation. An antidromic AP generated in the distal axon and recorded at the soma was compared with an orthodromic AP generated at the soma and recorded at the axon (red arrows stimulation and recording sites in both conditions). The antidromic propagation is slower with a latency of 5.725 ms (conduction velocity, 0.15 m/s) compared to orthodromic propagation (5.1 ms, conduction velocity, 0.17 m/s).

(b) Phase plot analysis of the antidromic and orthodromic AP waveforms shows large differences in terms of width and amplitude.

Figure S6



---

**Figure S6** Boutons swelling slow down conduction velocity.

(a) Schematic of a simplified “balls and sticks” model used for the simulation. A 1mm long sequence was tested (only samples of the sequence is represented) with a fixed axon shaft diameter of 200 nm and boutons of 3  $\mu\text{m}$  periodicity and of dimensions 1  $\mu\text{m}$  long and 500 nm width in control and 1  $\mu\text{m}$  width after swelling.

(b) AP recordings from the beginning (1) and the end (2) of the sequences in control (top) and after boutons swelling (bottom) tested. The traces show the reduction in conduction velocity (around 18%) for the large boutons (control: 0.175 m/s; boutons swelling condition: 0.144 m/s).

---

**REFERENCES**

1. Miles, R. Synaptic excitation of inhibitory cells by single CA3 hippocampal pyramidal cells of the guinea-pig in vitro. *J Physiol* **428**, 61-77 (1990).
2. Debanne, D., Gähwiler, B.H. & Thompson, S.M. Asynchronous pre- and postsynaptic activity induces associative long-term depression in area CA1 of the rat hippocampus in vitro. *Proc Natl Acad Sci U S A* **91**, 1148-1152 (1994).
3. Markram, H., Lubke, J., Frotscher, M. & Sakmann, B. Regulation of synaptic efficacy by coincidence of postsynaptic APs and EPSPs. *Science* **275**, 213-215 (1997).
4. Soleng, A.F., Raastad, M. & Andersen, P. Conduction latency along CA3 hippocampal axons from rat. *Hippocampus* **13**, 953-961 (2003).
5. Shepherd, G.M. & Harris, K.M. Three-dimensional structure and composition of CA3->CA1 axons in rat hippocampal slices: implications for presynaptic connectivity and compartmentalization. *J Neurosci* **18**, 8300-8310 (1998).
6. Meeks, J.P., Jiang, X. & Mennerick, S. Action potential fidelity during normal and epileptiform activity in paired soma-axon recordings from rat hippocampus. *J Physiol* **566**, 425-441 (2005).
7. Boudkazi, S., *et al.* Release-dependent variations in synaptic latency: a putative code for short- and long-term synaptic dynamics. *Neuron* **56**, 1048-1060 (2007).
8. Bakkum, D.J., Chao, Z.C. & Potter, S.M. Long-term activity-dependent plasticity of action potential propagation delay and amplitude in cortical networks. *PLoS One* **3**, e2088 (2008).
9. Bastrikova, N., Gardner, G.A., Reece, J.M., Jeromin, A. & Dudek, S.M. Synapse elimination accompanies functional plasticity in hippocampal neurons. *Proc Natl Acad Sci U S A* **105**, 3123-3127 (2008).
10. Becker, N., Wierenga, C.J., Fonseca, R., Bonhoeffer, T. & Nagerl, U.V. LTD induction causes morphological changes of presynaptic boutons and reduces their contacts with spines. *Neuron* **60**, 590-597 (2008).
11. Bethge, P., Chereau, R., Avignone, E., Marsicano, G. & Nagerl, U.V. Two-photon excitation STED microscopy in two colors in acute brain slices. *Biophys J* **104**, 778-785 (2013).
12. Nagerl, U.V., Willig, K.I., Hein, B., Hell, S.W. & Bonhoeffer, T. Live-cell imaging of dendritic spines by STED microscopy. *Proc Natl Acad Sci U S A* **105**, 18982-18987 (2008).
13. Gähwiler, B.H. Organotypic slice cultures: a model for interdisciplinary studies. *Prog Clin Biol Res* **253**, 13-18 (1987).
14. Gähwiler, B.H., Capogna, M., Debanne, D., McKinney, R.A. & Thompson, S.M. Organotypic slice cultures: a technique has come of age. *Trends Neurosci* **20**, 471-477 (1997).
15. Ehrenguber, M.U., *et al.* Recombinant Semliki Forest virus and Sindbis virus efficiently infect neurons in hippocampal slice cultures. *Proc Natl Acad Sci U S A* **96**, 7041-7046 (1999).
16. Jeromin, A., Yuan, L.L., Frick, A., Pfaffinger, P. & Johnston, D. A modified Sindbis vector for prolonged gene expression in neurons. *J Neurophysiol* **90**, 2741-2745 (2003).
17. IMSpector. [www.max-planck-innovation.de/de/industrie/technologieangebote/software/](http://www.max-planck-innovation.de/de/industrie/technologieangebote/software/).
18. Carnevale, N.T. & Hines, M.L. eds. *The NEURON Book* (Cambridge, UK: Cambridge University Press, 2006).

19. Hodgkin, A.L. & Huxley, A.F. Propagation of electrical signals along giant nerve fibers. *Proc R Soc Lond B Biol Sci* **140**, 177-183 (1952).
20. Hodgkin, A.L. & Huxley, A.F. A quantitative description of membrane current and its application to conduction and excitation in nerve. *J Physiol* **117**, 500-544 (1952).
21. Voronin, L.L., Volgushev, M., Chistiakova, M., Kuhnt, U. & Singer, W. Involvement of silent synapses in the induction of long-term potentiation and long-term depression in neocortical and hippocampal neurons. *Neuroscience* **74**, 323-330 (1996).
22. Goldstein, S.S. & Rall, W. Changes of action potential shape and velocity for changing core conductor geometry. *Biophys J* **14**, 731-757 (1974).
23. Bourne, J.N., Chirillo, M.A. & Harris, K.M. Presynaptic ultrastructural plasticity along CA3-->CA1 axons during long-term potentiation in mature hippocampus. *J Comp Neurol* **521**, 3898-3912 (2013).
24. Wittner, L., Henze, D.A., Zaborszky, L. & Buzsaki, G. Three-dimensional reconstruction of the axon arbor of a CA3 pyramidal cell recorded and filled in vivo. *Brain Struct Funct* **212**, 75-83 (2007).
25. Izhikevich, E.M. Polychronization: computation with spikes. *Neural Comput* **18**, 245-282 (2006).
26. Major, G., Larkman, A.U., Jonas, P., Sakmann, B. & Jack, J.J. Detailed passive cable models of whole-cell recorded CA3 pyramidal neurons in rat hippocampal slices. *J Neurosci* **14**, 4613-4638 (1994).
27. Debanne, D., Guerineau, N.C., Gahwiler, B.H. & Thompson, S.M. Action-potential propagation gated by an axonal I(A)-like K<sup>+</sup> conductance in hippocampus. *Nature* **389**, 286-289 (1997).
28. Soleng, A.F., Chiu, K. & Raastad, M. Unmyelinated axons in the rat hippocampus hyperpolarize and activate an H current when spike frequency exceeds 1 Hz. *J Physiol* **552**, 459-470 (2003).
29. Meeks, J.P. & Mennerick, S. Selective effects of potassium elevations on glutamate signaling and action potential conduction in hippocampus. *J Neurosci* **24**, 197-206 (2004).
30. Vonderschen, K. & Wagner, H. Detecting interaural time differences and remodeling their representation. *Trends Neurosci* **37**, 289-300 (2014).
31. Jeffress, L.A. A place theory of sound localization. *J Comp Physiol Psychol* **41**, 35-39 (1948).
32. Seidl, A.H., Rubel, E.W. & Harris, D.M. Mechanisms for adjusting interaural time differences to achieve binaural coincidence detection. *J Neurosci* **30**, 70-80 (2010).

## **Part 2: Development of two-photon excitation STED microscopy in two colors in acute brain slices**

### **Aim of the study:**

To understand how neural cells shape and react in physiological and pathological conditions, it is necessary to observe them in the most intact preparation. STED microscopy enables for observing nanoscale dynamics of cellular morphology and organelles where conventional light microscopy failed to resolve them. However, the first developments of STED microscopy were based on single photon excitation thus limiting observations to superficial structures in dissociated cultures and organotypic brain slices. On the other hand, two-photon microscopy is currently the method of choice for imaging in thick living tissue preparations, both in acute brain slices and *in vivo*. As a conventional light microscopy method, the spatial resolution of a two-photon microscope is limited to ~350 nm by the diffraction of light, hence missing important structural details like spine and axon morphological features.

We aimed to develop a 2-photon excitation STED depletion microscope providing unprecedented spatial resolution and excellent experimental access in acute brain slices.

### **Results:**

We built a new microscope based on two-photon excitation and pulsed stimulated depletion. Its versatility allows for imaging the classical green fluorophores such as GFP, YFP and Alexa488. We illustrate the potential of the microscope for resolving thin brain structures such as dendritic spines, axons and microglia processes in acute brain slices at more than 50 $\mu$ m from the surface. We also show the potential for two colors superresolution imaging using linear unmixing. Its upright design and the long-working distance water dipping

objective provides access to combine superresolution imaging with electrophysiological recording as well as performing *in vivo* STED imaging.

## Two-Photon Excitation STED Microscopy in Two Colors in Acute Brain Slices

Philipp Bethge,<sup>†‡</sup> Ronan Chéreau,<sup>†‡</sup> Elena Avignone,<sup>†‡</sup> Giovanni Marsicano,<sup>§</sup> and U. Valentin Nägerl<sup>†‡\*</sup>

<sup>†</sup>Interdisciplinary Institute for Neuroscience, Université de Bordeaux, Bordeaux, France; <sup>‡</sup>UMR 5297, Centre National de la Recherche Scientifique, Bordeaux, France; and <sup>§</sup>Université de Bordeaux, INSERM U862 NeuroCentre Magendie, Bordeaux, France

**ABSTRACT** Many cellular structures and organelles are too small to be properly resolved by conventional light microscopy. This is particularly true for dendritic spines and glial processes, which are very small, dynamic, and embedded in dense tissue, making it difficult to image them under realistic experimental conditions. Two-photon microscopy is currently the method of choice for imaging in thick living tissue preparations, both in acute brain slices and in vivo. However, the spatial resolution of a two-photon microscope, which is limited to ~350 nm by the diffraction of light, is not sufficient for resolving many important details of neural morphology, such as the width of spine necks or thin glial processes. Recently developed superresolution approaches, such as stimulated emission depletion microscopy, have set new standards of optical resolution in imaging living tissue. However, the important goal of superresolution imaging with significant subdiffraction resolution has not yet been accomplished in acute brain slices. To overcome this limitation, we have developed a new microscope based on two-photon excitation and pulsed stimulated emission depletion microscopy, which provides unprecedented spatial resolution and excellent experimental access in acute brain slices using a long-working distance objective. The new microscope improves on the spatial resolution of a regular two-photon microscope by a factor of four to six, and it is compatible with time-lapse and simultaneous two-color superresolution imaging in living cells. We demonstrate the potential of this nanoscopy approach for brain slice physiology by imaging the morphology of dendritic spines and microglial cells well below the surface of acute brain slices.

### INTRODUCTION

Most neurons in the mammalian brain are studded with hundreds to thousands of dendritic spines (1). Spines are tiny specializations of the postsynaptic membrane that are packed with receptors, ion channels, and other signaling complexes and mediate fast excitatory synaptic transmission in the brain. Their structural dynamics are thought to be critical for brain development and experience-dependent synaptic plasticity throughout life (2).

Thus, quantitative measurements of the structure and function of spines have been a primary endeavor in neuroscience research for a long time. Getting reasonable optical access is a huge challenge, because they are embedded in dense brain tissue and are oftentimes smaller than what can be resolved by diffraction-limited light microscopy, including two-photon (2P) microscopy.

Moreover, recent studies indicate that spines also interact directly with surrounding glial cells, like astrocytes and microglia (3,4), which extend extremely thin processes. Hence, to study how spines operate and interact with their

partners in a complex and dynamic environment, it is essential to image several cell types at the same time with sufficient spatial resolution below the diffraction limit. In recent years, several big steps have been made in developing methods to make this possible.

Starting a new era in optical microscopy, stimulated emission depletion (STED) microscopy (5–7) has allowed for nanoscale imaging of dynamic events in living tissue, imaging synaptic vesicles (8) and spine morphology (9). Furthermore, several strategies were recently developed for multicolor STED imaging (10–13).

Most STED studies to date have been done in culture systems using oil objectives (e.g., Westphal et al. (8), Nägerl et al. (9), and Willig et al. (14)), but the experimental preparation of choice for synaptic physiologists is acute brain slices. To record healthy cells in acute brain slices, it is necessary to image a few tens of microns deep in the tissue, which cannot be done with oil objectives. Although glycerol objectives can substantially extend optical penetration without compromising spatial resolution (15), they are not compatible with acute brain slices, which call for an upright microscope design and water-immersion objectives with long working distances to accommodate electrophysiological recording electrodes.

The combination of 2P excitation and STED (2P-STED) microscopy (16,17) opened new perspectives for superresolution imaging in deep tissue. However, the use of continuous wave (CW) STED lasers limited the spatial resolution to 250 nm in living tissue (16).

Submitted August 27, 2012, and accepted for publication December 11, 2012.

\*Correspondence: valentin.nagerl@u-bordeaux2.fr

This is an Open Access article distributed under the terms of the Creative Commons-Attribution Noncommercial License (<http://creativecommons.org/licenses/by-nc/2.0/>), which permits unrestricted noncommercial use, distribution, and reproduction in any medium, provided the original work is properly cited.

Editor: Paul Wiseman.

© 2013 by the Biophysical Society  
0006-3495/13/02/0778/8 \$2.00

<http://dx.doi.org/10.1016/j.bpj.2012.12.054>



In this study, our goal was to overcome these limitations and to achieve true subdiffraction imaging in acute brain slices a few cell layers below the tissue surface, which corresponds to a depth usually targeted in patch-clamp electrophysiology experiments. To this end, we developed a new 2P-STED microscope incorporating a pulsed STED laser, a long-working distance water objective and spectral detection for two-color imaging.

We characterize the 2P-STED microscope and illustrate its potential by imaging dendritic spines in acute brain slices. The spatial resolution in the focal plane of the new microscope is four to six times better than that of a regular, diffraction-limited 2P microscope. Furthermore, we show that the microscope is compatible with time-lapse and two-color superresolution imaging, using transgenic mice in which neurons and microglia are labeled with yellow (YFP) and green fluorescent protein (GFP), respectively.

## MATERIALS AND METHODS

### Lasers

A femtosecond mode-locked Ti:Sapphire laser (Mai Tai, Spectra-Physics, Darmstadt, Germany) operating at ~80 MHz and a wavelength of 797 nm was used in combination with an optical parametric oscillator (OPO BASIC Ring fs, APE, Berlin, Germany) to produce pulses at a wavelength of 592 nm (STED laser). The pulses of originally ~200-fs duration were stretched to >68 ps by passing them through a 25-cm dispersive glass rod (high-refractive-index flint glass) and a 20-m-long polarization-preserving fiber (Schäfer & Kirchhoff, Hamburg, Germany). A reflection from the STED laser was used to synchronize a second mode-locked ultrafast Ti:Sapphire laser (Tsunami, Spectra-Physics) operating at 910 nm for 2P excitation (2P laser).

Synchronization and fine pulse delay (<2 ns) was performed via phase-locked loop electronics (3930, Lok-to-Clock, Spectra-Physics), while the coarse delay was set by varying the length of the BNC cable, using a fast photodiode (3932-LX, Spectra-Physics) placed below the microscope objective for readout.

Laser intensities were controlled via dedicated electro-optical modulators (Conoptics, Danbury, CT) for the 2P and STED laser beams. The time-averaged power at the back focal plane (BFP) of the objective was between 15 and 25 mW for the 2P light and between 20 and 40 mW for the STED light, depending on imaging depth and sample brightness.

### Microscope setup

The microscope was built around a standard commercial research microscope (BX51WI, Olympus, Hamburg, Germany) using scan and tube lenses from the microscope manufacturer. The telecentric scanner (Yanus IV, TILL Photonics, Gräfelfing, Germany) was placed so that both scan axes are projected into the BFP of the objective, ensuring that the 2P and STED laser beams stay stationary at the BFP during scanning.

A water-immersion objective with a long working distance (1.5 mm) and equipped with a correction collar was used for all experiments (60X LUMFI, 1.1 NA, Olympus). The correction collar was adjusted to optimize the STED doughnut using gold nanospheres (diameter = 150 nm; BBInternational, Cardiff, United Kingdom) and slightly re-adjusted for particular imaging depths, using the 2P fluorescence signal as readout. The  $z$ -position of the objective was controlled via a piezo actuator (P-721 PIFOC, PI Physik Instrumente, Karlsruhe, Germany). Signal detection and peripheral hardware were controlled by the Inspector scan-

ning software (18) via data acquisition cards (6259 M, 2090A, National Instruments, Austin, TX).

A polymeric phase plate (RPC Photonics, Rochester, NY) was used to create the STED doughnut and a bandpass filter (593/40, AHF Analysentechnik, Tübingen, Germany) was used to spectrally clean up the STED laser beam. The 2P and STED laser beams were combined using a dichroic mirror (F73-700UV, AHF) before the scanner.

The fluorescence signal was detected in descanned mode and separated from the excitation and STED light by a longpass dichroic (580 DCXRUV, AHF). The detectors were protected from the 2P and STED light by suitable blocking and emission filters (680SP-25, 594S-25, 520-70, Semrock, Rochester, NY). The signal was spectrally divided into two channels by a dichroic mirror (514RS, Semrock) before being focused onto multimode fibers (100- $\mu$ m core diameter, which corresponds to 120% of the back-projected Airy disk), terminating on avalanche photodiodes (SPCM-AQR-13-FC, PerkinElmer, Waltham, MA).

### Microscope alignment

For spatial alignment of the 2P and STED lasers and quality control of the doughnut (Fig. 1 D), a pellicle beam splitter (Thorlabs, Maisons-Laffite, France) was flipped into the beam path so that the reflection from gold nanospheres could be detected by a photomultiplier tube (MD963, PerkinElmer). A piezo-controlled motorized mirror (AG-M100N, Newport, Beane la Rolande, France) and a telescope were used to align the doughnut on the excitation spot in all three dimensions. Doughnut quality (shape and null) was optimized via achromatic  $\lambda/2$  and  $\lambda/4$  wave plates (Qioptiq, Paris, France). Optical resolution (Fig. 2 D) was assessed using fluorescent nanospheres (Fluo Spheres, yellow-green, diameter = 0.04  $\mu$ m, Invitrogen).

### Animals and labeling

Two transgenic mouse lines (C57BL/6 background) were used: Thy1<sup>eYFP/cYFP</sup> mice that express YFP in a subpopulation of principal neurons in the hippocampus as well as in layer 4/5 of cortex, and CX3CR1<sup>eGFP/cGFP</sup> mice that express GFP in microglial cells (Jackson Labs, Bar Harbor, ME). In experiments where only neurons were imaged, heterozygous Thy1<sup>+eYFP</sup> mice were used. In experiments where neurons and microglia were imaged, mice obtained from the crossbreeding of the two mouse lines were used (CX3CR1<sup>+eGFP</sup>; Thy1<sup>+eYFP</sup>). All experiments were carried out in accordance with the National Code of Ethics on Animal Experimentation (Carte Nationale d'éthique sur l'expérimentation animale; Ministère de l'enseignement et de la recherche, Ministère de l'agriculture et de la pêche) and approved by the Committee of Ethics of Bordeaux (No. 3306001).

### Acute brain slices

Animals 21–40 days old were killed by cervical dislocation, and their brains were quickly removed and placed in ice-cold sucrose-based artificial cerebrospinal fluid (ACSF) containing (in mM) 210 sucrose, 10 glucose, 2 KCl, 26 NaHCO<sub>3</sub>, 1.25 NaH<sub>2</sub>PO<sub>4</sub>, 0.1 CaCl<sub>2</sub>, and 6 MgCl (pH 7.4, osmolarity ~320 mOsm/L), which was bubbled with carbogen (95% O<sub>2</sub>/5% CO<sub>2</sub>). Sagittal 350- $\mu$ m-thick slices were cut using a vibratome (VT1200, Leica, Mannheim, Germany) and transferred to a heated (32°C) holding chamber with NaCl-based ACSF bubbled with carbogen, which consisted of (in mM) 124 NaCl, 3 KCl, 26 NaHCO<sub>3</sub>, 1.25 NaH<sub>2</sub>PO<sub>4</sub>, 10 glucose, 2 CaCl<sub>2</sub>, 1 MgCl, and 0.6 Trolox (pH 7.4, osmolarity ~305 mOsm/L) for 1 h. These slices were subsequently maintained at room temperature for a maximum of 4 h. For the imaging experiments, the slices were transferred to a submerged recording chamber, where they were continuously perfused (2.1 mL/min) with ACSF at room temperature.

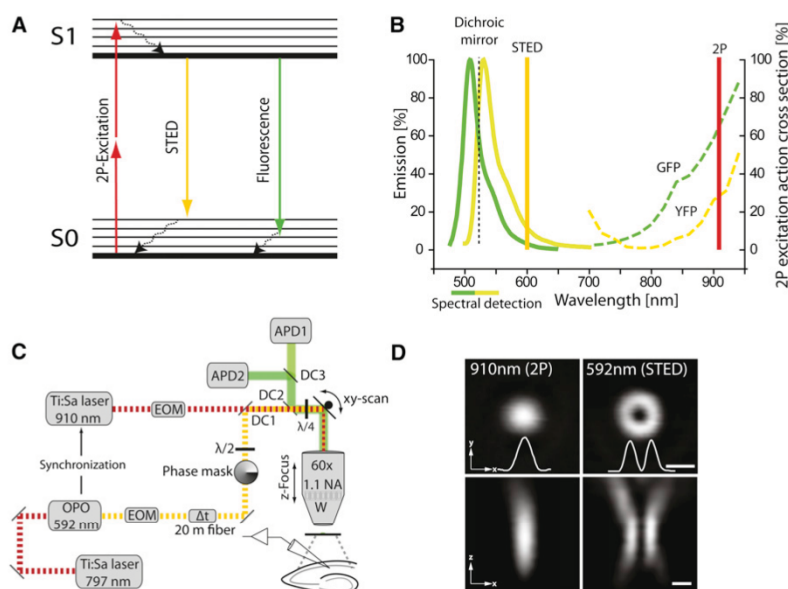


**FIGURE 1** Principle and design of a pulsed 2P-STED microscope. (A) Simplified Jablonski diagram of the molecular excitation states in 2P-STED microscopy. The molecule is excited to the excited state (S1) by two-photon absorption and returns from there to the ground state (S0) by the emission of fluorescence. The incidence of STED light quenches the fluorescence and returns the molecule to S0 before fluorescence can occur (curved dashed arrows show internal conversion). (B) Two-photon excitation action cross section and emission spectra for GFP and YFP (Warren Zipfel, Cornell University, Ithaca, NY). Simultaneous quenching of GFP and YFP by a single laser beam of 592 nm is possible because of the highly overlapping tails of the emission spectra. Two-photon excitation is performed at 910 nm. The emission signal is spectrally separated and detected in two channels. (C) Schematic of beam path. The femtosecond pulsed Ti:Sa laser used for 2P excitation is routed through a beam scanner into an upright microscope and synchronized with the STED laser (Ti:Sa/optical parametric oscillator (OPO)). Femtosecond pulses emitted from the Ti:Sa/OPO are broadened by a 20-m-long polarization-preserving single-mode fiber. The doughnut is

formed by a helical phase mask. A long-working distance, water-immersion objective is used. It is equipped with a correction ring to correct spherical aberrations due to mismatches in refractive index at the lens-sample interface.  $\lambda/2$ , half-wave plate;  $\lambda/4$ , quarter-wave plate; DC, dichroic mirrors, NA, numerical aperture;  $\Delta t$ , pulse broadening fiber; xy-scan, scanner for  $x$  and  $y$  dimension; APD, avalanche photodiode; EOM = electro-optical modulator. (D) Reflections of the laser beams from gold particles used for visualization and spatial alignment of the excitation and STED beams. The laser beams are routed through a pellicle beam splitter so that the reflections can be detected by a photomultiplier tube. This allows for the characterization of the excitation and STED beams and illustrates the doughnut-like intensity distribution of the STED laser. Scale bar, 500 nm.

## Image acquisition and analysis

All images were acquired with a pixel size of 19.5 nm ( $512 \times 512$  pixels,  $10 \mu\text{m} \times 10 \mu\text{m}$ , except see Fig. 4 B3, which is  $1024 \times 1024$  pixels,  $40 \mu\text{m} \times 40 \mu\text{m}$ , with a pixel size of 39 nm) and a pixel dwell time of 30  $\mu\text{s}$ , which corresponds to about 8 s acquisition time for a  $10 \mu\text{m} \times 10 \mu\text{m}$  field of view. Imaging depth into the slice was determined by the piezo  $z$ -focus, the fluorescence signal on top of the slice defining the zero  $z$ -position. Image analysis was done on raw data using ImageJ. Images presented in the figures were filtered by a 1-pixel Gaussian filter to reduce noise. To quantify and compare the line profiles from 2P and 2P-STED images, we used the Lorentzian function:

$$y = y_0 + \frac{2A}{\pi} \frac{\Gamma}{4(x - x_c)^2 + \Gamma^2},$$

where  $y_0$  and  $A$  are constants,  $x_c$  is the center, and  $\Gamma$  is the width of the curve.

Two-color images are shown merged with and without linear unmixing using a plugin for ImageJ as described before (12). Unless stated otherwise, single frames from a  $z$ -stack ( $\Delta z$  typically 400 nm) are shown.

## Statistics

Data are expressed as the mean  $\pm$  SE. A two-tailed unpaired  $t$ -test was used to compare spine neck widths ( $\Gamma$ ) measured for 2P and 2P-STED in the CA1, cortex, and for the two groups pooled. Multiple comparisons were post-hoc Bonferroni-corrected. A nonparametric Kolmogorov-Smirnov test was additionally used for groups containing  $< 17$  data points, confirming the results of the parametric  $t$ -test. Data from 12 mice were included in this study. Tests marked with (\*\*\*) in Fig. 3 C are significant, with  $p < 10^{-12}$ .

## RESULTS

### Construction of the microscope

We built a 2P-STED microscope for two-color sub-diffraction imaging in brain slices using a long-working distance, water-immersion objective as outlined in Fig. 1, A–C. For coupling the lasers into the microscope, we first checked the reflection of the 2P and STED light using gold beads (Fig. 1 D). We optimized the symmetry and central minimum of the STED doughnut by adjusting a  $\lambda/4$  wave plate placed in front of the scanner. The intensity of the STED beam at the doughnut center was  $< 1\%$  of the intensity measured at the rim of the doughnut (Fig. 1 D), which was indistinguishable from background noise.

### Performance of the microscope

Because we used pulsed lasers for 2P excitation and the STED effect, the lasers had to be synchronized and their pulses had to arrive at the sample with an optimal delay to achieve efficient quenching of the 2P fluorescence by the STED laser. Indeed, quenching depended on how much of the STED pulse overlaps with the time that the molecules spent in the excited state after 2P excitation. Fig. 2, A and B, illustrates that 80% quenching efficiency in a sea of dye fluorescence ( $\sim 1$  mM calcein) can be achieved.

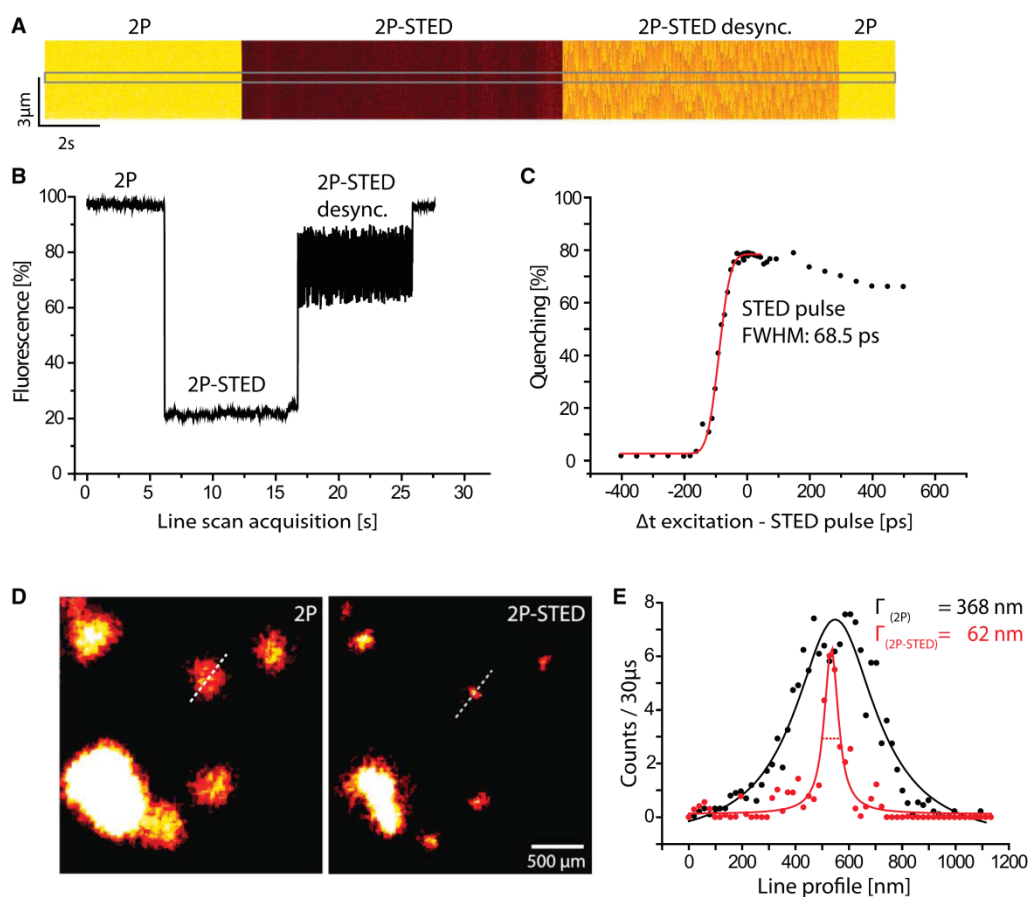


FIGURE 2 Fluorescence quenching and spatial resolution in 2P-STED microscopy. (A) Line scans in a fluorescent solution excited by the 2P laser. The signal is quenched by a pulsed STED laser. Desynchronization strongly attenuates this effect. (B) Quantification of the signal intensity along the rectangle indicated in A. Desynchronization greatly reduces quenching efficiency and increases variability. Fluorescence quenching is 80% when the 2P and STED pulses are synchronized and aligned in space and time. (C) 2P-STED requires a precise relative temporal delay of the synchronized laser pulses, which can be used to probe the duration of the STED laser pulse. Quenching efficiency is plotted as a function of the relative delay between the excitation and the STED beam. Fitting the data with a Gaussian error function (red) indicates a STED pulse duration (FWHM) of at least 68.5 ps. (D) 2P and 2P-STED images of fluorescent beads (diameter = 40 nm). A clear resolution enhancement can be observed in 2P-STED relative to 2P excitation. (E) Quantification of the line indicated in D and fitting with a Lorentzian function returns a width of 62 nm for 2P-STED (red) as compared with 368 nm for 2P (black).

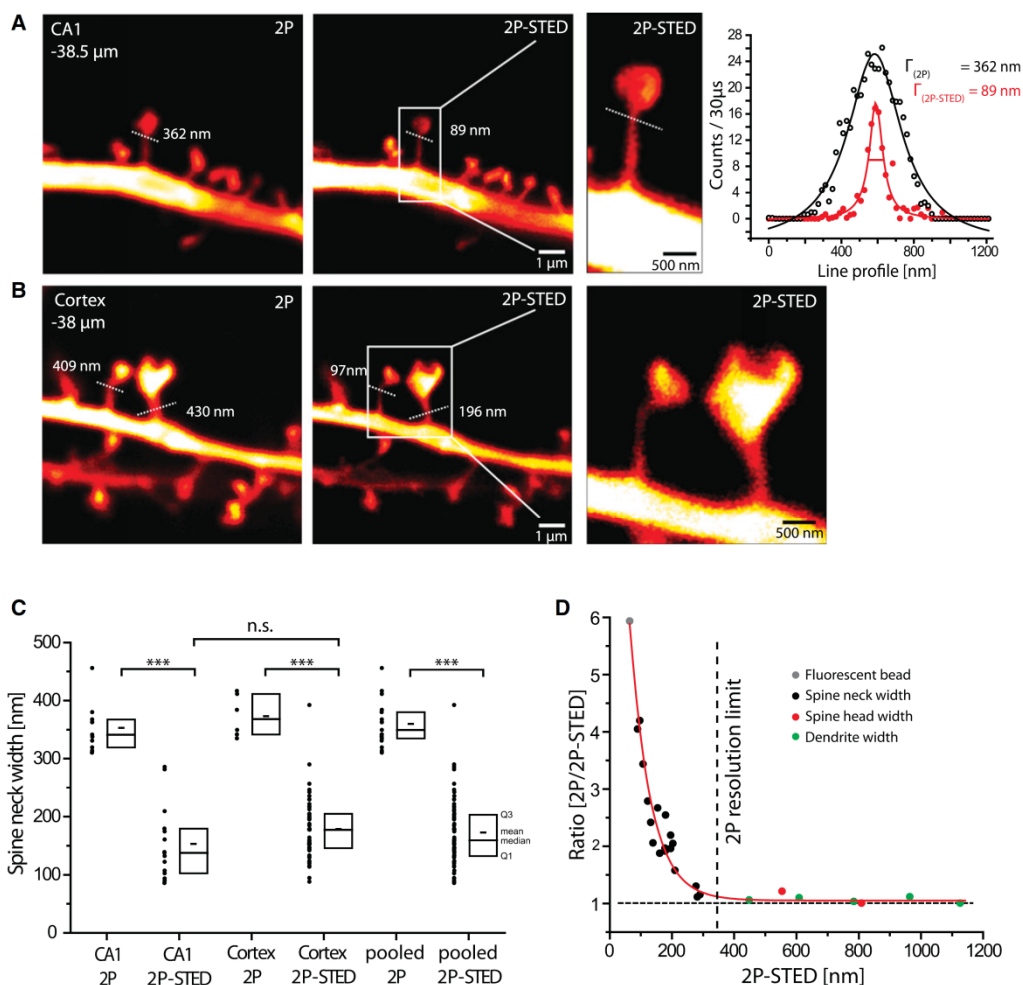
Conversely, when the synchronization is turned off, the quenching effect is strongly diminished (Fig. 2 B).

Fig. 2 C illustrates the fluorescence quenching efficiency by the STED laser as a function of the relative delay between the laser pulses, where zero refers to the optimal delay. Changing the relative delay between pulses results in a rapid increase of quenching to a maximum of 80% before it decreases again gradually. Whereas the rising phase of the curve should be mostly defined by the duration of the STED pulse, the decay should be defined by the lifetime of the fluorophore (19).

Based on the rising phase (fitting a Gaussian error function), we estimated the duration of the STED pulse to be at least 68.5 ps (full width at half maximum (FWHM)) using a 20-m-long polarization-preserving optical fiber,

which is consistent with pulse durations of 200–300 ps reported for 120-m-long optical fibers (20).

To check the performance of the 2P-STED microscope, we imaged subdiffraction-sized fluorescent beads (diameter = 40 nm) and determined the point-spread functions (PSFs) for the 2P and 2P-STED case (Fig. 2 D). The width of the PSF is an important indicator of the spatial resolution of the microscope. Using a Lorentzian function to fit line profiles drawn through the centers of individual beads, we measured a PSF width of 368 nm for the 2P case, which corresponds well to the expected spatial resolution of a diffraction-limited 2P microscope given the wavelength of the 2P light (910 nm) and the NA of the objective (1.1) (21). Imaging the same bead in STED mode, the PSF width was 62 nm, which corresponds to about a sixfold



**FIGURE 3** 2P-STED microscopy in acute brain slices. (A and B) 2P and 2P-STED images of dendritic spines of YFP-labeled CA1 (A) and cortical (B) pyramidal neurons in acute slices from Thy1-YFP transgenic mice. Spine necks appear much thinner in 2P-STED compared to 2P images. Dotted lines indicate spine neck widths (Lorentzian fit of the line profile of the line indicated). The difference in width between 2P imaging ( $\Gamma = 362$  nm) and 2P-STED imaging ( $\Gamma = 89$  nm) demonstrates the resolution enhancement by 2P-STED. (C) Quantification of spine neck widths of CA1 and cortex imaged in 2P and 2P-STED modes. No difference between CA1 and cortex was detected. 2P imaging clearly overestimates spine neck widths when compared to the 2P-STED mode. Boxplot indicate Q1 and Q3 (first and third quartile), median and mean (large and small lines, respectively). (D) Plot of 2P-STED measurements versus the ratio between 2P and 2P-STED of the same object. As expected, the ratio is 1 when the structures are larger than the resolution limit of 2P microscopy ( $\sim 350$  nm), but it increases steeply when the structures are  $< 350$  nm in size.

improvement in spatial resolution over the 2P case. The peak photon count at the center of the bead was only slightly ( $\sim 10\%$ ) reduced (Fig. 2 E), confirming that the STED light intensity in the center of the doughnut is very low.

### Subdiffraction imaging of dendritic spines in acute slices

To check whether we could achieve subdiffraction spatial resolution in acute brain slices, we imaged dendritic spines from transgenic mice expressing YFP as a volume label in a subset of hippocampal and cortical neurons. We compared

the performance of the 2P-STED with the 2P microscope by imaging spines with or without the STED light. In general, the spine necks appeared substantially wider without the STED light, whereas the appearance of the 2P-STED images was much crisper (Fig. 3 and Fig. S1).

To confirm this impression quantitatively, we measured line profiles across the spine necks and fitted them with a Lorentzian function as above. In the example illustrated in Fig. 3 A (a spine of a hippocampal CA1 pyramidal neuron imaged at a depth of  $38.5 \mu\text{m}$ ), the neck appeared to be  $362$  nm wide in the 2P image but only  $89$  nm in the 2P-STED image. This fourfold difference demonstrates that

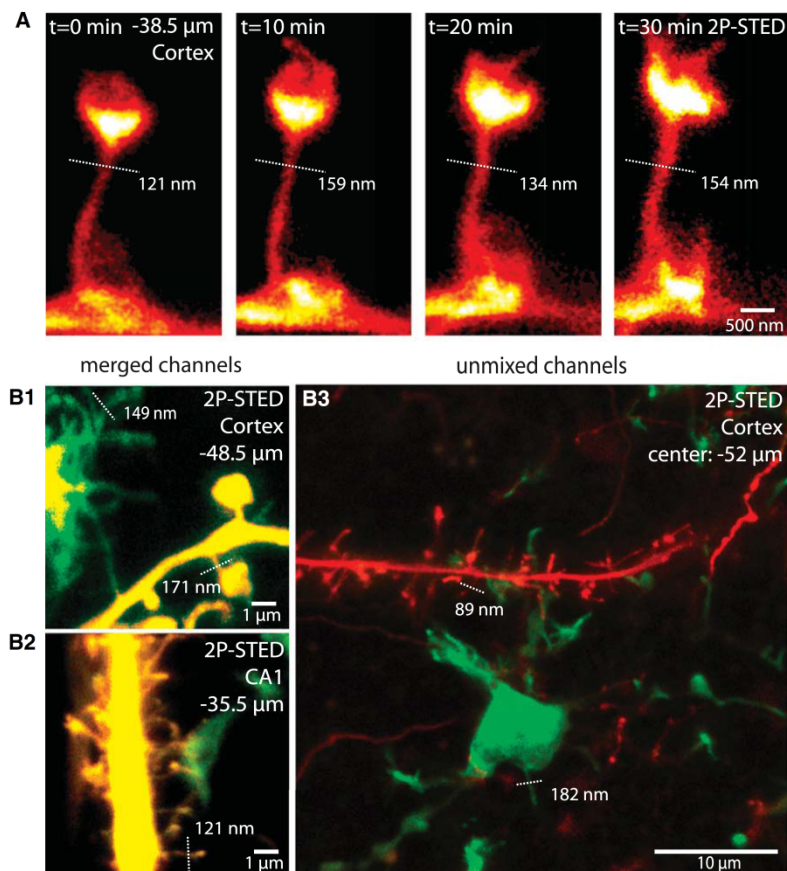


**FIGURE 4** Time-lapse and dual-color 2P-STED imaging. (A) Time-lapse images of a cortical spine acquired at 38.5  $\mu\text{m}$  below the tissue surface. Individual time points are average projections of two frames based on multiple sections (5 frames/stack, four stacks,  $\Delta z = 400$  nm). (B) Two-color 2P-STED imaging of neurons and microglia. Transgenic mice (CX3CR1<sup>+/eGFP</sup>; Thy1<sup>+/eYFP</sup>) express YFP in neurons and GFP in microglia. Superresolved microglial processes ( $\Gamma = 149$  nm) can be observed (B1), as can a microglial process contacting dendritic spines (B2) and a maximum-intensity projection of a z-stack of images (19 frames,  $40 \times 40 \mu\text{m}$ , from  $-49.5$  to  $-56.5 \mu\text{m}$ ,  $\Delta z = 368$  nm) in the cortex (B3). The high magnification images (B1 and B2) are merges of both color channels (green (GFP) and yellow (YFP)); the overview image (B3) is linearly unmixed, effectively separating both channels (green (GFP) and red (YFP)). Dotted lines indicate spine neck widths ( $\Gamma$ , Lorentzian fit of raw data).

the STED approach can be used to achieve a substantial gain in spatial resolution, well below the surface of living brain tissue, using a long-working distance water-immersion objective. It is important to note that the peak signal intensity in 2P-STED mode was only reduced by  $\sim 30\%$  compared with the 2P signal (Fig. 3 A), suggesting that the minimum of the STED doughnut was fairly intact at this imaging depth.

We also imaged spines from layer 4/5 of cortical pyramidal neurons, imaged in the molecular layer of visual and parietal cortices at about the same depth (Fig. 3 B). Similar to spines of hippocampal neurons, the spine necks of cortical neurons appear much thinner in 2P-STED than in 2P images ( $\Gamma = 97$  nm for 2P-STED vs.  $\Gamma = 409$  nm for 2P). The differences between 2P and 2P-STED imaging were clear-cut and highly significant ( $p < 0.0001$ , Fig. 3 C). We did not detect any significant differences in width between spine necks in hippocampus and cortex, irrespective of whether 2P or 2P-STED was used ( $\Gamma_{2P \text{ CA1}} = 352 \pm 12$  nm,  $n = 11$ ;  $\Gamma_{2P\text{-STED CA1}} = 153 \pm 17$  nm,  $n = 15$ ;  $\Gamma_{2P \text{ Cortex}} = 372 \pm 15$  nm,  $n = 6$ ;  $\Gamma_{2P\text{-STED Cortex}} = 178 \pm 8$  nm,  $n = 49$ ) (Fig. 3 C).

Taken together, 2P-STED yields substantially better resolved images of dendritic spines compared to 2P microscopy, well below the surface of acute brain slices. To illustrate the gain in resolution quantitatively, we plotted the ratio of 2P to 2P-STED measurements as a function of the widths of assorted structures measured by 2P-STED (Fig. 3 D). This ratio equals 1 for structures larger than the 2P diffraction limit, but increases sharply for structures below it.

### Time-lapse imaging

Next, we addressed the potential issue of phototoxicity and bleaching during 2P-STED imaging. To this end, we repeatedly (20 times) imaged the same stretch of dendrite for 30 min ( $\Delta t = 10$  min) and looked for signs of photodamage such as blebbing. Our experiments demonstrate that it is possible to repeatedly acquire superresolved images with our 2P-STED microscope without obvious photodamage (Fig. 4 A). However, to avoid or reduce deleterious effects, which are a general concern in fluorescence microscopy, it was important to optimize the imaging parameters

(e.g., laser powers, pixel dwell times, image sizes, etc.), which are linked to several factors, including slice quality, sample brightness, and imaging depth.

### Two-color imaging

Finally, we performed two-color 2P-STED imaging using an approach we recently developed for STED microscopy, which is based on a single laser pair for fluorescence excitation and STED quenching (12). To this end, we modified the microscope by adding a dichroic mirror and a second detection channel for spectral detection. To illustrate the potential of using these techniques in combination, we imaged brain slices from transgenic mice in which neurons and microglia are fluorescently labeled with YFP and GFP, respectively. The images in Fig. 4 B demonstrate the ability of the new approach to acquire superresolved images of volume-labeled dendritic spines and microglial processes well below the surface of acute brain slices. Although spectral detection already provides for reasonable color contrast (Fig. 4, B1 and B2), linear unmixing of the fluorescence channels can improve color separation substantially (Fig. 4 B3).

### DISCUSSION

We present a novel kind of microscope for two-color super-resolution imaging of neural morphology well below the surface of acute brain slices using YFP and GFP as volume labels. It is based on 2P excitation and pulsed STED microscopy and hence reconciles many powerful features, such as subdiffraction spatial resolution, two-color imaging, optical sectioning, depth penetration, the use of living samples, and the possibility of combining it with electrophysiological approaches.

We employed a long-working distance water-immersion objective with an NA of 1.1, which is relatively low compared to the glycerol- and oil-immersion objectives (1.3 and 1.4, respectively) generally used in STED microscopy (9,14,15,22). Using spine necks to estimate our resolution, the spatial resolution at an imaging depth of  $\sim 40\text{--}50\ \mu\text{m}$  is likely to be around 60–70 nm, considering that spine necks are finite in size ( $>50\ \text{nm}$ , as indicated by electron microscopy (23)) and thus do not mimic point sources of light.

STED microscopy, which was initially used in neurobiology to acquire superresolved images of protein distributions inside cells by immunohistochemistry (14,24), has recently been extended to live-cell imaging of dendritic spine morphology (9,16), greatly facilitating investigation of the structure and function of synapses, which is a major research topic in neuroscience.

Most previous studies have used high-NA oil or glycerol objectives with short working distances, which is incompatible with acute brain slices, because this preparation

requires water-immersion objectives with long working distances and an upright microscope design. Acute brain slices are the preparation of choice for most synaptic physiologists because of the experimental access they provide for pharmacological and electrophysiological experiments.

Initially, STED microscopy was based on a confocal design and single-photon excitation, but recently the use of 2P excitation has been reported. The first two studies demonstrated the principle of 2P-STED using CW lasers for the STED beam (16,17), which are easier to implement than pulsed lasers. However, as the CW laser is much less efficient at quenching fluorescence than the pulsed laser, much more laser power ( $>10\text{-fold}$ ) is needed to achieve a comparable gain in spatial resolution, which is usually prohibitive for living tissue. As a consequence, 2P-STED microscopy in living tissue has been limited to  $>250\ \text{nm}$  in spatial resolution. Subsequent studies have used pulsed STED lasers in conjunction with 2P excitation (25,26), but those studies used inverted microscopes with oil objectives on fixed samples.

Here, we demonstrate 2P-STED time-lapse imaging in two colors in acute brain slices with a four- to sixfold improvement in spatial resolution over the 2P case. The STED laser intensities required to achieve the gain in resolution were substantially less than those reported previously (16,26), which is important for reducing phototoxicity and bleaching.

We speculate that the quality of the doughnut, which featured a very low minimum at its center, and the efficiency of quenching GFP and YFP with short laser pulses afforded the use of relatively modest STED laser powers.

Illustrating the potential of the new 2P-STED approach, we imaged dendritic spines in acute brain slices and measured superresolved spine necks at a few tens of microns below the tissue surface. The spine-neck widths of pyramidal neurons in the CA1 region of the hippocampus and cortex correspond well to those reported by electron microscopy (23,27), in our previous work (9), and by other recent superresolution approaches (28,29), and they are much thinner than is indicated by confocal measurements. For this reason, spine necks are thought to represent a diffusion barrier for signaling molecules, allowing for biophysical compartmentalization of synapses (15,30–33). Moreover, the sizes of the microglial processes we have observed are comparable with those of STED images in perfusion-fixed brain-tissue sections (data not shown).

Interestingly, the ability to measure the level of STED quenching as a function of the delay between the laser pulses provides a straightforward way to estimate the duration of the STED laser pulse, which otherwise requires special equipment. Likewise, fluorescence quenching by the STED laser can also be used to estimate the fluorescence lifetime of the fluorophores, as suggested previously (19), which is normally done using time-correlated single-photon counting instrumentation (34).

In summary, we have developed a new 2P-STED microscope that can be assembled using all commercial components and demonstrated its potential for investigating synapses and glial cells with unprecedented spatial resolution in acute brain slices using genetically encoded fluorophores.

## SUPPORTING MATERIAL

Fig. S1 is available at [http://www.biophysj.org/biophysj/supplemental/S0006-3495\(13\)00074-X](http://www.biophysj.org/biophysj/supplemental/S0006-3495(13)00074-X).

This work was supported by a Ph.D. fellowship from the 7th Framework Program (FP7) Marie Curie ITN SyMBaD to P.B. (cosupervised by G.M. and U.V.N.), and grants from the Regional Council of Aquitaine (CRA), Inserm, the French National Research Agency (ANR), and the Human Frontier Science Program, to U.V.N.

We thank S. Berning for discussions on the design of the microscope and S. W. Hell for providing optomechanical components (both affiliated with the Max Planck Institute for Biophysical Chemistry, Göttingen, Germany). We thank members of the lab (M.O. Lenz, A. Panatier, and J. Tonnesen) and L. S. Wijetunge (University of Edinburgh, Edinburgh, Scotland) for discussions and comments on the manuscript and J. Angibaud for technical support.

## REFERENCES

- Ramón y Cajal, S. 1995. *Histology of the nervous system of man and vertebrates*. Oxford University Press, New York.
- Holtmaat, A., and K. Svoboda. 2009. Experience-dependent structural synaptic plasticity in the mammalian brain. *Nat. Rev. Neurosci.* 10: 647–658.
- Araque, A., G. Carmignoto, and P. G. Haydon. 2001. Dynamic signaling between astrocytes and neurons. *Annu. Rev. Physiol.* 63: 795–813.
- Tremblay, M. E., B. Stevens, ..., A. Nimmerjahn. 2011. The role of microglia in the healthy brain. *J. Neurosci.* 31:16064–16069.
- Hell, S. W. 2007. Far-field optical nanoscopy. *Science*. 316:1153–1158.
- Hell, S. W., and J. Wichmann. 1994. Breaking the diffraction resolution limit by stimulated emission: stimulated-emission-depletion fluorescence microscopy. *Opt. Lett.* 19:780–782.
- Klar, T. A., S. Jakobs, ..., S. W. Hell. 2000. Fluorescence microscopy with diffraction resolution barrier broken by stimulated emission. *Proc. Natl. Acad. Sci. USA*. 97:8206–8210.
- Westphal, V., S. O. Rizzoli, ..., S. W. Hell. 2008. Video-rate far-field optical nanoscopy dissects synaptic vesicle movement. *Science*. 320: 246–249.
- Nägerl, U. V., K. I. Willig, ..., T. Bonhoeffer. 2008. Live-cell imaging of dendritic spines by STED microscopy. *Proc. Natl. Acad. Sci. USA*. 105:18982–18987.
- Bückers, J., D. Wildanger, ..., S. W. Hell. 2011. Simultaneous multi-lifetime multi-color STED imaging for colocalization analyses. *Opt. Express*. 19:3130–3143.
- Pellett, P. A., X. Sun, ..., J. Bewersdorf. 2011. Two-color STED microscopy in living cells. *Biomed. Opt. Express*. 2:2364–2371.
- Tønnesen, J., F. Nadrigny, ..., U. V. Nägerl. 2011. Two-color STED microscopy of living synapses using a single laser-beam pair. *Biophys. J.* 101:2545–2552.
- Willig, K. I., A. C. Stiel, ..., S. W. Hell. 2011. Dual-label STED nanoscopy of living cells using photochromism. *Nano Lett.* 11:3970–3973.
- Willig, K. I., S. O. Rizzoli, ..., S. W. Hell. 2006. STED microscopy reveals that synaptotagmin remains clustered after synaptic vesicle exocytosis. *Nature*. 440:935–939.
- Urban, N. T., K. I. Willig, ..., U. V. Nägerl. 2011. STED nanoscopy of actin dynamics in synapses deep inside living brain slices. *Biophys. J.* 101:1277–1284.
- Ding, J. B., K. T. Takasaki, and B. L. Sabatini. 2009. Supraresolution imaging in brain slices using stimulated-emission depletion two-photon laser scanning microscopy. *Neuron*. 63:429–437.
- Moneron, G., and S. W. Hell. 2009. Two-photon excitation STED microscopy. *Opt. Express*. 17:14567–14573.
- Inspector. [www.max-planck-innovation.de/de/industrie/technologie/angebote/software/](http://www.max-planck-innovation.de/de/industrie/technologie/angebote/software/).
- Schrader, M., F. Meinecke, ..., S. W. Hell. 1995. Monitoring the excited state of a fluorophore in a microscope by stimulated emission. *Bioimaging*. 3:147–153.
- Eggeling, C., C. Ringemann, ..., S. W. Hell. 2009. Direct observation of the nanoscale dynamics of membrane lipids in a living cell. *Nature*. 457:1159–1162.
- Zipfel, W. R., R. M. Williams, and W. W. Webb. 2003. Nonlinear magic: multiphoton microscopy in the biosciences. *Nat. Biotechnol.* 21:1369–1377.
- Berning, S., K. I. Willig, ..., S. W. Hell. 2012. Nanoscopy in a living mouse brain. *Science*. 335:551.
- Harris, K. M., F. E. Jensen, and B. Tsao. 1992. Three-dimensional structure of dendritic spines and synapses in rat hippocampus (CA1) at postnatal day 15 and adult ages: implications for the maturation of synaptic physiology and long-term potentiation. *J. Neurosci.* 12: 2685–2705.
- Sieber, J. J., K. I. Willig, ..., T. Lang. 2007. Anatomy and dynamics of a supramolecular membrane protein cluster. *Science*. 317:1072–1076.
- Li, Q., S. S. Wu, and K. C. Chou. 2009. Subdiffraction-limit two-photon fluorescence microscopy for GFP-tagged cell imaging. *Biophys. J.* 97:3224–3228.
- Bianchini, P., B. Harke, ..., A. Diaspro. 2012. Single-wavelength two-photon excitation-stimulated emission depletion (SW2PE-STED) superresolution imaging. *Proc. Natl. Acad. Sci. USA*. 109:6390–6393.
- Arellano, J. I., R. Benavides-Piccione, ..., R. Yuste. 2007. Ultrastructure of dendritic spines: correlation between synaptic and spine morphologies. *Front Neurosci.* 1:131–143.
- Testa, I., N. T. Urban, ..., S. W. Hell. 2012. Nanoscopy of living brain slices with low light levels. *Neuron*. 75:992–1000.
- Izeddin, I., C. G. Specht, ..., M. Dahan. 2011. Super-resolution dynamic imaging of dendritic spines using a low-affinity photoconvertible actin probe. *PLoS ONE*. 6:e15611.
- Svoboda, K., D. W. Tank, and W. Denk. 1996. Direct measurement of coupling between dendritic spines and shafts. *Science*. 272:716–719.
- Grunditz, A., N. Holbro, ..., T. G. Oertner. 2008. Spine neck plasticity controls postsynaptic calcium signals through electrical compartmentalization. *J. Neurosci.* 28:13457–13466.
- Bloodgood, B. L., and B. L. Sabatini. 2005. Neuronal activity regulates diffusion across the neck of dendritic spines. *Science*. 310:866–869.
- Araya, R., J. Jiang, ..., R. Yuste. 2006. The spine neck filters membrane potentials. *Proc. Natl. Acad. Sci. USA*. 103:17961–17966.
- Lakowicz, J. R. 2006. *Principles of Fluorescence Spectroscopy*. Springer, New York.

## Two-Photon-Excitation STED Microscopy in Two Colors in Acute Brain Slices

Philipp Bethge,<sup>†‡</sup> Ronan Chéreau,<sup>†‡</sup> Elena Avignone,<sup>†‡</sup> Giovanni Marsicano,<sup>§</sup> and U. Valentin Nägerl<sup>†‡\*</sup>

<sup>†</sup>University Bordeaux, Interdisciplinary Institute for Neuroscience, Bordeaux, France; <sup>‡</sup>Centre National de la Recherche Scientifique, Interdisciplinary Institute for Neuroscience, Bordeaux, France; and <sup>§</sup>University Bordeaux, Neurocentre, Institut National de la Santé et de la Recherche Médicale, Bordeaux, France

Bethge et al.

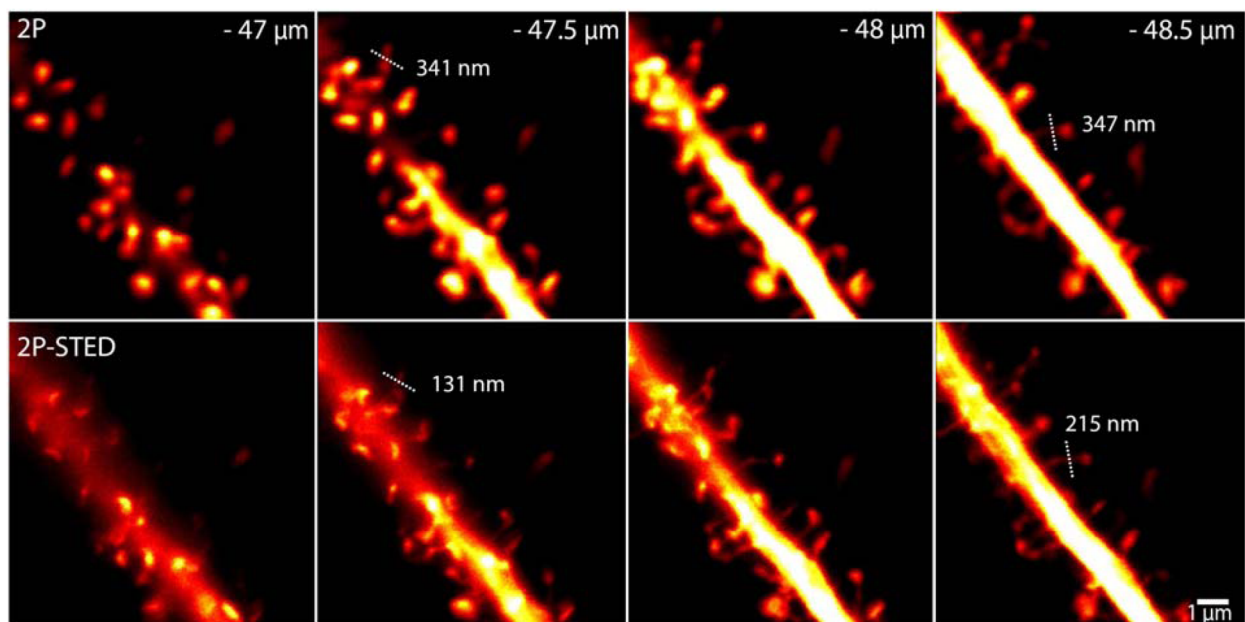
Superresolution Imaging in Acute Brain Slices

Submitted August 27, 2012, and accepted for publication December 11, 2012.

\*Correspondence: valentin.nagerl@u-bordeaux2.fr

This is an Open Access article distributed under the terms of the Creative Commons-Attribution Noncommercial License (<http://creativecommons.org/licenses/by-nc/2.0/>), which permits unrestricted noncommercial use, distribution, and reproduction in any medium, provided the original work is properly cited.

### Supplemental Material



**Supplemental Figure: 2P-STED imaging of dendrites and spines deep inside acute hippocampal slices** Comparison of 2P and 2P-STED images of dendrites in the CA1 region of an acute hippocampal slice acquired at 48.5  $\mu\text{m}$  imaging depth below tissue surface. Spine neck widths were measured as indicated.

---

## **Additional results**

### **Morphological dynamics of CA3 axons during LTD**

We found that LTP modulates the axonal morphology by overall increasing the diameter of the axonal shafts. We also investigated whether LTD (i.e. functional counterpart of LTP) that leads to synaptic depression could also produce a directional change in the axonal morphology and examine whether the morphological effect observed on the axons during LTP depended on the type of electrical stimulation and the direction of synaptic plasticity. Indeed, the application of LFS (900 pulses, 1 Hz), which reliably induced LTD (Figure 14a), led to a small but statistically significant decrease in the diameter of CA3 axon shafts coinciding with the LTD induction phase. However, the effect was only short-lived and the axon diameters recovered at 45 minutes after LFS (Figure 14b). In addition, no morphological change was observed on boutons (Figure 14c).

These results indicate that LTD leads to a different type of morphological change on axon whereby the axon shaft diameters transiently decrease after LFS and recover later. The morphological dynamics of CA3 axons is specific to the type of stimulation and synaptic plasticity.

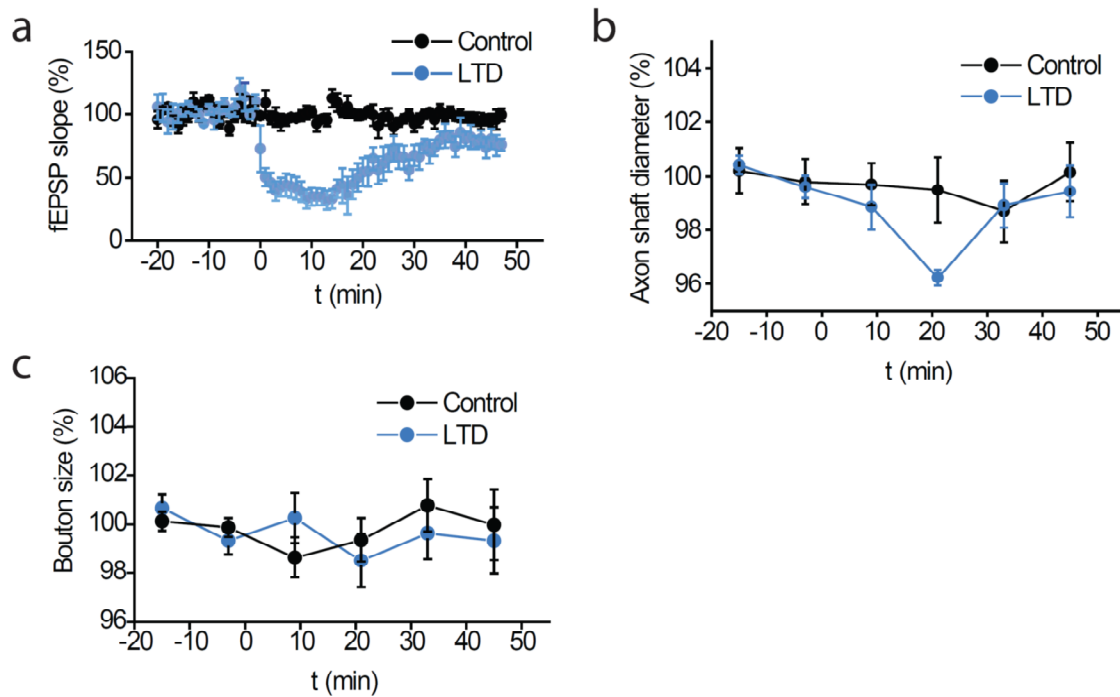


**Figure 14: Structural plasticity of axon shafts and boutons during LTD.**

(a) Average time course of the fEPSP slope (normalized to baseline) during LTD induction (blue; average depression at 30-40 minutes post-induction  $24 \pm 6\%$  of baseline,  $n=4$ ). The recordings were stable in control conditions (black,  $n=7$ ); mean  $\pm$  SEM shown.

(b) Normalized axon shaft diameter during LTD (blue) shows a transient decrease at 21 minutes after induction ( $n=4$ ) over the control condition (black,  $n=7$ ); mean  $\pm$  SEM shown.

(c) Normalized bouton size dynamics during LTD (Control, black,  $n=101$ ; 7 experiments; LTD, blue,  $n=65$ ; 4 experiments); mean  $\pm$  SEM shown.

### Characterization of the FWHM measurement

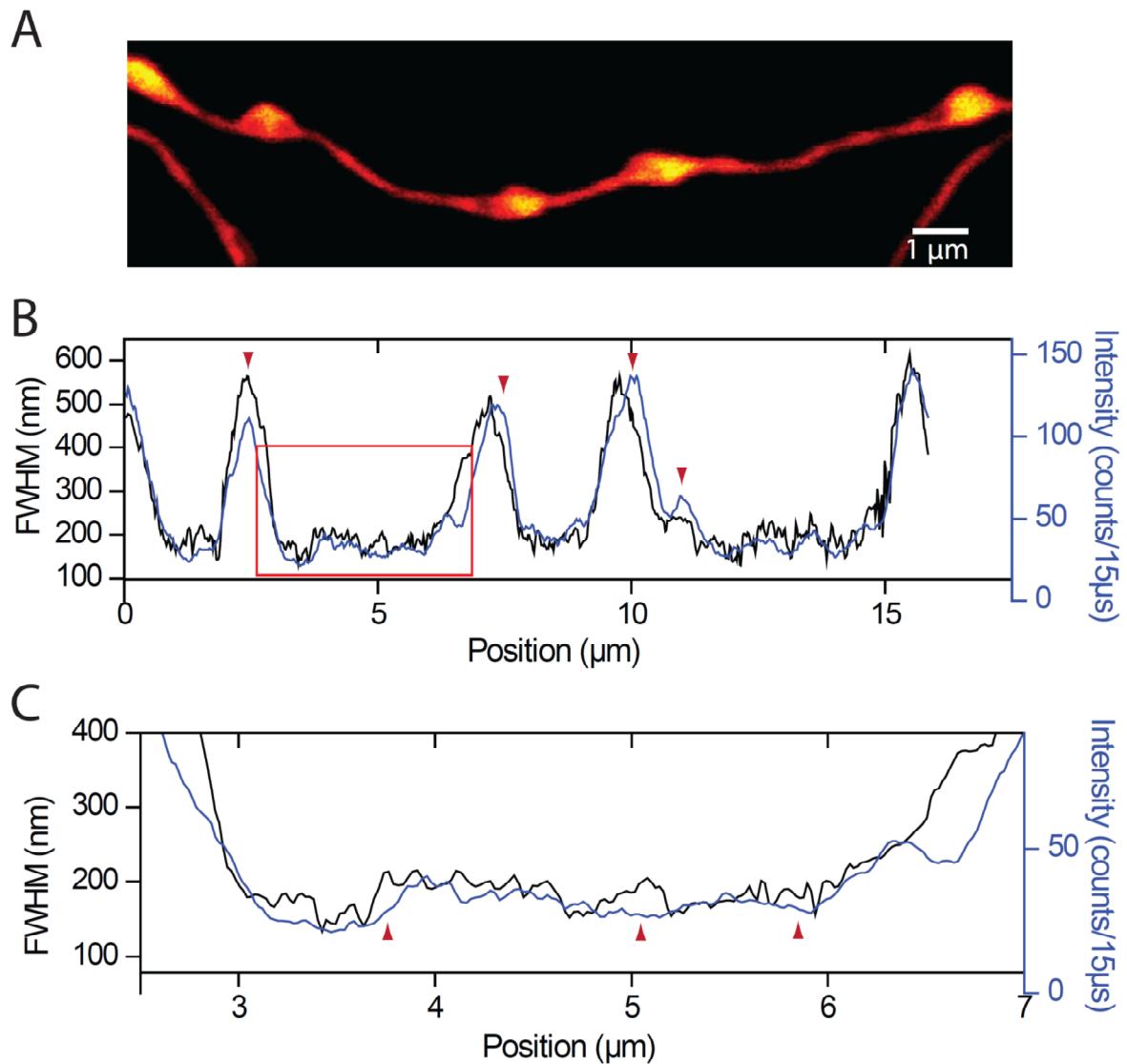


**Figure 15: The inhomogeneous distribution of fluorophores in the axon structure makes intensity-based measurement of diameters inaccurate.**

(A) STED image of an axon acquired in the CA1 stratum radiatum. (B, C) Comparison between the FWHM measurement (black) and estimation of the axon diameter based on the relative change of intensity (blue). The red arrows points to the large difference observed on the boutons (B) and on the shaft (C).

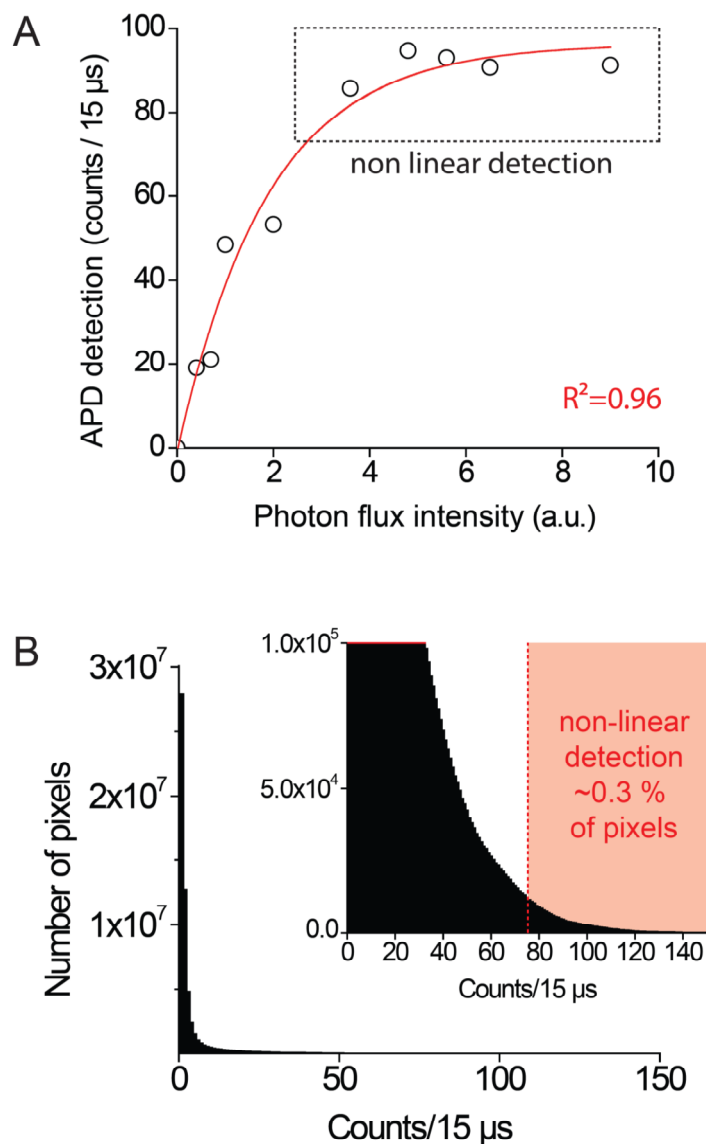


**Figure 16: The imaging of axonal structures was performed in non-saturated conditions.**

(A) Plot representing the number of counts performed by the APD detector increasing the flux of photons (a low power green diode was used as a light source). The data is well fitted by a exponential curve ( $R^2=0.96$ ; red line). The detection starts to be highly non-linear after 75 counts in 15  $\mu$ s (black dotted rectangle). (B) Histogram of intensity distribution from 10 representative imaging sessions (30x20x3  $\mu$ m maximum intensity projections, containing 6 timepoints each, pulled together acquired with a 15  $\mu$ s dwell time). The inset shows the expanded y-axis scale showing that less than 0.3% of the pixels are detected non-linearly.

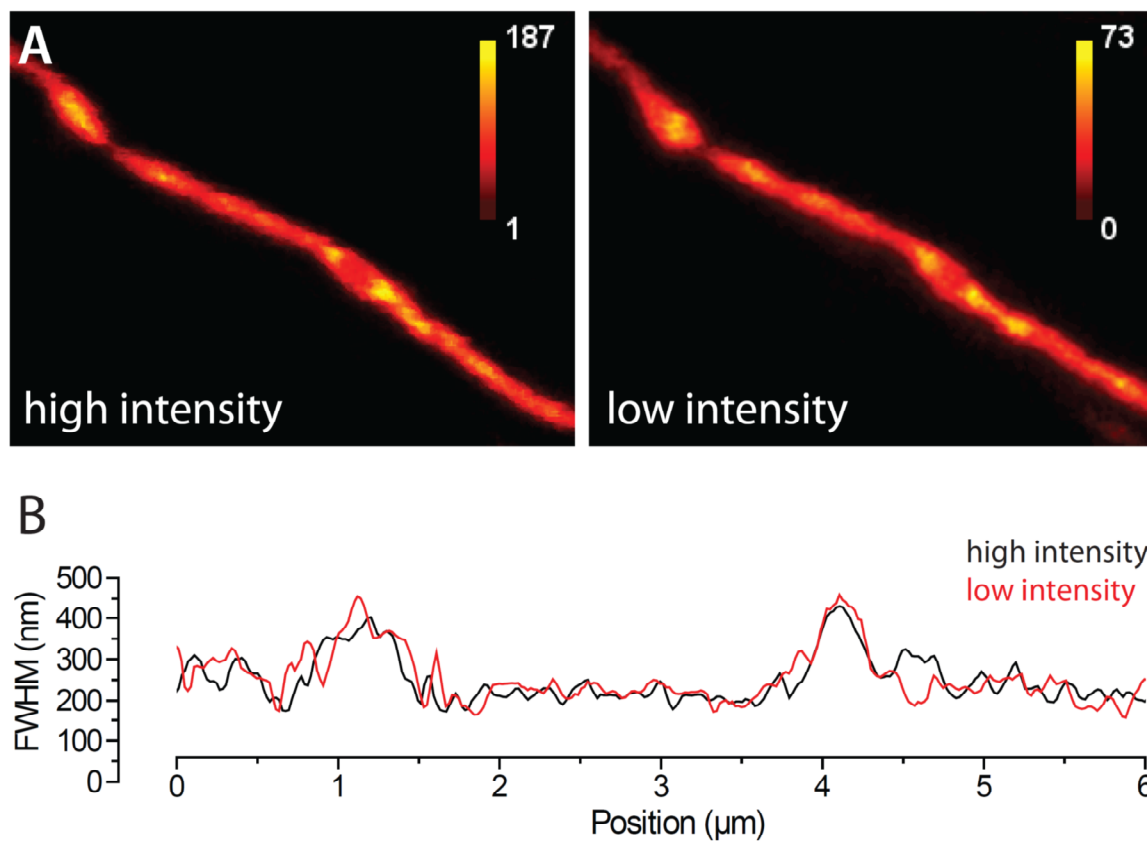


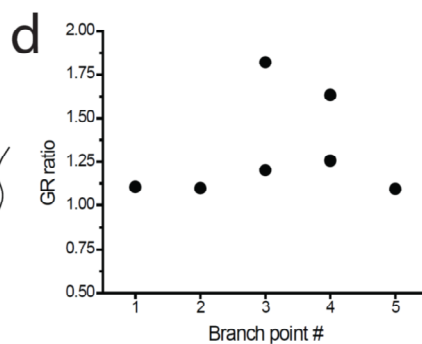
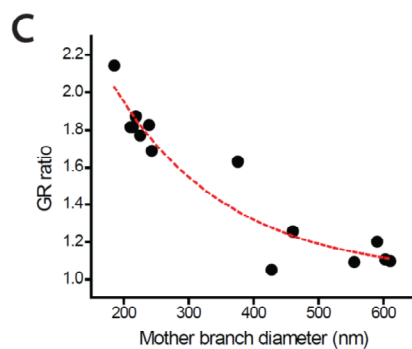
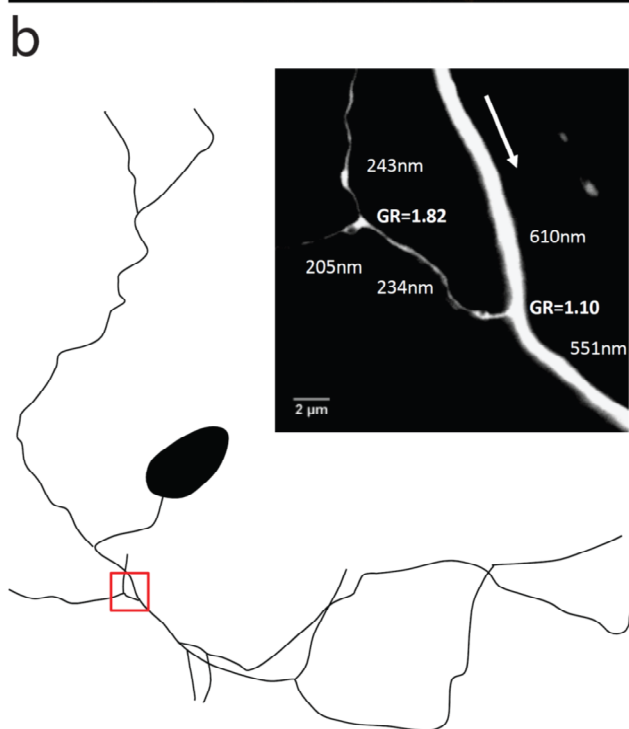
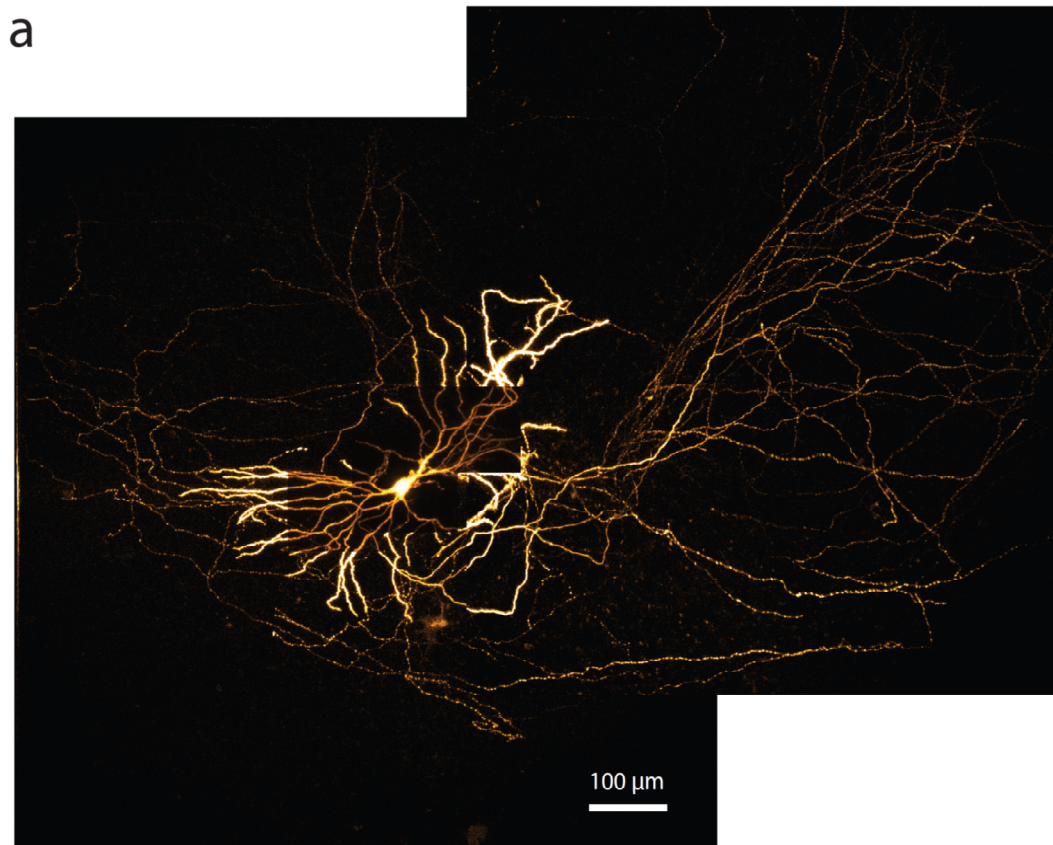
**Figure 17: The FWHM measurement does not depend on the intensity of the signal.**

(A) STED images from the same axon stretch acquired with high and low excitation power in a living sample. The scale of pixel intensities is represented in the top right corner. (B) Comparison of the FWHM measurement along the axon stretch shown in A. The two profiles are very similar and highlight the independence of the measurement from the fluorescence intensity of the structure. The slight differences observed denote the dynamic fluctuations of the structure.

---

### **Topological organization of CA3 axon trees**

The rules whereby an AP propagates through a complex unmyelinated axonal arborization are still elusive. When some studies show that once initiated, APs reliably reach their presynaptic targets (Cox et al, 2000; Hu & Jonas, 2014), others indicate that geometric constrains might alter propagation and even produce conduction failures (Goldstein & Rall, 1974; Luscher et al, 1994). Branch points represent a biophysical constrain that may alter this propagation. A large geometrical ratio (GR) calculated between the cross sectional diameter of a mother branch and its two daughter branches can serve as an indication to predict if AP may slow down passing through branch point or even fail to propagate in one of the daughter branches. Preliminary results show that due to large diameters the GR ratio is often close to 1 in the proximal part of the arborization and substantially increase in the distal part of the axon when the collaterals are much thinner (Figure 18). These data indicate the proximal part of the tree should conduct APs reliably whereas it could be altered in the distal region. Further investigations will be required to determine whether rules of propagation are different between the proximal and distal part of the axon.



---

**Figure 18: Geometric ratio measurement on the proximal axon tree.**

(a) *Confocal image of a GFP-labeled CA3 pyramidal neuron by single-cell Sindbis-GFP viral infection. The axon branches extensively and contacts local CA3 neurons (axon around the dendritic tree) and CA1 neurons (extensions on the right part of the image).*

(b) *Tracing of the proximal part of the axon and STED image corresponding to the region shown in the schematic (red square). Axon diameters and calculated geometric ratio (GR) are shown. The arrow indicated the direction of orthodromic AP propagation.*

(c) *GR ratio as a function of the mother branch diameter.*

(d) *GR ratio as a function of the branch point order.*

## DISCUSSION

Our current view of the axon compartment has considerably changed in the last few years. As advanced electrophysiological and imaging techniques have emerged, interesting properties on axon physiology have been discovered (Ganguly et al, 2000; Geiger & Jonas, 2000; Grubb & Burrone, 2010; Kuba et al, 2010; Sasaki et al, 2011; Sasaki et al, 2012a). Even though it is now well established that important structural modifications occur presynaptically during neuronal activity (Bastrikova et al, 2008; Becker et al, 2008; Bourne et al, 2013), it is less clear whether the structure of the axon proper undergoes structural changes that might affect its functions.

While EM studies have exquisitely described geometry and ultrastructure of unmyelinated axons of principal neurons in fixed preparations, little is known about their dynamics in living tissue. Limited by the diffraction of light, conventional light microscopy has failed to study their dynamics at the nanoscale hence calling for a novel imaging approach. The development of superresolution STED microscopy, overcoming light diffraction limit and providing an optical resolution down to 50 nm, bridges this gap allowing for live observations of these hyperthin structures.

### **Summary of the findings**

In this study, we report a new type of plasticity whereby axons can dynamically modulate their diameters hence changing its properties for the propagation of APs. We combined STED imaging and electrophysiology in live brain tissue and computer simulations to investigate the activity-dependent dynamics of axons. We found that HFS-induced LTP leads to a persistent increase of axon shaft diameters that is largely repressed when the LTP expression is pharmacologically prohibited. In addition, we observed that boutons swell

transiently shortly after the HFS stimulus, thus, increasing the morphological irregularity of the structure. Extracting conduction latencies from antidromically propagating APs, we show that AP conduction velocity is altered by the induction of LTP with an initial slowing down followed by a persistent increase of the velocity during the establishment of LTP. These data strongly corroborate what was observed in superresolution imaging experiments, hence confirmed by simulation models using our acquired morphological data.

Knowing now that the geometry of axons can be modulated by activity raises many new questions to understand the causes and the consequences for the physiology of the neuron and the impact on the neuronal circuitry and network behaviour.

### **Effect of structural factors on AP propagation**

There are two structural mechanisms employed by axons that warrant fast AP propagation. One of the strategies, largely used by invertebrates, is to set up large axon diameters. For instance, the well studied squid giant axon has a typical 0.5 mm cross sectional diameter and can conduct AP at 25 m/s. Myelination, specific to vertebrates, insulate axons and ensure fast propagation through saltatory conduction. None of those strategies are used by CA3 axons in the hippocampus where axon diameters range around 200 nm and myelination is absent (Ishizuka et al, 1990; Meeks et al, 2005; Shepherd & Harris, 1998; Soleng et al, 2003a; Westrum & Blackstad, 1962). Hence, APs are conducted slowly, increasing the importance of the topological organization of the synaptic targets which will receive the information with a variable temporal delay. Do the differences in axonal latencies influence hippocampal function?

First, regarding that some hippocampal rhythms such as gamma (20-70 Hz) and ripples waves (140-200 Hz) are very fast, the synchronization within a millisecond might be important. Gamma oscillations are known to be important for exploratory behaviour and

sharp wave ripples play a role in memory consolidation during rest. Those network rhythms have to be extremely precise and utterly depend on neuronal connectivity, therefore axonal delays could substantially modify those oscillation patterns. Second and partially related to the first argument, few milliseconds difference may be critical in the context of disynaptic inhibitory signals. Third, in the context of STDP, excitatory synapses are either potentiated or depressed in a time window of 10-20 ms which reflects the maximal supralinear calcium summation between dendritic spike and synaptic event.

### **Morpho-functional changes on axons depend on LTP induction**

In this study we found that the axonal structure was sensitive to the HFS-induced LTP. This type of stimulation protocol has been widely used in the literature to explore and unravel synaptic plasticity mechanisms at CA3-CA1 synapses. While postsynaptic NMDA receptors are an established mediator of the expression of LTP, there are also indications for either direct or indirect structural and functional modifications on the presynaptic element. Indeed, some studies suggest that the functions of the pre- and postsynaptic elements are enhanced in a well coordinated fashion (Lauri et al, 2007). Following a fast postsynaptic potentiation, a slow presynaptic component was shown to appear during LTP (Bayazitov et al, 2007). It consists in the enhancement of the release probability of vesicles and depends on the activation of L-type voltage-gated calcium channels. Furthermore, it has been shown that LTP induction enhances presynaptic neuronal excitability (Ganguly et al, 2000; Li et al, 2004).

Even though there is an extensive literature on the postsynaptic morphological changes, little is known about the structural modifications on axons during LTP. Recent studies revealed that the number of synaptic vesicles was persistently reduced after LTP induction (Bourne et

al, 2013) and that bouton sizes increase following glutamate uncaging protocols to strengthen synapses (Meyer et al, 2014).

In our experiments, we partially but not fully blocked the increase of axon shaft diameter when LTP was blocked by the NMDAR antagonist APV, although we did not observe a reduction of AP latencies. Knowing that NMDA receptors are present at the axon membrane (Li et al, 2004; Pina-Crespo & Gibb, 2002; Siegel et al, 1994), we can hypothesize that the blockade of axonal NMDA receptors during HFS could either reduce axonal membrane excitability.

### **Putative mechanisms axon structural plasticity**

We can emit several hypotheses that could explain the dynamic modulation and more specifically the enlargement of axons during HFS-induced LTP. Some would involve mechanical tension of the plasma membrane and others involve dynamic redistribution of membrane.

The recent discovery of unique cytoskeleton architecture of the axon proper triggers the imagination for novel axonal properties (Xu et al, 2013). The actin rings displayed along the axon and periodically spacing every 180-190 nm with an incredible accuracy raise new questions. First being: are those rings regulated by activity? In the case of our study, we could assume that the global axon enlargement is the consequence of the modulation of those actin rings. Every ring could be seen as a tunable pattern imposing a form on the axon that could both modulate its electrical and biochemical compartmentalization.

A possible scenario involves the release machinery of presynaptic boutons. Even though we have a good understanding of the molecular and structural determinants of neurotransmitter release through the fusion of vesicles at the plasma membrane, it is not yet clear how the presynaptic compartment deals with this membrane dynamics. We wondered whether the

source of membrane producing the enlargement of axons could come from neurotransmitter vesicles. A strong argument supporting this hypothesis comes from recent studies. First of all, *in vivo* studies have clearly shown that the number of presynaptic vesicles in boutons scales with the surface area of the postsynaptic density (Harris & Stevens, 1989; Harris & Sultan, 1995; Lisman & Harris, 1993; Schikorski & Stevens, 2001). Since the postsynaptic density size increases with LTP, one could assume that the number of vesicles increases as well. Although, early EM observations from single section analyses suggested that the number of presynaptic vesicles was reduced after induction of LTP (Applegate et al, 1987; Fifkova & Van Harreveld, 1977; Meshul & Hopkins, 1990). This was recently confirmed through 3D reconstructions from serial EM sections revealing a strong depletion of about 100 vesicles out of 300 in average, 30 minutes and 2 hours after LTP induction (Bourne et al, 2013). Thus, one could suspect that this depletion of vesicles represents the source of membrane that contributes to the overall increase of axon diameter.

Knowing that the size of a vesicle is about 40 nm in diameter, and on average, the axon structure is composed of an axon shaft of 200 nm and displays oblong-shaped boutons of 1  $\mu\text{m}$  long and 500 nm large with a frequency of 3  $\mu\text{m}$  along the axon; the exocytosis of 100 vesicles per bouton would yield an average axonal diameter increase of  $\sim 20\%$ . Performing the reverse calculation from a 5-7% increase in axonal diameter observed in our study, we could estimate a depletion of about 20-30 vesicles in average per bouton. This difference with the study from Bourne et al. might be due to the type of preparation and stimulation employed therefore giving different probability of vesicular release during HFS and bulk endocytosis mechanisms following exocytosis (Bourne et al, 2013).

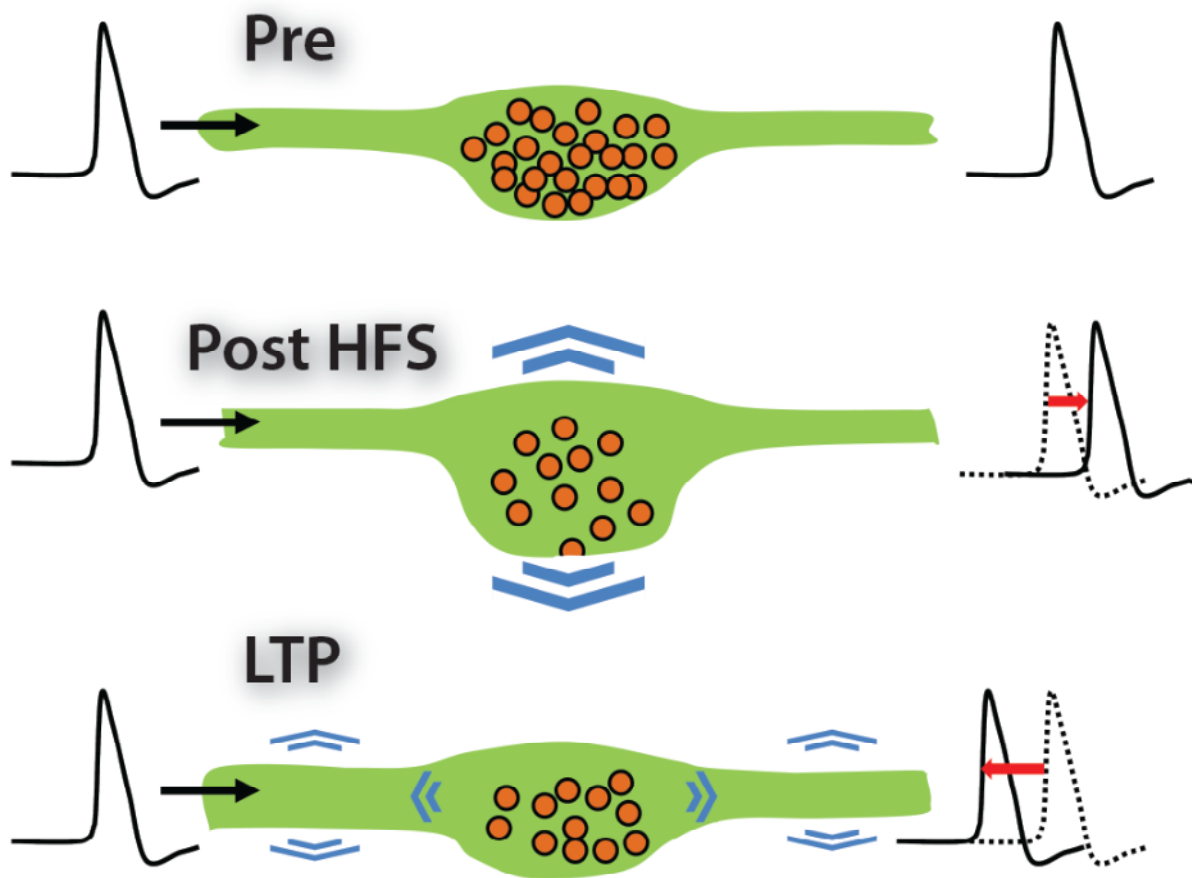


**Figure 19: Proposed mechanism of axonal diameter enlargement.**

*High-frequency stimulation of axons promotes the exocytosis of neurotransmitter release in the presynaptic element leading to an increase in the size of the bouton. This makes the overall axonal structure more irregular hence slowing down AP conduction velocity. The excess of membrane in boutons subsequently diffuses in the adjacent axon shaft enlarging its cross sectional diameter concomitantly with LTP induction. In consequence, larger axon diameter and fewer irregularities lead to faster propagation of APs.*

The release probability at hippocampal synapses was shown to be highly heterogeneous and positively correlates with bouton volume and active zone area (Holderith et al, 2012). This parameter is also non-linear with the frequency of stimulation. Typically, HFS produces a facilitation quickly followed by a depletion of the readily-releasable pool (Dobrunz, 2002; Dobrunz & Stevens, 1997). Considering the stimulus protocol employed in our study (3 times

1 second at 100 Hz) and taking a conservative estimate of the release probability at single boutons of 0.2 in average (Dobrunz, 2002; Hanse & Gustafsson, 2001; Holderith et al, 2012), an average of 60 vesicles have fused to every boutons on the axon during the stimulation.

In addition, a recent study brought the evidence that exocytosis of neurotransmitter was followed by rapid bulk endocytosis within 50-100 ms (Watanabe et al, 2013) which means that a part of the membrane coming from the 60 vesicles calculated would be endocytosed. Altogether, this scenario involving a net change in the number of vesicles after LTP could explain the overall increase axon diameter (Figure 19).

### **Functional impact of axonal AP velocity modulation on information processing in the brain**

The timing of signal transmission between neurons in the hippocampus can be substantial but is most of the time ignored in computational studies. This delay in transmission is generally described as the sum of axonal conduction that depends on the conduction velocity, the axonal length, and the synaptic delay.

In that regard, CA3 axons conduct APs relatively slowly (0.37 m/s (Meeks et al, 2005); 0.2 m/s (Soleng et al, 2003b)) because there are thin, irregular and unmyelinated ((Ishizuka et al, 1990; Meeks et al, 2005; Shepherd & Harris, 1998; Soleng et al, 2003a; Westrum & Blackstad, 1962). In addition, an in vivo reconstruction of a full CA3 axon arborisation in the rat revealed that some of its collaterals can extend up to 20 mm (Wittner et al, 2007). Therefore, propagation times in axons can be as long as 100 ms.

In our study, we observed a consistent change in the population of axons measured. However, STED microscopy limits the imaging to a set of axon stretches in a relatively small field of view (~ 30 x 20 $\mu$ m). Therefore, we cannot rule out that the increase of diameter is homogenous throughout the axon arborisation. But, assuming that the change is global, the

acceleration of the conduction could shorten the AP arrival time by a few milliseconds in the distal axon (Figure 20). There is evidence that milliseconds time difference would have a significant impact on several hippocampal functions. First, some hippocampal rhythms such as gamma (20-70 Hz) and ripples (140-200 Hz) are very fast and suggest that sub-milliseconds synchronization may be important. Second, delays of propagation are crucial in the context of spike-timing dependent plasticity (STDP). The time window for supralinear summation of calcium caused by dendritic spikes and synaptic events is on the milliseconds scale and determines whether synapses are potentiated or depressed. Knowing that STDP is responsible for the formation of synchronized groups of neurons that are strongly interconnected, a slight change in axonal delay could remodel those polysynchronous groups (Izhikevich, 2006). Third, a few milliseconds change in delay of propagation could largely alter the disynaptic inhibition of the postsynaptic neuron.

Thus, it will be interesting to evaluate whether axon geometry-dependent variations in AP delay further increase storage capacity.

In addition to the modulation of AP propagation properties, it would be interesting to investigate whether structural modifications of axon morphology are reflected in a change in diffusive properties which would impact axonal transport.

## **Outlook**

This work, going along with recent discoveries, outline more generally that the computational power of axons and their functional impact has been largely underestimated. In biology, it is considered that the level of structural complexity scales with the diversity of functions. In that regard, both the diversity of the large scale organization of axonal trees, the ultrastructural organization of the axon trunk and presynaptic boutons gives us as many indications for a variety of functions that remains to be discovered.

For instance, by picturing the complexity of axon arborisations in the hippocampus (Major et al, 1994; Wittner et al, 2007), emerging ideas supported by biophysical principles are challenging the view that APs have a smooth ride from the soma to the presynaptic targets. The highly collateralized organization and the presence of many varicose en passant boutons may substantially decrease conduction speed and could even lead to failure of propagation. It would be interesting to see whether in non-pathological conditions, axons use such mechanism to control APs propagation in an arborisation. One could imagine that every branch points within a tree would act as a gate for allowing or blocking the passage of an AP. This failure of AP propagation was suggested many times (Bucher & Goillard, 2011; Debanne, 2004; Debanne et al, 2011) and experimentally shown, but only in specific conditions (Luscher et al, 1994; Manor et al, 1991).

Another aspect to consider is that the axonal protrusion can be very isolated biochemically and electrically from the neuronal cell body. For some cell types, axons can extend up to several meters making any signalling from the soma a very slow and non-reliable process. It is then likely that the distal axon would be largely influenced by local signalling from its glial environment. This concept has emerged recently with two studies from the same group. One of those studies demonstrated that the distal part of the axon is electrically isolated as compared to the proximal part (Sasaki et al, 2012a). The other shows the influence of astrocytes on the local regulation of AP propagation (Sasaki et al, 2011).

### **Concluding remarks**

In conclusion, this work serves us with novel indicators that beyond the classical scope of AP propagation, axons are capable of many structural rearrangements for the plasticity of neuronal circuitry.

We showed that the morphology with both the irregularity of the structure and the average diameter can be directly modulated by neuronal activity. Biophysical theory, computer simulations as well as electrophysiological recordings indicate that changes in AP conduction velocity are the direct result of structural changes in the axons.

The emergence of new technologies and the conceptual refinement about axonal properties will help to discover many interesting facets of axon physiology and unravel its significance for neural computations.

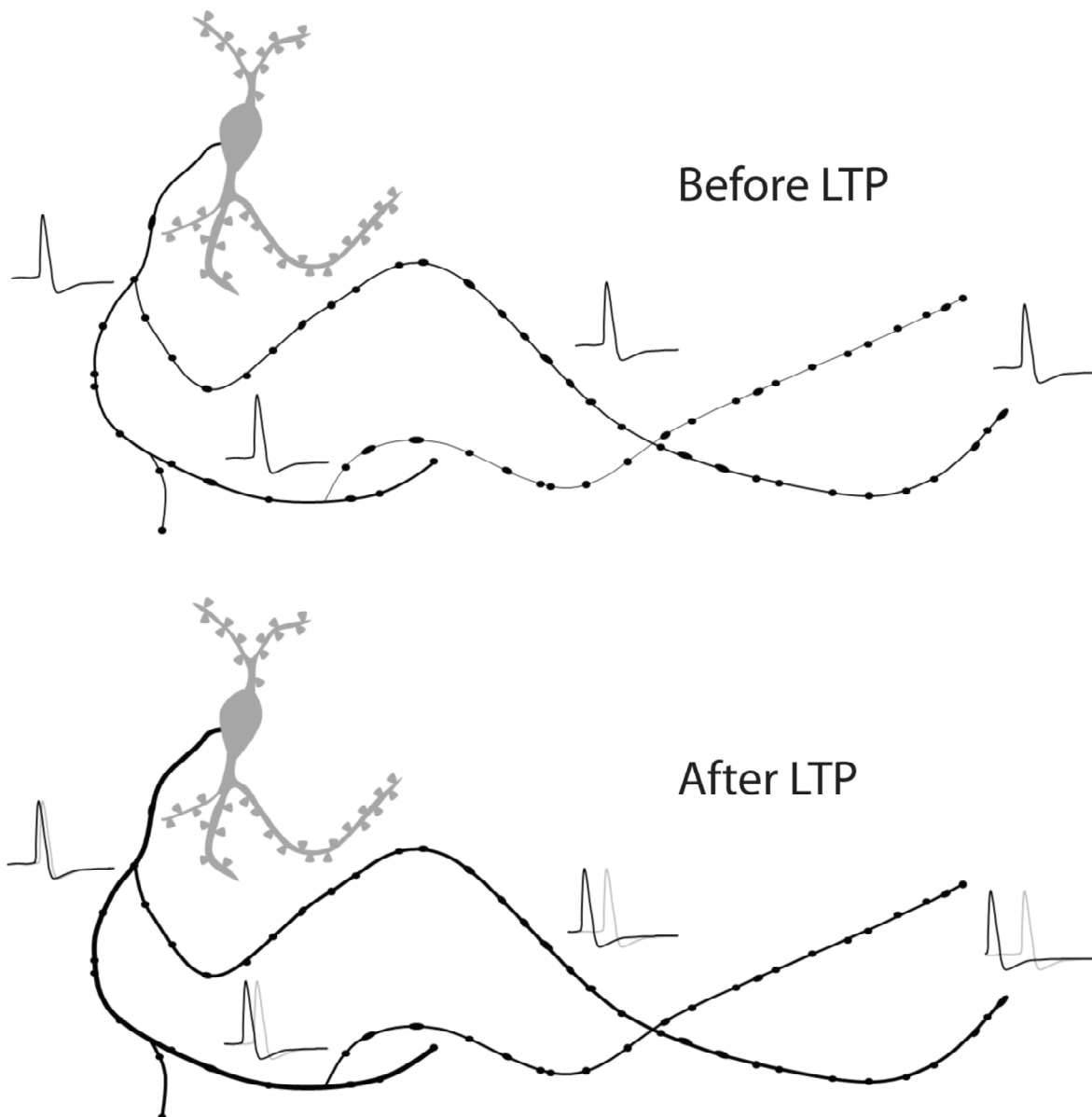


**Figure 20: Hippocampal axons may serve as dynamic delay lines for information transfer.**

*The activity-dependent modulation of axonal geometry leading to a change in conduction delay could represent a novel type of plasticity whereby axons could control delays of transmission impacting several important functions in the hippocampus.*

---

## REFERENCES

1. Andersen P, Morris, R., Amaral, D., Bliss T., O'Keefe, J. (2007) *The Hippocampus Book*.
2. Andersen P, Soleng AF, Raastad M (2000) The hippocampal lamella hypothesis revisited. *Brain Res* **886**: 165-171
3. Andersen P, Trommald M, Jensen V (1994) Low synaptic convergence of CA3 collaterals on CA1 pyramidal cells suggests few release sites. *Adv Second Messenger Phosphoprotein Res* **29**: 340-351
4. Applegate MD, Kerr DS, Landfield PW (1987) Redistribution of synaptic vesicles during long-term potentiation in the hippocampus. *Brain Res* **401**: 401-406
5. Baker MD, Bostock H (1997) Low-threshold, persistent sodium current in rat large dorsal root ganglion neurons in culture. *J Neurophysiol* **77**: 1503-1513
6. Bakkum DJ, Chao ZC, Potter SM (2008) Long-term activity-dependent plasticity of action potential propagation delay and amplitude in cortical networks. *PLoS One* **3**: e2088
7. Bastrikova N, Gardner GA, Reece JM, Jeromin A, Dudek SM (2008) Synapse elimination accompanies functional plasticity in hippocampal neurons. *Proc Natl Acad Sci U S A* **105**: 3123-3127
8. Bayazitov IT, Richardson RJ, Fricke RG, Zakharenko SS (2007) Slow presynaptic and fast postsynaptic components of compound long-term potentiation. *J Neurosci* **27**: 11510-11521
9. Becker N, Wierenga CJ, Fonseca R, Bonhoeffer T, Nagerl UV (2008) LTD induction causes morphological changes of presynaptic boutons and reduces their contacts with spines. *Neuron* **60**: 590-597
10. Bender KJ, Ford CP, Trussell LO (2010) Dopaminergic modulation of axon initial segment calcium channels regulates action potential initiation. *Neuron* **68**: 500-511
11. Bender KJ, Trussell LO (2009) Axon initial segment Ca<sup>2+</sup> channels influence action potential generation and timing. *Neuron* **61**: 259-271
12. Bender KJ, Trussell LO (2012) The physiology of the axon initial segment. *Annu Rev Neurosci* **35**: 249-265
13. Bender KJ, Uebele VN, Renger JJ, Trussell LO (2012) Control of firing patterns through modulation of axon initial segment T-type calcium channels. *J Physiol* **590**: 109-118
14. Bi G, Poo M (2001) Synaptic modification by correlated activity: Hebb's postulate revisited. *Annu Rev Neurosci* **24**: 139-166

- 
15. Bliss TV, Lomo T (1973) Long-lasting potentiation of synaptic transmission in the dentate area of the anaesthetized rabbit following stimulation of the perforant path. *J Physiol* **232**: 331-356
  16. Bolshakov VY, Siegelbaum SA (1995) Regulation of hippocampal transmitter release during development and long-term potentiation. *Science* **269**: 1730-1734
  17. Bostock H, Rothwell JC (1997) Latent addition in motor and sensory fibres of human peripheral nerve. *J Physiol* **498** ( Pt 1): 277-294
  18. Bourne JN, Chirillo MA, Harris KM (2013) Presynaptic ultrastructural plasticity along CA3-->CA1 axons during long-term potentiation in mature hippocampus. *J Comp Neurol* **521**: 3898-3912
  19. Bredt DS, Nicoll RA (2003) AMPA receptor trafficking at excitatory synapses. *Neuron* **40**: 361-379
  20. Breustedt J, Vogt KE, Miller RJ, Nicoll RA, Schmitz D (2003) Alpha1E-containing Ca<sup>2+</sup> channels are involved in synaptic plasticity. *Proc Natl Acad Sci U S A* **100**: 12450-12455
  21. Brunig I, Scotti E, Sidler C, Fritschy JM (2002) Intact sorting, targeting, and clustering of gamma-aminobutyric acid A receptor subtypes in hippocampal neurons in vitro. *J Comp Neurol* **443**: 43-55
  22. Bucher D, Goillard JM (2011) Beyond faithful conduction: short-term dynamics, neuromodulation, and long-term regulation of spike propagation in the axon. *Prog Neurobiol* **94**: 307-346
  23. Bullock TH (1951) Facilitation of conduction rate in nerve fibers. *J Physiol* **114**: 89-97
  24. Burke SP, Adams ME, Taylor CP (1993) Inhibition of endogenous glutamate release from hippocampal tissue by Ca<sup>2+</sup> channel toxins. *Eur J Pharmacol* **238**: 383-386
  25. Byrne JH, Kandel ER (1996) Presynaptic facilitation revisited: state and time dependence. *J Neurosci* **16**: 425-435
  26. Campanac E, Daoudal G, Ankri N, Debanne D (2008) Downregulation of dendritic I(h) in CA1 pyramidal neurons after LTP. *J Neurosci* **28**: 8635-8643
  27. Campanac E, Debanne D (2007) Plasticity of neuronal excitability: Hebbian rules beyond the synapse. *Arch Ital Biol* **145**: 277-287
  28. Carnevale NT, Hines ML (eds) (2006) *The NEURON Book*: Cambridge, UK: Cambridge University Press
  29. Castillo PE (2012) Presynaptic LTP and LTD of excitatory and inhibitory synapses. *Cold Spring Harb Perspect Biol* **4**

- 
30. Cesca F, Baldelli P, Valtorta F, Benfenati F (2010) The synapsins: key actors of synapse function and plasticity. *Prog Neurobiol* **91**: 313-348
  31. Chklovskii DB, Mel BW, Svoboda K (2004) Cortical rewiring and information storage. *Nature* **431**: 782-788
  32. Choi S, Klingauf J, Tsien RW (2000) Postfusional regulation of cleft glutamate concentration during LTP at 'silent synapses'. *Nat Neurosci* **3**: 330-336
  33. Christie SB, De Blas AL (2003) GABAergic and glutamatergic axons innervate the axon initial segment and organize GABA(A) receptor clusters of cultured hippocampal pyramidal cells. *J Comp Neurol* **456**: 361-374
  34. Cobb SR, Buhl EH, Halasy K, Paulsen O, Somogyi P (1995) Synchronization of neuronal activity in hippocampus by individual GABAergic interneurons. *Nature* **378**: 75-78
  35. Cole KS, Curtis HJ (1939) Electric Impedance of the Squid Giant Axon during Activity. *J Gen Physiol* **22**: 649-670
  36. Cooke SF, Bliss TV (2006) Plasticity in the human central nervous system. *Brain* **129**: 1659-1673
  37. Cox CL, Denk W, Tank DW, Svoboda K (2000) Action potentials reliably invade axonal arbors of rat neocortical neurons. *Proc Natl Acad Sci U S A* **97**: 9724-9728
  38. Dayan P, Abbott LF (eds) (2001) *Theoretical neuroscience: computational and mathematical modeling of neural systems*: Cambridge, MA: Massachusetts Institute of Technology
  39. De Paola V, Holtmaat A, Knott G, Song S, Wilbrecht L, Caroni P, Svoboda K (2006) Cell type-specific structural plasticity of axonal branches and boutons in the adult neocortex. *Neuron* **49**: 861-875
  40. Debanne D (2004) Information processing in the axon. *Nat Rev Neurosci* **5**: 304-316
  41. Debanne D, Campanac E, Bialowas A, Carlier E, Alcaraz G (2011) Axon physiology. *Physiol Rev* **91**: 555-602
  42. Debanne D, Daoudal G, Sourdet V, Russier M (2003) Brain plasticity and ion channels. *J Physiol Paris* **97**: 403-414
  43. Debanne D, Poo MM (2010) Spike-timing dependent plasticity beyond synapse - pre- and post-synaptic plasticity of intrinsic neuronal excitability. *Front Synaptic Neurosci* **2**: 21
  44. Deiters O (1865) Untersuchungen über Gehirn und Rückenmark des Menschen und der Säugethiere. *Braunschweig: Vieweg*
  45. Del Castillo J, Moore JW (1959) On increasing the velocity of a nerve impulse. *J Physiol* **148**: 665-670

- 
46. Dietrich D, Kirschstein T, Kukley M, Pereverzev A, von der Brélie C, Schneider T, Beck H (2003) Functional specialization of presynaptic Cav2.3 Ca<sup>2+</sup> channels. *Neuron* **39**: 483-496
  47. Dobrunz LE (2002) Release probability is regulated by the size of the readily releasable vesicle pool at excitatory synapses in hippocampus. *Int J Dev Neurosci* **20**: 225-236
  48. Dobrunz LE, Stevens CF (1997) Heterogeneity of release probability, facilitation, and depletion at central synapses. *Neuron* **18**: 995-1008
  49. Ehrengruber MU, Lundstrom K, Schweitzer C, Heuss C, Schlesinger S, Gähwiler BH (1999) Recombinant Semliki Forest virus and Sindbis virus efficiently infect neurons in hippocampal slice cultures. *Proc Natl Acad Sci U S A* **96**: 7041-7046
  50. Emptage NJ, Reid CA, Fine A, Bliss TV (2003) Optical quantal analysis reveals a presynaptic component of LTP at hippocampal Schaffer-associational synapses. *Neuron* **38**: 797-804
  51. Engelman HS, MacDermott AB (2004) Presynaptic ionotropic receptors and control of transmitter release. *Nat Rev Neurosci* **5**: 135-145
  52. Fifkova E, Van Harreveld A (1977) Long-lasting morphological changes in dendritic spines of dentate granular cells following stimulation of the entorhinal area. *J Neurocytol* **6**: 211-230
  53. Foust A, Popovic M, Zecevic D, McCormick DA (2010) Action potentials initiate in the axon initial segment and propagate through axon collaterals reliably in cerebellar Purkinje neurons. *J Neurosci* **30**: 6891-6902
  54. French CR, Sah P, Buckett KJ, Gage PW (1990) A voltage-dependent persistent sodium current in mammalian hippocampal neurons. *J Gen Physiol* **95**: 1139-1157
  55. Frick A, Magee J, Johnston D (2004) LTP is accompanied by an enhanced local excitability of pyramidal neuron dendrites. *Nat Neurosci* **7**: 126-135
  56. Gähwiler BH (1987) Organotypic slice cultures: a model for interdisciplinary studies. *Prog Clin Biol Res* **253**: 13-18
  57. Gähwiler BH, Capogna M, Debanne D, McKinney RA, Thompson SM (1997) Organotypic slice cultures: a technique has come of age. *Trends Neurosci* **20**: 471-477
  58. Ganguly K, Kiss L, Poo M (2000) Enhancement of presynaptic neuronal excitability by correlated presynaptic and postsynaptic spiking. *Nat Neurosci* **3**: 1018-1026
  59. Gasser HS, Grundfest H (1939) Axon diameters in relation to the spike dimensions and the conduction velocity in mammalian A fibers. *American Journal of Physiology* **127(2)**: 393-414

- 
60. Geer JJ, Dooley DJ, Adams ME (1993) K(+)-stimulated  $^{45}\text{Ca}^{2+}$  flux into rat neocortical mini-slices is blocked by omega-Aga-IVA and the dual  $\text{Na}^{+}/\text{Ca}^{2+}$  channel blockers lidoflazine and flunarizine. *Neurosci Lett* **158**: 97-100
  61. Geiger JR, Jonas P (2000) Dynamic control of presynaptic  $\text{Ca}^{2+}$  inflow by fast-inactivating K(+) channels in hippocampal mossy fiber boutons. *Neuron* **28**: 927-939
  62. Goldin AL (2002) Evolution of voltage-gated  $\text{Na}^{+}$  channels. *J Exp Biol* **205**: 575-584
  63. Goldstein SS, Rall W (1974) Changes of action potential shape and velocity for changing core conductor geometry. *Biophys J* **14**: 731-757
  64. Gong B, Rhodes KJ, Bekele-Arcuri Z, Trimmer JS (1999) Type I and type II  $\text{Na}^{+}$  channel alpha-subunit polypeptides exhibit distinct spatial and temporal patterning, and association with auxiliary subunits in rat brain. *J Comp Neurol* **412**: 342-352
  65. Greenberg MM, Leitao C, Trogadis J, Stevens JK (1990) Irregular geometries in normal unmyelinated axons: a 3D serial EM analysis. *J Neurocytol* **19**: 978-988
  66. Grieco TM, Malhotra JD, Chen C, Isom LL, Raman IM (2005) Open-channel block by the cytoplasmic tail of sodium channel beta4 as a mechanism for resurgent sodium current. *Neuron* **45**: 233-244
  67. Grissmer S, Nguyen AN, Aiyar J, Hanson DC, Mather RJ, Gutman GA, Karmilowicz MJ, Auperin DD, Chandy KG (1994) Pharmacological characterization of five cloned voltage-gated  $\text{K}^{+}$  channels, types  $\text{Kv}1.1$ ,  $1.2$ ,  $1.3$ ,  $1.5$ , and  $3.1$ , stably expressed in mammalian cell lines. *Mol Pharmacol* **45**: 1227-1234
  68. Grover LM, Teyler TJ (1990) Two components of long-term potentiation induced by different patterns of afferent activation. *Nature* **347**: 477-479
  69. Grubb MS, Burrone J (2010) Activity-dependent relocation of the axon initial segment fine-tunes neuronal excitability. *Nature* **465**: 1070-1074
  70. Hanse E, Gustafsson B (2001) Vesicle release probability and pre-primed pool at glutamatergic synapses in area CA1 of the rat neonatal hippocampus. *J Physiol* **531**: 481-493
  71. Harke B, Keller J, Ullal CK, Westphal V, Schonle A, Hell SW (2008) Resolution scaling in STED microscopy. *Opt Express* **16**: 4154-4162
  72. Harris KM, Stevens JK (1989) Dendritic spines of CA 1 pyramidal cells in the rat hippocampus: serial electron microscopy with reference to their biophysical characteristics. *J Neurosci* **9**: 2982-2997
  73. Harris KM, Sultan P (1995) Variation in the number, location and size of synaptic vesicles provides an anatomical basis for the nonuniform probability of release at hippocampal CA1 synapses. *Neuropharmacology* **34**: 1387-1395

- 
74. Harvey CD, Svoboda K (2007) Locally dynamic synaptic learning rules in pyramidal neuron dendrites. *Nature* **450**: 1195-1200
75. Hell SW, Wichmann J (1994) Breaking the diffraction resolution limit by stimulated emission: stimulated-emission-depletion fluorescence microscopy. *Opt Lett* **19**: 780-782
76. Hodgkin AL (1939) The relation between conduction velocity and the electrical resistance outside a nerve fibre. *J Physiol* **94**: 560-570
77. Hodgkin AL, Huxley AF (1952a) Propagation of electrical signals along giant nerve fibers. *Proc R Soc Lond B Biol Sci* **140**: 177-183
78. Hodgkin AL, Huxley AF (1952b) A quantitative description of membrane current and its application to conduction and excitation in nerve. *J Physiol* **117**: 500-544
79. Holderith N, Lorincz A, Katona G, Rozsa B, Kulik A, Watanabe M, Nusser Z (2012) Release probability of hippocampal glutamatergic terminals scales with the size of the active zone. *Nat Neurosci* **15**: 988-997
80. Holmes WR, Rall W (1992) Electrotonic length estimates in neurons with dendritic tapering or somatic shunt. *J Neurophysiol* **68**: 1421-1437
81. Hu H, Jonas P (2014) A supercritical density of Na channels ensures fast signaling in GABAergic interneuron axons. *Nat Neurosci*
82. Hu W, Tian C, Li T, Yang M, Hou H, Shu Y (2009) Distinct contributions of Na(v)1.6 and Na(v)1.2 in action potential initiation and backpropagation. *Nat Neurosci* **12**: 996-1002
83. Hursh JB (1939) Conduction velocity and diameter of nerve fibers. *American Journal of Physiology* **127**: 29-54
84. IMSpector. [www.max-planck-innovation.de/de/industrie/technologieangebote/software/](http://www.max-planck-innovation.de/de/industrie/technologieangebote/software/).
85. Ishizuka N, Weber J, Amaral DG (1990) Organization of intrahippocampal projections originating from CA3 pyramidal cells in the rat. *J Comp Neurol* **295**: 580-623
86. Izhikevich EM (2006) Polychronization: computation with spikes. *Neural Comput* **18**: 245-282
87. Jenkins SM, Bennett V (2001) Ankyrin-G coordinates assembly of the spectrin-based membrane skeleton, voltage-gated sodium channels, and L1 CAMs at Purkinje neuron initial segments. *J Cell Biol* **155**: 739-746
88. Jeromin A, Yuan LL, Frick A, Pfaffinger P, Johnston D (2003) A modified Sindbis vector for prolonged gene expression in neurons. *J Neurophysiol* **90**: 2741-2745
89. Kamiya H (2002) Kainate receptor-dependent presynaptic modulation and plasticity. *Neurosci Res* **42**: 1-6

- 
90. Katz B (1947) The effect of electrolyte deficiency on the rate of conduction in a single nerve fibre. *J Physiol* **106**: 411-417
  91. Klar TA, Hell SW (1999) Subdiffraction resolution in far-field fluorescence microscopy. *Opt Lett* **24**: 954-956
  92. Knott GW, Quairiaux C, Genoud C, Welker E (2002) Formation of dendritic spines with GABAergic synapses induced by whisker stimulation in adult mice. *Neuron* **34**: 265-273
  93. Kölliker A (1849) *Neurologische Bemerkungen.*, Vol. 1: 135–163.
  94. Kopec CD, Li B, Wei W, Boehm J, Malinow R (2006) Glutamate receptor exocytosis and spine enlargement during chemically induced long-term potentiation. *J Neurosci* **26**: 2000-2009
  95. Kuba H, Oichi Y, Ohmori H (2010) Presynaptic activity regulates Na(+) channel distribution at the axon initial segment. *Nature* **465**: 1075-1078
  96. Laezza F, Gerber BR, Lou JY, Kozel MA, Hartman H, Craig AM, Ornitz DM, Nerbonne JM (2007) The FGF14(F145S) mutation disrupts the interaction of FGF14 with voltage-gated Na<sup>+</sup> channels and impairs neuronal excitability. *J Neurosci* **27**: 12033-12044
  97. Lauri SE, Palmer M, Segerstrale M, Vesikansa A, Taira T, Collingridge GL (2007) Presynaptic mechanisms involved in the expression of STP and LTP at CA1 synapses in the hippocampus. *Neuropharmacology* **52**: 1-11
  98. Li CY, Lu JT, Wu CP, Duan SM, Poo MM (2004) Bidirectional modification of presynaptic neuronal excitability accompanying spike timing-dependent synaptic plasticity. *Neuron* **41**: 257-268
  99. Li KW, Jimenez CR (2008) Synapse proteomics: current status and quantitative applications. *Expert Rev Proteomics* **5**: 353-360
  100. Li XG, Somogyi P, Ylinen A, Buzsaki G (1994) The hippocampal CA3 network: an in vivo intracellular labeling study. *J Comp Neurol* **339**: 181-208
  101. Lisman J (1989) A mechanism for the Hebb and the anti-Hebb processes underlying learning and memory. *Proc Natl Acad Sci U S A* **86**: 9574-9578
  102. Lisman J, Raghavachari S (2006) A unified model of the presynaptic and postsynaptic changes during LTP at CA1 synapses. *Sci STKE* **2006**: re11
  103. Lisman JE, Harris KM (1993) Quantal analysis and synaptic anatomy--integrating two views of hippocampal plasticity. *Trends Neurosci* **16**: 141-147
  104. Llinas R, Sugimori M, Lin JW, Cherksey B (1989) Blocking and isolation of a calcium channel from neurons in mammals and cephalopods utilizing a toxin fraction (FTX) from funnel-web spider poison. *Proc Natl Acad Sci U S A* **86**: 1689-1693

- 
105. Lorincz A, Nusser Z (2008) Cell-type-dependent molecular composition of the axon initial segment. *J Neurosci* **28**: 14329-14340
  106. Loughney K, Kreber R, Ganetzky B (1989) Molecular analysis of the para locus, a sodium channel gene in *Drosophila*. *Cell* **58**: 1143-1154
  107. Luscher C, Streit J, Lipp P, Luscher HR (1994) Action potential propagation through embryonic dorsal root ganglion cells in culture. II. Decrease of conduction reliability during repetitive stimulation. *J Neurophysiol* **72**: 634-643
  108. Luscher HR, Shiner JS (1990) Simulation of action potential propagation in complex terminal arborizations. *Biophys J* **58**: 1389-1399
  109. Lynch GS, Dunwiddie T, Gribkoff V (1977) Heterosynaptic depression: a postsynaptic correlate of long-term potentiation. *Nature* **266**: 737-739
  110. Mainen ZF, Joerges J, Huguenard JR, Sejnowski TJ (1995) A model of spike initiation in neocortical pyramidal neurons. *Neuron* **15**: 1427-1439
  111. Major G, Larkman AU, Jonas P, Sakmann B, Jack JJ (1994) Detailed passive cable models of whole-cell recorded CA3 pyramidal neurons in rat hippocampal slices. *J Neurosci* **14**: 4613-4638
  112. Malenka RC, Bear MF (2004) LTP and LTD: an embarrassment of riches. *Neuron* **44**: 5-21
  113. Malenka RC, Nicoll RA (1999) Long-term potentiation--a decade of progress? *Science* **285**: 1870-1874
  114. Malinow R (1991) Transmission between pairs of hippocampal slice neurons: quantal levels, oscillations, and LTP. *Science* **252**: 722-724
  115. Malinow R, Malenka RC (2002) AMPA receptor trafficking and synaptic plasticity. *Annu Rev Neurosci* **25**: 103-126
  116. Manor Y, Koch C, Segev I (1991) Effect of geometrical irregularities on propagation delay in axonal trees. *Biophys J* **60**: 1424-1437
  117. Matsuzaki M, Honkura N, Ellis-Davies GC, Kasai H (2004) Structural basis of long-term potentiation in single dendritic spines. *Nature* **429**: 761-766
  118. McAllister AK (2007) Dynamic aspects of CNS synapse formation. *Annu Rev Neurosci* **30**: 425-450
  119. McIntyre CC, Richardson AG, Grill WM (2002) Modeling the excitability of mammalian nerve fibers: influence of afterpotentials on the recovery cycle. *J Neurophysiol* **87**: 995-1006

- 
120. McNaughton BL, Shen J, Rao G, Foster TC, Barnes CA (1994) Persistent increase of hippocampal presynaptic axon excitability after repetitive electrical stimulation: dependence on N-methyl-D-aspartate receptor activity, nitric-oxide synthase, and temperature. *Proc Natl Acad Sci U S A* **91**: 4830-4834
  121. Meeks JP, Jiang X, Mennerick S (2005) Action potential fidelity during normal and epileptiform activity in paired soma-axon recordings from rat hippocampus. *J Physiol* **566**: 425-441
  122. Meeks JP, Mennerick S (2007) Action potential initiation and propagation in CA3 pyramidal axons. *J Neurophysiol* **97**: 3460-3472
  123. Meshul CK, Hopkins WF (1990) Presynaptic ultrastructural correlates of long-term potentiation in the CA1 subfield of the hippocampus. *Brain Res* **514**: 310-319
  124. Meyer D, Bonhoeffer T, Scheuss V (2014) Balance and Stability of Synaptic Structures during Synaptic Plasticity. *Neuron* **82**: 430-443
  125. Mintz IM, Venema VJ, Swiderek KM, Lee TD, Bean BP, Adams ME (1992) P-type calcium channels blocked by the spider toxin omega-Aga-IVA. *Nature* **355**: 827-829
  126. Moalem-Taylor G, Lang PM, Tracey DJ, Grafe P (2007) Post-spike excitability indicates changes in membrane potential of isolated C-fibers. *Muscle Nerve* **36**: 172-182
  127. Moore JW, Stockbridge N, Westerfield M (1983) On the site of impulse initiation in a neurone. *J Physiol* **336**: 301-311
  128. Nagerl UV, Willig KI, Hein B, Hell SW, Bonhoeffer T (2008) Live-cell imaging of dendritic spines by STED microscopy. *Proc Natl Acad Sci U S A* **105**: 18982-18987
  129. Palay SL, Sotelo C, Peters A, Orkand PM (1968) The axon hillock and the initial segment. *J Cell Biol* **38**: 193-201
  130. Pan Z, Selyanko AA, Hadley JK, Brown DA, Dixon JE, McKinnon D (2001) Alternative splicing of KCNQ2 potassium channel transcripts contributes to the functional diversity of M-currents. *J Physiol* **531**: 347-358
  131. Parnas I (1972) Differential block at high frequency of branches of a single axon innervating two muscles. *J Neurophysiol* **35**: 903-914
  132. Pelkey KA, Topolnik L, Lacaille JC, McBain CJ (2006) Compartmentalized Ca(2+) channel regulation at divergent mossy-fiber release sites underlies target cell-dependent plasticity. *Neuron* **52**: 497-510
  133. Perroy J, Prezeau L, De Waard M, Shigemoto R, Bockaert J, Fagni L (2000) Selective blockade of P/Q-type calcium channels by the metabotropic glutamate receptor type 7 involves a phospholipase C pathway in neurons. *J Neurosci* **20**: 7896-7904

- 
134. Pina-Crespo JC, Gibb AJ (2002) Subtypes of NMDA receptors in new-born rat hippocampal granule cells. *J Physiol* **541**: 41-64
135. Pocock JM, Venema VJ, Adams ME (1992) Omega-agatoxins differentially block calcium channels in locust, chick and rat synaptosomes. *Neurochem Int* **20**: 263-270
136. Rall W (1962) Theory of physiological properties of dendrites. *Ann N Y Acad Sci* **96**: 1071-1092
137. Ramon y Cajal S (1897) Leyes de la morfología y dinamismo de las células nerviosas. *Rev Trim Micrograf* **2**: 1-12
138. Rankin BR, Moneron G, Wurm CA, Nelson JC, Walter A, Schwarzer D, Schroeder J, Colon-Ramos DA, Hell SW (2011) Nanoscopy in a living multicellular organism expressing GFP. *Biophys J* **100**: L63-65
139. Rapp M, Yarom Y, Segev I (1996) Modeling back propagating action potential in weakly excitable dendrites of neocortical pyramidal cells. *Proc Natl Acad Sci U S A* **93**: 11985-11990
140. Remak R (1855) *über den Bau der grauen Säuden im Rückenmark der Säugethiere.*, Vol. 7: 295: Deutsche Klinik.
141. Renganathan M, Cummins TR, Waxman SG (2001) Contribution of Na(v)1.8 sodium channels to action potential electrogenesis in DRG neurons. *J Neurophysiol* **86**: 629-640
142. Reynolds IJ, Wagner JA, Snyder SH, Thayer SA, Olivera BM, Miller RJ (1986) Brain voltage-sensitive calcium channel subtypes differentiated by omega-conotoxin fraction GVIA. *Proc Natl Acad Sci U S A* **83**: 8804-8807
143. Rittweger E, Young Han K, Irvine SE, Eggeling C, Hell SW (2009) STED microscopy reveals crystal colour centres with nanometric resolution. *Nature Photonics*
144. Ropireddy D, Scorcioni R, Lasher B, Buzsaki G, Ascoli GA (2011) Axonal morphometry of hippocampal pyramidal neurons semi-automatically reconstructed after in vivo labeling in different CA3 locations. *Brain Struct Funct* **216**: 1-15
145. Rosenthal JJ, Bezanilla F (2000) Seasonal variation in conduction velocity of action potentials in squid giant axons. *Biol Bull* **199**: 135-143
146. Rossi B, Maton G, Collin T (2008) Calcium-permeable presynaptic AMPA receptors in cerebellar molecular layer interneurons. *J Physiol* **586**: 5129-5145
147. Rusakov DA (2006) Ca<sup>2+</sup>-dependent mechanisms of presynaptic control at central synapses. *Neuroscientist* **12**: 317-326
148. Rushton WA (1951) A theory of the effects of fibre size in medullated nerve. *J Physiol* **115**: 101-122

- 
149. Salami M, Itami C, Tsumoto T, Kimura F (2003) Change of conduction velocity by regional myelination yields constant latency irrespective of distance between thalamus and cortex. *Proc Natl Acad Sci U S A* **100**: 6174-6179
  150. Sasaki T, Matsuki N, Ikegaya Y (2011) Action-potential modulation during axonal conduction. *Science* **331**: 599-601
  151. Sasaki T, Matsuki N, Ikegaya Y (2012a) Effects of axonal topology on the somatic modulation of synaptic outputs. *J Neurosci* **32**: 2868-2876
  152. Sasaki T, Matsuki N, Ikegaya Y (2012b) Targeted axon-attached recording with fluorescent patch-clamp pipettes in brain slices. *Nat Protoc* **7**: 1228-1234
  153. Schikorski T, Stevens CF (2001) Morphological correlates of functionally defined synaptic vesicle populations. *Nat Neurosci* **4**: 391-395
  154. Shah M, Mistry M, Marsh SJ, Brown DA, Delmas P (2002) Molecular correlates of the M-current in cultured rat hippocampal neurons. *J Physiol* **544**: 29-37
  155. Shah MM, Migliore M, Valencia I, Cooper EC, Brown DA (2008) Functional significance of axonal Kv7 channels in hippocampal pyramidal neurons. *Proc Natl Acad Sci U S A* **105**: 7869-7874
  156. Shapiro E, Castellucci VF, Kandel ER (1980) Presynaptic membrane potential affects transmitter release in an identified neuron in *Aplysia* by modulating the Ca<sup>2+</sup> and K<sup>+</sup> currents. *Proc Natl Acad Sci U S A* **77**: 629-633
  157. Shepherd GM, Harris KM (1998) Three-dimensional structure and composition of CA3→CA1 axons in rat hippocampal slices: implications for presynaptic connectivity and compartmentalization. *J Neurosci* **18**: 8300-8310
  158. Siegel SJ, Brose N, Janssen WG, Gasic GP, Jahn R, Heinemann SF, Morrison JH (1994) Regional, cellular, and ultrastructural distribution of N-methyl-D-aspartate receptor subunit 1 in monkey hippocampus. *Proc Natl Acad Sci U S A* **91**: 564-568
  159. Smith DO (1980a) Mechanisms of action potential propagation failure at sites of axon branching in the crayfish. *J Physiol* **301**: 243-259
  160. Smith DO (1980b) Morphological aspects of the safety factor for action potential propagation at axon branch points in the crayfish. *J Physiol* **301**: 261-269
  161. Soleng AF, Baginskas A, Andersen P, Raastad M (2004) Activity-dependent excitability changes in hippocampal CA3 cell Schaffer axons. *J Physiol* **560**: 491-503
  162. Soleng AF, Chiu K, Raastad M (2003a) Unmyelinated axons in the rat hippocampus hyperpolarize and activate an H current when spike frequency exceeds 1 Hz. *J Physiol* **552**: 459-470

- 
163. Soleng AF, Raastad M, Andersen P (2003b) Conduction latency along CA3 hippocampal axons from rat. *Hippocampus* **13**: 953-961
  164. Song I, Huganir RL (2002) Regulation of AMPA receptors during synaptic plasticity. *Trends Neurosci* **25**: 578-588
  165. Stanford LR (1987) Conduction velocity variations minimize conduction time differences among retinal ganglion cell axons. *Science* **238**: 358-360
  166. Stepanyants A, Hof PR, Chklovskii DB (2002) Geometry and structural plasticity of synaptic connectivity. *Neuron* **34**: 275-288
  167. Stevens CF, Wang Y (1994) Changes in reliability of synaptic function as a mechanism for plasticity. *Nature* **371**: 704-707
  168. Stricker C, Cowan AI, Field AC, Redman SJ (1999) Analysis of NMDA-independent long-term potentiation induced at CA3-CA1 synapses in rat hippocampus in vitro. *J Physiol* **520 Pt 2**: 513-525
  169. Stys PK, Sontheimer H, Ransom BR, Waxman SG (1993) Noninactivating, tetrodotoxin-sensitive Na<sup>+</sup> conductance in rat optic nerve axons. *Proc Natl Acad Sci U S A* **90**: 6976-6980
  170. Sugihara I, Lang EJ, Llinas R (1993) Uniform olivocerebellar conduction time underlies Purkinje cell complex spike synchronicity in the rat cerebellum. *J Physiol* **470**: 243-271
  171. Swadlow HA (1982) Impulse conduction in the mammalian brain: physiological properties of individual axons monitored for several months. *Science* **218**: 911-913
  172. Swadlow HA (1985) Physiological properties of individual cerebral axons studied in vivo for as long as one year. *J Neurophysiol* **54**: 1346-1362
  173. Tippens AL, Pare JF, Langwieser N, Moosmang S, Milner TA, Smith Y, Lee A (2008) Ultrastructural evidence for pre- and postsynaptic localization of Cav1.2 L-type Ca<sup>2+</sup> channels in the rat hippocampus. *J Comp Neurol* **506**: 569-583
  174. Tokuno HA, Kocsis JD, Waxman SG (2003) Noninactivating, tetrodotoxin-sensitive Na<sup>+</sup> conductance in peripheral axons. *Muscle Nerve* **28**: 212-217
  175. Toni N, Buchs PA, Nikonenko I, Bron CR, Muller D (1999) LTP promotes formation of multiple spine synapses between a single axon terminal and a dendrite. *Nature* **402**: 421-425
  176. Turner TJ, Adams ME, Dunlap K (1992) Calcium channels coupled to glutamate release identified by omega-Aga-IVA. *Science* **258**: 310-313

- 
177. Uchitel OD, Protti DA, Sanchez V, Cherksey BD, Sugimori M, Llinas R (1992) P-type voltage-dependent calcium channel mediates presynaptic calcium influx and transmitter release in mammalian synapses. *Proc Natl Acad Sci U S A* **89**: 3330-3333
178. Veh RW, Lichtinghagen R, Sewing S, Wunder F, Grumbach IM, Pongs O (1995) Immunohistochemical localization of five members of the Kv1 channel subunits: contrasting subcellular locations and neuron-specific co-localizations in rat brain. *Eur J Neurosci* **7**: 2189-2205
179. Voronin LL, Altinbaev RS, Bayazitov IT, Gasparini S, Kasyanov AV, Saviane C, Savtchenko L, Cherubini E (2004) Postsynaptic depolarisation enhances transmitter release and causes the appearance of responses at "silent" synapses in rat hippocampus. *Neuroscience* **126**: 45-59
180. Watanabe S, Rost BR, Camacho-Perez M, Davis MW, Sohl-Kielczynski B, Rosenmund C, Jorgensen EM (2013) Ultrafast endocytosis at mouse hippocampal synapses. *Nature* **504**: 242-247
181. Waxman SG, Ritchie JM (1993) Molecular dissection of the myelinated axon. *Ann Neurol* **33**: 121-136
182. Westrum LE, Blackstad TW (1962) An electron microscopic study of the stratum radiatum of the rat hippocampus (regio superior, CA 1) with particular emphasis on synaptology. *J Comp Neurol* **119**: 281-309
183. Willig KI, Nagerl UV (2012) Stimulated emission depletion (STED) imaging of dendritic spines in living hippocampal slices. *Cold Spring Harb Protoc* **2012**
184. Wittner L, Henze DA, Zaborszky L, Buzsaki G (2007) Three-dimensional reconstruction of the axon arbor of a CA3 pyramidal cell recorded and filled in vivo. *Brain Struct Funct* **212**: 75-83
185. Xu J, Kang N, Jiang L, Nedergaard M, Kang J (2005) Activity-dependent long-term potentiation of intrinsic excitability in hippocampal CA1 pyramidal neurons. *J Neurosci* **25**: 1750-1760
186. Xu K, Zhong G, Zhuang X (2013) Actin, spectrin, and associated proteins form a periodic cytoskeletal structure in axons. *Science* **339**: 452-456
187. Yang Y, Ogawa Y, Hedstrom KL, Rasband MN (2007) betaIV spectrin is recruited to axon initial segments and nodes of Ranvier by ankyrinG. *J Cell Biol* **176**: 509-519
188. Yang Y, Wang XB, Frerking M, Zhou Q (2008) Spine expansion and stabilization associated with long-term potentiation. *J Neurosci* **28**: 5740-5751
189. Young JS, Peck LS, Matheson T (2006) The effects of temperature on peripheral neuronal function in eurythermal and stenothermal crustaceans. *J Exp Biol* **209**: 1976-1987

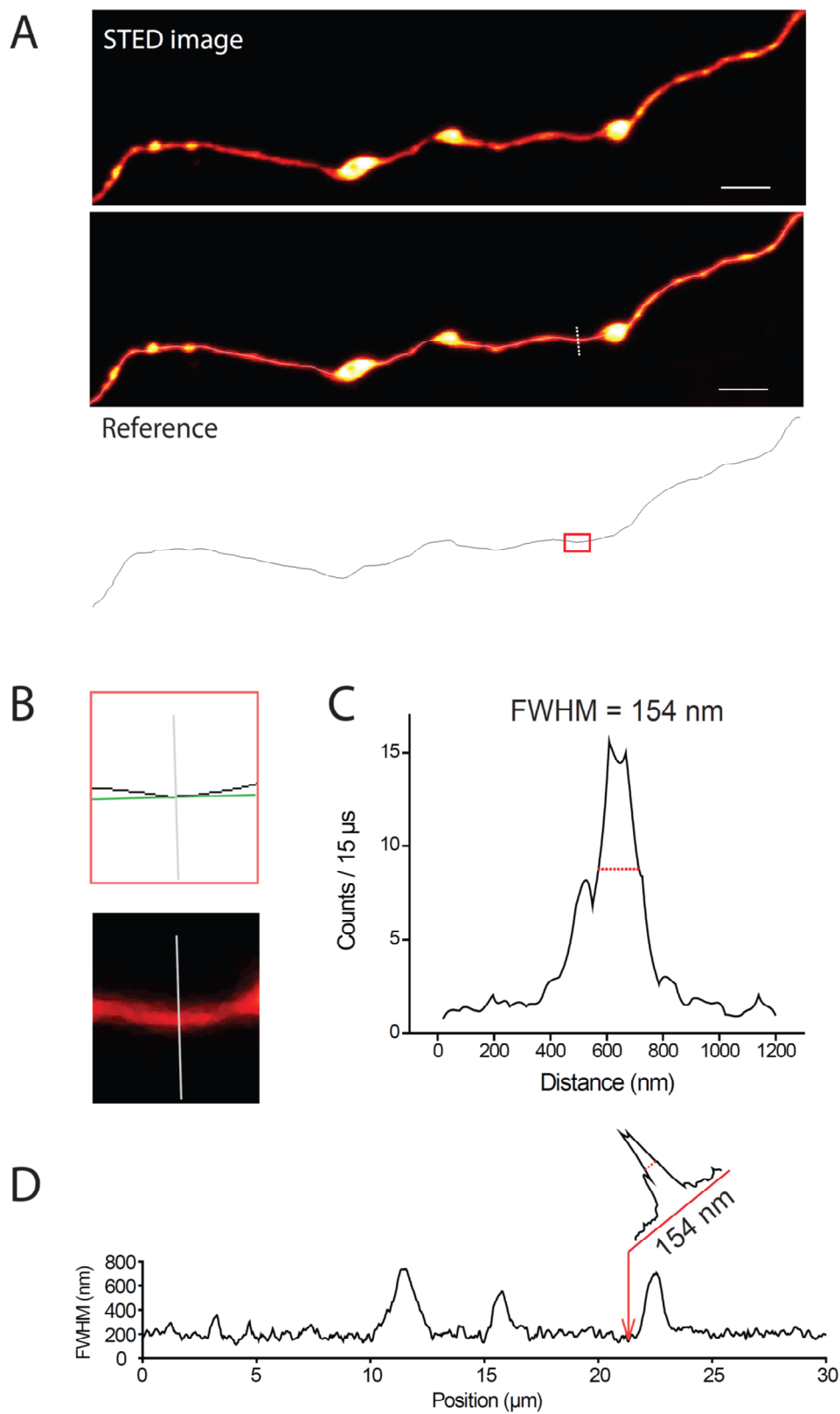
- 
190. Yue C, Yaari Y (2006) Axo-somatic and apical dendritic Kv7/M channels differentially regulate the intrinsic excitability of adult rat CA1 pyramidal cells. *J Neurophysiol* **95**: 3480-3495
  191. Zakharenko SS, Zablow L, Siegelbaum SA (2001) Visualization of changes in presynaptic function during long-term synaptic plasticity. *Nat Neurosci* **4**: 711-717
  192. Zhang W, Linden DJ (2003) The other side of the engram: experience-driven changes in neuronal intrinsic excitability. *Nat Rev Neurosci* **4**: 885-900
  193. Zhou D, Lambert S, Malen PL, Carpenter S, Boland LM, Bennett V (1998) AnkyrinG is required for clustering of voltage-gated Na channels at axon initial segments and for normal action potential firing. *J Cell Biol* **143**: 1295-1304
  194. Zhou Q, Homma KJ, Poo MM (2004) Shrinkage of dendritic spines associated with long-term depression of hippocampal synapses. *Neuron* **44**: 749-757

## APPENDIX

The following pages correspond to the algorithm written in Matlab used for the automated analysis of the axon diameters.

It consists in a main program called 'axomorph' and a series of functions used in this program.

The figure next page illustrates how the automatic measurement is performed by the program. From the image of an axon stretch, a reference line of pixels corresponding to the center of the axon stretch (or skeleton) is generated using ImageJ or the home-made function 'refcreator' (A). In order to realize the measure of the cross section diameter, it is necessary to find the best orthogonal line at every position. Therefore, for every position (pixel of the reference line) a linear fit is performed based on a group of pixels around the position. Then, the orthogonal line passing thru the pixel position is calculated (B). The pixel coordinates of the orthogonal line are used to collect the intensity values of the axon cross section for the position and built the Gaussian-like intensity profile (C). From this, the FWHM value is extracted by detecting the edges of the curve at 50 % the maximum. The maximum is defined as the average of the three brightest pixels. Then the measurement is reported for the position and repeated for the next pixel of the reference line (D).



```

function result = axomorph
(axoimage,ref,pixsizenm,linewidth,nf,flip,visual)

%% Function that plots the FWHM of an axon at any given section. The x-axis
% is in  $\mu\text{m}$  and the y-axis is in nm.
%%%%%% Ronan Chéreau %%%%%% REVISION: November 29, 2012
%%%%%%%%%%%%%%%%%%%%%%%%%%%%%%%%%%%%%%%%%%%%%%%%%%%%%%%%%%%%%%%%%%%%%%%%
%INPUTS: axoimage = the real image containing the axon to be measured
%         ref = reference line going thru the center of the axon (usually a
skeletonization of the axon in imagej)
%         pixsizenm = enter the value of the pixel size resolution of the
picture (assuming that the pixel is not rectangular)
%         (auto defined) lfitvector = number of pixels used to make the
linear fit at every section
%         (auto defined) limplot = number of pixels value from the axoimage
to plot at every step
%         linewidth = width of the line in pixels
%         nf = noise filter: allow the user to choose the number of data
points to average in order to smoothen the plot
%         flip = if you want to inverse the data, flip=1
%         visual = if you want to visualize the measurement process,visual=1
%
%OUTPUTS:
%         In the figure: show the original axon image; the reference line;
%         the plot of all the raw data collected; the linear transformation
%         of the axon and the plot of the calculated FWHM over the distance.

%% Set default value in the inputs if nothing entered
if nargin==2, pixsizenm=19.5; linewidth=3; nf=2; flip=0; visual=0; end
if nargin==3, linewidth=3; nf=2; flip=0; visual=0; end
if nargin==4, nf=2; flip=0; visual=0; end
if nargin==5, flip=0; visual=0; end
if nargin==6, visual=0; end

%% Determination of few variables
taille=size(axoimage);%for later, I will need those limits to avoid the
program to look for pixels outside of the real image
%this module is here the correct the reading of the ref. If the values of
%the background is 255 and the line is 0 then it will make the negative so
%it does not bug.
binref=ref>0; %binarize the image
%binref=check_ref(binref); %invert the values of the image in case the
background is 1 and the line is 0. automatic check

%% Finds the coordinates of the pixels in the reference image
xyline=findline2(binref);%see findline2 function

%% Orientation of image for result by determining the distance of the 2
ends of xyline from the left side of the axoimage.
dist2ref_1=(xyline(1,1)-fix (size (ref, 1)/2))/(xyline (1, 2)-1);
dist2ref_2=(xyline(size (xyline,1),1)-fix (size (ref, 1)/2))/(xyline ( size
(xyline, 1) , 2)-1);

%to delete in the future
%dist2ref_1=sqrt((xyline(1,1)-fix (size (ref, 1)/2))^2 + (xyline (1, 2)-
1)^2);
%dist2ref_2=sqrt((xyline(size (xyline,1),1)-fix (size (ref, 1)/2))^2 +
(xyline ( size (xyline, 1) , 2)-1)^2);

```

---

```

if dist2ref_2> dist2ref_1,
    %flip findline points
    xyline=flipud(xyline);
end
xline=xyline(:,1); yline=xyline(:,2); %just to separate the coordinates in
2 vectors so the writing is easier for what is coming

% if a filtering has been applied to the axon picture, sometimes pixels
has
%negative values, this puts them to 0.
for ix=1:taille(1),
    for iy=1:taille(2),
        if axoimage(ix,iy)<0,
            axoimage(ix,iy)=0;
        end
    end
end

% then I have to be able to use the first 'lfitvector' pixels coordinates
do all bunch
%of things and select the next 'lfitvector' pixels at the next pixel and
repeat etc...
npoint=size(xyline,1); %returns the number of points in my line
index=0;

if pixsizenm<=20, lfitvector=30; limplot=30;
    elseif pixsizenm<=30, lfitvector=30; limplot=24;
        elseif pixsizenm<=40, lfitvector=22; limplot=30;
            elseif pixsizenm<=50, lfitvector=10; limplot=8;
                else lfitvector=8; limplot=10; disp('Warning: the pixel size of the
image is too big for measuring axons, result might not be accurate...Give
me more resolution!!!')
            end
end
flip_pic=0;

% Determines the best tangential for a given segment of the axon

%Preallocation of variables
for ic=1:npoint;
    if ic+lfitvector<=npoint,
        index=index+1;
    end
end
axonprofile=zeros(index,2*limplot+1);
index=0;
for ic=1:npoint-lfitvector;
    if ic+lfitvector<=npoint,
        index=index+1;
    end
end
pixdistfactor=NaN(1,index);
FWHMraw=NaN(1,index);
FWHMfilter=NaN(1,index-nf);
cumul=NaN(1,index);
line_limit(1,(1:index))=250;
index=0;
%
```



---

```

        if and(avgY>0,avgY<taille(2)),
            if and(avgX>0,avgX<taille(1)),
                profilevalue(lwindex)=axoimage(avgX,avgY);
                if visual==1,
                    if flip_pic==0,
                        axoimage_rep(avgX,avgY)=255;
                        ref_rep(avgX,avgY)=255;
                    end
                end
                numval2avg=numval2avg+1;
            else profilevalue(lwindex)=NaN;
            end
        else profilevalue(lwindex)=NaN;
        end
        if numval2avg==0,
            axonprofile(index,plotindex)=NaN;
        else axonprofile(index,plotindex)=
nansum(profilevalue)/numval2avg;
        end
    end
end

Xmorpho=pixdistfactor*pixsizenm/1000;%returns the real distances in nm
between the pixels sections

%% Calculation of the FWHM with all the profiles collected
if visual==0,

FWHMraw(index)=fwhmraw(double(axonprofile(index,:)))*pixsizenm*pixdistfacto
r(index);
elseif visual==1,
    FWHMraw_withline=fwhmraw(double(axonprofile(index,:)),1);
    FWHMraw(index)=FWHMraw_withline(1)*pixsizenm*pixdistfactor(index);
    min_linelimit=FWHMraw_withline(2)*pixsizenm*pixdistfactor(index);
    max_linelimit=FWHMraw_withline(3)*pixsizenm*pixdistfactor(index);
    halfmax_linelimit=FWHMraw_withline(4);
end

    for in=1:index, cumul(in)=sum(Xmorpho(1:in)); end

%% Layout of the result in visualization mode
if visual==1,
    min_intensity=min(axoimage(:));
    max_intensity=max(axoimage(:));
    %normalization for the intensity profile plot
    axonprofile_norm=axonprofile;
    for i_plot=1:limplot*2+1,

axonprofile_norm(index,i_plot)=axonprofile(index,i_plot)/max(axonprofile(in
dex,:));
    end
    %halfmax_linelimit=halfmax_linelimit/max(axonprofile(index,:));
    %x values for the plot
    xval_axonprofileindex=NaN(limplot*2+1,1);
    for i_xval=1:2*limplot+1,

```

---

```

xval_axonprofileindex(i_xval)=i_xval*pixsizenm*pixdistfactor(index);
end

figure (1);
set(gcf, 'color', 'white');
subplot(5,5,[1:4 6:9]);
if taille(2)>taille(1),
    imshow(axoimage_rep,[min_intensity max_intensity]);figure(gcf);
else imshow(axoimage_rep',[min_intensity max_intensity]);figure(gcf);
end
title('STED image','fontsize',15);

subplot(5,5,[11:13 16:18]);
if taille(2)>taille(1),
imshow(ref_rep);figure(gcf);
else imshow(ref_rep');figure(gcf);
end
title('Reference image','fontsize',15);
%imshow(axonprofile'/linewidth,[min_intensity
max_intensity]);figure(gcf);
%title('Axon linearization','fontsize',15);
colormap(hot)

subplot(5,5,[10 15 20]);
plot(xval_axonprofileindex,axonprofile_norm(index,:),'-
blacko',[min_linelimit max_linelimit],[halfmax_linelimit
halfmax_linelimit'],'r');figure(gcf)
set(gca, 'box', 'off')
xlabel('(nm)','fontsize',12)
ylabel('Normalized intensity','fontsize',12)
axis([0 1500 0 1])
title(['FWHM = ', num2str(FWHMraw(index), '%4.0f'), '
nm'],'fontsize',15);

subplot (5,5,21:25);
plot(cumul,FWHMraw,'black',cumul,line_limit,'r:');figure(gcf)
set(gca, 'box', 'off')
xlabel('Position (µm)','fontsize',12)
ylabel('FWHM (nm)','fontsize',12)
axis([0 16 0 610]);
title('Diameter profile','fontsize',15)

%if FWHMraw(index)<= 200,
%    title ('Diameter profile','color','red','fontsize',15);
%    hold off
%else
%    title ('','color','white','fontsize',15);
%    hold off
%end
hold on
%saveas(gcf, ['visual' num2str(index)], 'tif');
end
end

% feature that allow the user to choose how many data point to average in
order to smoothen the plot.
for i=1:index-nf,

```

---

```

        FWHMfilter(i)=(median(FWHMraw(i:i+nf-1)));
        cumulfilter=cumul(1:i);

    end

    if flip==1;
    cumulfilter=abs(max(cumulfilter)-cumulfilter);
    end

    result=[cumulfilter;FWHMfilter];
    result=result';

%% Layout of the result in normal mode
if visual==0,
    figure (1);
    set(gcf, 'color', 'white');
    subplot(4,4,[1:3 5:7]);
    if taille(2)>taille(1),
    imshow(axoimage,[min(axoimage(:)) max(axoimage(:))]);figure(gcf);
    else imshow(axoimage',[min(axoimage(:)) max(axoimage(:))]);figure(gcf);
    end
    title('STED image','fontsize',15);

    subplot(4,4,9:12);
    imshow(axonprofile'/linewidth,[min(axoimage(:))
max(axoimage(:))]);figure(gcf);
    title('Axon linearization','fontsize',15);
    colormap(hot);

    subplot(4,4,[4 8]);
    plot(axonprofile(index,:));figure(gcf)
    xlabel('Position (µm)','fontsize',15)
    ylabel('Fluo. intensity','fontsize',15)
    title(['FWHM = ', num2str(FWHMraw(index), '%3.1f'),
'nm'],'color','red','fontsize',15);

    subplot (4,4,13:16);
    plot(cumulfilter,FWHMfilter);figure(gcf)
    xlabel('Position (µm)','fontsize',15)
    ylabel('FWHM (nm)','fontsize',15)
    hold on
end

```

---

```
function continuousline=findline2(binref)
```

```
%%%%%%%%%%%%%REVISION: Aug 20, 2012%%%%%%%%%
```

```
%rev Aug 20, 2012: the line is simplified, it looks for the diag pix before
%horizontal or vert.
```

```
%The idea of this is to avoid mistakes for complex forms of axons where in
%an extreme case, it would make loop, therefore in this case the find
%function is not strong enough
%detect the succession of pixels in a line
%The first part is to identify one end of the line by screening the binary
```

```

%matrix
%The second part collect the pixels in a new matrix going from one end to
%the other

%Made for axomorph

%The contour of the image has to be zero in order the the program to not
%look at the neighbor outside of the picture. And also to make sure that
%there was no weired processing that gives a contour line on the image.
binref=binref>0;
size_mat=size(binref);
binref(1,:)=0;
binref(:,1)=0;
binref(size_mat(1),:)=0;
binref(:,size_mat(2))=0;

%since I'm going to erase the values to find one end of the line, I have to
%duplicate the matrix.
binref1=binref;

%%1st part: take the coordinates of any pixel of the line%%
[xlin,ylin]=ind2sub(size(binref),find(binref)); %find(binref) returns only
the pixels containing a 1
%ind2sub use the size of the matrix to transform the values in x,y
%coordinates because by default it gives
% 1 position value per pixel (i.e. 2050 > (50,20))
x=xlin(1); y=ylin(1); %this returns the coordinates of the first pixel in
the %find list pixel which is not necessarily the first of the line

%%2nd part: finding the pixel coordinates of one of the 2 end of the
%%line. It's screening the positive pixels in the neighbourhood, and
%%since we want to go over all the pixels, it's looking first in
%%horizontal, then vertical, then both diagonals. Horizontal and
%%vertical have the priority because in some cases one pixel can have 2
%%postives neighbours.
for i=1:size(xlin),
%   if x<size(binref1(1))-1 & y<size(binref1(2))-1,
%       if binref1(x+1,y)==1,
%           binref1(x,y)=0; %I turn the current positif pixel off, since I
found %the next.
%           %This way the cursor is polarized and will not go backward      000
%           x=x+1; %it moves the cursor once the condition is verified      011
%           %                                                                    000
%       else
%           if binref1(x-1,y)==1,
%               binref1(x,y)=0;
%               x=x-1;
%           else
%               if binref1(x,y+1)==1,
%                   binref1(x,y)=0;
%                   y=y+1;
%               else
%                   if binref1(x,y-1)==1,
%                       binref1(x,y)=0;
%                       y=y-1;
%                   else

```



---

```

        linex(idx-1)=x-1;
        liney(idx-1)=y-1;
        binref(x,y)=0;binref(x+1,y)=0;binref(x-
1,y)=0;binref(x,y+1)=0;binref(x,y-1)=0;
        x=x-1; y=y-1;
    else
        if binref(x+1,y)==1;           % 000
            linex(idx-1)=x+1;         % 011
            liney(idx-1)=y;           % 000
            binref(x,y)=0;
            x=x+1;
        else
            if binref(x-1,y)==1;
                linex(idx-1)=x-1;
                liney(idx-1)=y;
                binref(x,y)=0;
                x=x-1;
            else
                if binref(x,y+1)==1;
                    linex(idx-1)=x;
                    liney(idx-1)=y+1;
                    binref(x,y)=0;
                    y=y+1;
                else
                    if binref(x,y-1)==1;
                        linex(idx-1)=x;
                        liney(idx-1)=y-1;
                        binref(x,y)=0;
                        y=y-1;
                    else
                        end
                    end
                end
            end
        end
    end
end

continuousline=[linex',liney'];

end

```

---

```

function coeff = pixlinefit_5(X,Y)

%%%%%REVISION: Nov 29, 2012 %%%%%%%%%%%%%%%%%%%%%%%%%%%%%%%
%Function that returns the coefficient of a linear regression from pixel
%coordinates
%Made for axomorph

nbpix=size(X,1);
X=X'; Y=Y';
%I will calculate coefficients the lines using pairs of points from the
%center to the edges of the serie of coordinates, applying a coefficient of
%importance following a gaussian distribution. The contribution of the
%values found in the middle is more important than on the edges, I hope it

```

---

```

%will give me a very accurate result.

for i=1:fix(nbpix/2),
    flip_meas=0;
    if X(i)-X(nbpix-i+1)==0,
        coeff_pairs(i)=Inf;
        %what if I could have some +Inf and -Inf
    else
        coeff_pairs(i)=(Y(i)-Y(nbpix-i+1))/((X(i)-X(nbpix-i+1)));
    end
end

if abs(mean(coeff_pairs))>100,%before was >1, to see for later
    flip_meas=1;
    for i=1:fix(nbpix/2),
        if Y(i)-Y(nbpix-i+1)==0,
            coeff_pairs(i)=Inf;
        else coeff_pairs(i)=(X(i)-X(nbpix-i+1))/((Y(i)-Y(nbpix-i+1)));
        end
    end
end
%coefficient from a normal function in the interval [-2;0]
s_coeff=size(coeff_pairs,2);
count=0;

for i=-2:4/(2*(s_coeff-1)):0,
    count=count+1;
    y(count)=(1/(sqrt(2*pi))*exp((-i^2)/2));
end
%normalization of the gaussian value to 1

for i=1:size(y,2),
    norm_y(i)=y(i)/sum(y);
end
y=norm_y;

tan_coeff=atan(coeff_pairs);
calc_coeff=zeros(1,s_coeff);
for i=1:s_coeff,
    calc_coeff(i)=tan_coeff(i)*y(i);
end
sum_tancoeff=sum(calc_coeff);
if flip_meas==1,
    coeff=1/(tan(sum_tancoeff));
else coeff=tan(sum_tancoeff);
end

%for test%
%image=zeros(100,100);
%for i=1:size(X,1),
%    image(X(i),Y(i))=1;
%end

```

---

```
function fwhmraw = fwhmraw(plot)
```

---

```

%%%%%%%%%REVISION: April 15,
2011%%%%%%%%%
%function that determines the full width half-maximum from a vector that is
%gaussian-like distributed.
%plot is the serie of data
%Made for axomorph

sizeplot=size(plot);
sizeplot=sizeplot(2);
avgmin=(nansum(plot(1:5))+nansum(plot(sizeplot-4:sizeplot)))/10; %calculates
the minimum of the plot looking at the first 5 values and the 5 last values
and make an average of it
maxval=max(plot); %finds the maximum value of the plot
rankmaxplot=fix(sizeplot/2);
for i=1:sizeplot, %this loop is just to find the rank of the maxvalue of
the plot
    if plot(i)==maxval,
        rankmaxplot=i;
    else
    end
end

halfmax=((maxval-avgmin)/2)+avgmin; %obvious enough

index=1;
minrankhm=0;
maxrankhm=0;

for ia=-(rankmaxplot-1):-1, %finds the ranks of the 2 edges of the
FWHM
    if plot(abs(ia))<halfmax, %starts from the maxvalue and look for the
ranks that are lower than halfmax, i keep the first found value
        minrankhm(index)=abs(ia);
        index=index+1;
    else
    end
end

minrankhm=minrankhm(1);
index=1;

for ib=rankmaxplot+1:sizeplot,
    if plot(ib)<halfmax,
        maxrankhm(index)=abs(ib);
        index=index+1;
    else
    end
end

maxrankhm=maxrankhm(1);
if minrankhm==0, %from the rank, it determines exactly where it cuts the
plot at half max (determination of xmin and xmax)
    xmin=NaN;
else if plot(minrankhm+1) ~= halfmax,
    coeffmin=plot(minrankhm+1)-plot(minrankhm);
    xmin=((halfmax-plot(minrankhm))/coeffmin)+minrankhm;
else xmin=minrankhm+1;
end

```

```

end

if maxrankhm==0,
    xmax=NaN;
else if plot(maxrankhm-1) ~= halfmax,
    coeffmax=plot(maxrankhm-1)-plot(maxrankhm);
    xmax=maxrankhm-((halfmax-plot(maxrankhm))/coeffmax);
else xmax=maxrankhm-1;
end
end

if or(isnan(xmin), isnan(xmax)),
    fwhmraw=NaN;
else fwhmraw=xmax-xmin;
end

```

---

```

function result=check_ref(binref)

```

```

%Revision Setp 13, 2011
%USED BY AXOMORPH
%check the reference image that the values of the line is positive and
%above 0 and that the background is 0, otherwise it does a negative of the
%image

```

```

%returns binref with 0 values for background and 1 values for the line

```

```

size_binref=size(binref);
size_x=size_binref(1);
size_y=size_binref(2);
%find the coordinates of the pixel in the center of the image
test_pix_x=fix(size_x);
test_pix_y=fix(size_y);
%I look for the ratio of positive pixels in a cross that is representing
%10% of the picture and in a square. If more than 50% are positive, I
%inverse the picture
index_cross_x=0;
count_x=0;
for cursor_x=-ceil(0.1*size_x):1:+fix(0.1*size_x),
    if binref(test_pix_x+cursor_x,test_pix_y)==1,
        index_cross_x=index_cross_x+1;
    end
    count_x=count_x+1;
end

index_cross_y=0;
count_y=0;
for cursor_y=-ceil(0.1*size_y):1:+fix(0.1*size_y),
    if binref(test_pix_x,test_pix_y+cursor_y)==1,
        index_cross_y=index_cross_y+1;
    end
    count_y=count_y+1;
end

index_cross_x1=0;
count_x1=0;

```

---

```

for cursor_x=-ceil(0.1*size_x):1:+fix(0.1*size_x),
    if binref(test_pix_x+cursor_x,test_pix_y-ceil(0.1*size_y))==1,
        index_cross_x1=index_cross_x1+1;
    end
    count_x1=count_x1+1;
end

index_cross_y1=0;
count_y1=0;
for cursor_y=-ceil(0.1*size_y):1:+fix(0.1*size_y),
    if binref(test_pix_x-ceil(0.1*size_x),test_pix_y+cursor_y)==1,
        index_cross_y1=index_cross_y1+1;
    end
    count_y1=count_y1+1;
end

index_cross_x2=0;
count_x2=0;
for cursor_x=-ceil(0.1*size_x):1:+fix(0.1*size_x),
    if binref(test_pix_x+cursor_x,test_pix_y+ceil(0.1*size_y))==1,
        index_cross_x2=index_cross_x2+1;
    end
    count_x2=count_x2+1;
end

index_cross_y2=0;
count_y2=0;
for cursor_y=-ceil(0.1*size_y):1:+fix(0.1*size_y),
    if binref(test_pix_x+ceil(0.1*size_x),test_pix_y+cursor_y)==1,
        index_cross_y2=index_cross_y2+1;
    end
    count_y2=count_y2+1;
end

all_pixels=count_x+count_x1+count_x2+count_y+count_y1+count_y2;
all_positive=index_cross_x+index_cross_x1+index_cross_x2+index_cross_y+inde
x_cross_y1+index_cross_y2;
ratio=all_positive/all_pixels;

%make the negative of the image if the ratio is 50%
if ratio>0.5,
    for ix=1:size_x(1),
        for iy=1:size_y(2),
            if binref(ix,iy)==0,
                binref(ix,iy)=1;
            else binref(ix,iy)=0;
            end
        end
    end
end
end

result=binref;

```

---

```

function ref_image= refcreator(nbttimepoints)

%directly converts the axon image into a reference line to analyse after in

```

---

```
%axomorph

dir=cd;
if nargin==0, nbtimesteps=1; end

for i=1:nbtimesteps;

%auto open the axon images
axoimage=importfile(['ax' num2str(i) '.tif']);

%sequence of operation to create the reference line
mean_intensity=mean(axoimage);
mean_intensity=mean(mean_intensity);
thres=mean_intensity*3;
bin_image=axoimage>thres;

a=bwmorph(bin_image, 'fill');
b=bwmorph(a, 'close');
c=bwmorph(b, 'erode');
d=bwmorph(c, 'thin',1);
e=bwmorph(d, 'dilate',10);

%result
ref_image=bwmorph(e, 'thin',100);

%save the ref file in the same folder
imwrite(ref_image,['ref' num2str(i) '.tif'],'tif');

end

figure (1)
imagesc(ref_image(i));figure(gcf);
```